TECHNISCHE UNIVERSITÄT DRESDEN
Technischen Universität Dresden
der Fakultät Mathematik und Naturwissenschaften

HZDR
Helmholtz-Zentrum Dresden-Rossendorf
Institut für Strahlenphysik\Strahlungsquelle ELBE

Optimization of an SRF Gun for High Bunch Charge Applications at ELBE

D I S S E R T A T I O N

zur Erlangung des akademischen Grades
Doctor rerum naturalium
(Dr. rer. nat.)

Von
Pengnan Lu
geboren am 30.05.1986 in Heilongjiang, China

Betreuer
Prof. Dr. Ulrich Schramm
Dr. Jochen Teichert

Eingereicht am 14.11.2016
Tag der Prüfung: 31.03.2017
Die Dissertation wurde in der Zeit von 07/2012 bis
10/2016 im Helmholtz-Zentrum Dresden-Rossendorf angefertigt.

Erster Gutachter:	Prof. Dr. Ulrich Schramm
Zweiter Gutachter:	Prof. Dr. Thomas Cowan
Dritter Gutachter:	Prof. Dr. Carsten Welsch

Abstract

As a cutting-edge technology for photoinjectors, SRF guns are expected to provide CW electron beams with high bunch charge and low emittance, which is critical to the development of future FELs, ERLs and 4th/5th generation light sources. However, existing research has not explored the full potential of SRF guns as predicted by theory.

Currently, the research activities at ELBE focus on solving technological challenges of a 3.5 cell SRF gun as well as applying it to high-bunch-charge experiments. This thesis aims to optimize the ELBE SRF gun and the relevant beam transport for future high-bunch-charge applications at pELBE, nELBE, TELBE and CBS experimental stations. Chapter 1 describes the demands of these applications on the SRF gun in detail. Chapter 2 outlines the development of a simulation tool based on ASTRA and Elegant, followed by the optimized gun parameters and the beam transport for the four experimental stations. Chapter 3 introduces beam diagnostic methods and data processing applied in this thesis. Chapter 4 presents results of experiments, including the pulse length measurement of the UV laser for generating electrons from the photcathode, the commissioning of ELBE SRF Gun II, a verification experiment on the LSC effect conducted at PITZ and a beam transport experiment with the bunch charge of 200 pC.

Simulation results have determined the effect of each SRF gun parameter on the beam quality and have provided optimized settings according to the requirements in Chapter 1. Experimentally, the LSC effect was confirmed at PITZ, in agreement with simulations which indicated that LSC significantly influences beam quality. The performance of ELBE SRF Gun II was improved and a beam with a bunch charge of 200 pC and an emittance of 7.7 μm from ELBE SRF Gun II has been transported through ELBE without visible beam loss.

The development of the simulation tool and beam diagnostics will serve further research at ELBE. Results of both simulations and experiments enrich the understanding of the existing SRF gun as well as the ELBE beamline and will guide continuing improvements. Already, ELBE SRF Gun II can deliver twice the bunch charge and lower emittance compared to the thermionic injector routinely used for ELBE. Ongoing modifications and development of the gun-cavity and photocathodes are expected to provide still further improvements. Progress on high-bunch-charge experiments at ELBE can be expected by applying the SRF gun.

Content

1. Introduction 1
1.1. ELBE SRF Gun 1
1.2. ELBE accelerator 8
1.3. High bunch charge applications 9
1.4. User-motivated optimization 15
2. Theory and simulation 16
2.1. Introduction 16
2.2. Parameterization of beam quality 17
2.3. Initialization from cathodes 21
2.4. ASTRA simulation for the gun 23
2.5. Elegant simulation of the beam transport 25
2.6. LabVIEW based simulation tool 39
2.7. Optimization of gun parameters 44
2.8. Optimization of beam transport 53
3. Beam diagnostic methods 73
3.1. The measurement of laser pulse length 73
3.2. Measurement of energy and energy spread 76
3.3. Slit scan emittance measurement 79
3.4. Quadrupole scan emittance measurement 89
4. Experimental results 94
4.1. Measurements of the laser pulse length 94
4.2. Commissioning of ELBE SRF Gun II with magnesium cathode 97
4.3. Longitudinal space charge experiments at PITZ 105
4.4. 200 pC beam transport in ELBE beamline 110
5. Conclusion 120
5.1. Summary of content 120
5.2. Outlook 122
Acknowledgement 124
Appendix 125
I. Table of abbreviations 125
II. Simulation parameters for Section 2.8 127
III. Simulation parameters for Section 4.4 129
Bibliography 131

1. Introduction

1.1. ELBE SRF Gun

1.1.1. History of SRF guns

Electron beams with high brightness, low emittance and high average current are demanded by cutting-edge and future accelerator projects, like Free Electron Lasers (FELs) [1], Energy Recovery Linacs (ERLs) [2] and 4th/5th generation light sources [3,4]. In most of these projects, photoinjectors are applied.

Direct Current (DC) guns, Normal Conducting Radio Frequency (NCRF) guns and Superconducting Radio Frequency (SRF) guns are the three most important categories of photoinjectors. DC guns provide electron bunches with the state-of-art performance [5, 6] in Continuous-Wave (CW) operation with high-average-current record [7]. But the DC voltage applied to short accelerator gaps is limited to several hundreds of keV, with which the quality of high-bunch-charge beams is limited by space charge effects. NCRF guns have performed the best in pulsed applications with high bunch charges [8] but their repetition rate is limited by ohmic wall losses in normal conducting cavities, therefore, they are usually operated in pulsed modes, or in CW modes but only with low frequency and low gradient [9]. In comparison, SRF guns are almost free of ohmic wall losses as their cavities are superconducting. Meanwhile, SRF guns can also be operated with much higher fields than DC guns [10]. To achieve CW beams with good quality and high bunch charge has always been motivating SRF gun projects. However, the development of SRF guns is still challenged by the processing of cavities, the performance of photocathodes and their lifetime, as well as the risk of cavity contamination.

The concept of the SRF gun was proposed in 1988 at the University of Wuppertal [11] and then different types of SRF guns have been developed in laboratories worldwide [12] with different approaches. Fig. 1.1 illustrates the distribution of SRF gun related studies with different features. Generally, SRF guns can be categorized by the ways how they combine photocathode with accelerating cavity.

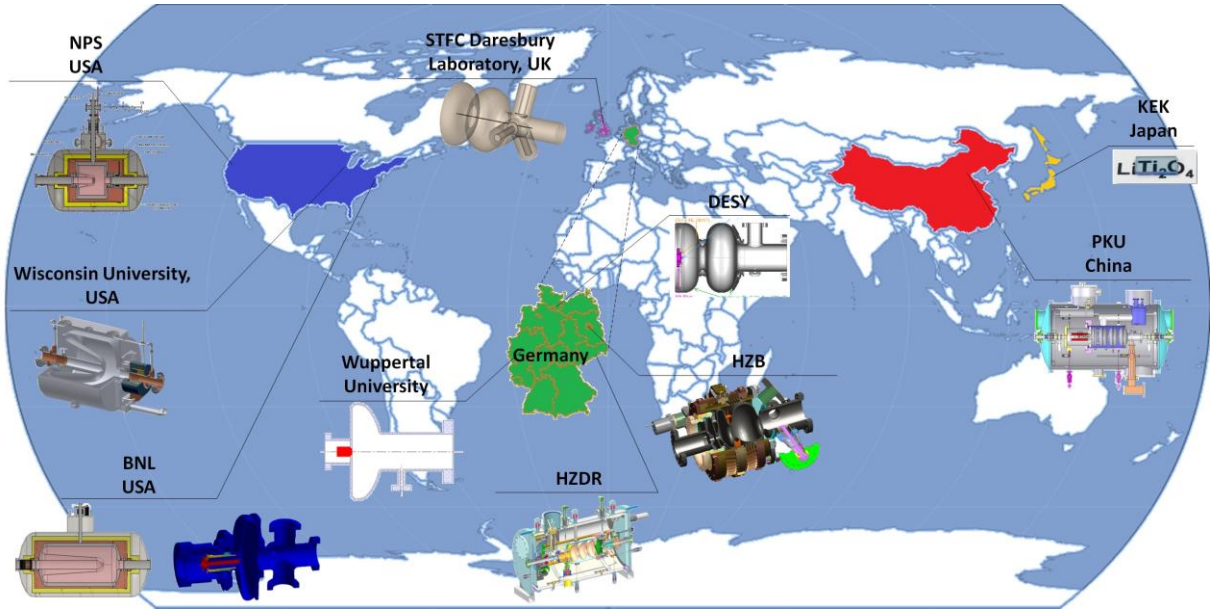

Fig. 1.1 Worldwide SRF gun projects and researches. Courtesy NPS, Wisconsin University, BNL, STFC, Wuppertal University, DESY, HZB, KEK and PKU.

As the first category, a DC-SRF gun was implemented in 2004 in Peking University (PKU) with a Pierce structure and a 1.5 cell superconducting cavity [13]. After that, a new photoinjector combining a DC Pierce gun and a 3.5 cell TESLA cavity has been developed as the injector of Peking University Free Electron Laser (PKU-FEL) facility and achieved stable mA-level average current in 2014 [14]. For this category of SRF gun, the DC gun in the front part reduces the risk of cavity contamination, however, the relative low gradient is not enough to conquer the space charge effect in high-bunch-charge operations.

The second category of SRF gun combines normal conducting cathodes directly with superconducting cavities. Six examples are included in this category and they are the majority of the SRF gun community.

At Helmholtz-Zentrum Dresden-Rossendorf (HZDR), a cathode working at 77 K is installed in a 1.3 GHz cavity with 3.5 TESLA-shaped cells working at 2 K. A choke filter is installed between the half cell and the cathode cooler to reduce RF leak. Development of this gun will be presented in detail in Section 1.1.2.

In the same way of combining cathode and cavity, a 1.4 cell 1.3 GHz TESLA cavity based SRF gun project is developing in Helmholtz-Zentrum Berlin (HZB) [15], which has been designed to provide a 100 mA beam with CsK_2Sb photocathodes for a 50 MeV ERL facility, named bERLinPro.

In Brookhaven National Laboratory (BNL) a 704 MHz half-cell SRF gun has been constructed for the R&D ERL project. It is designed to provide 0.5 A, 2 MeV electron beams. In 2014 the first beam was successfully generated [16].

The remaining three guns in this category use Quarter Wave Resonators (QWR) instead of elliptical cavities. All of them were manufactured by the company NIOWAVE. This structure has the advantage of lower frequency, which leads to a higher operation temperature up to 4.5 k. The first SC QWR prototype gun has been developed in Naval Postgraduate School (NPS) for NPS FEL. It works at 500 MHz and had the first beam in 2010 [17]. The second SC QWR photoinjector has been developed in Brookhaven National Laboratory (BNL) for electron cooling purpose with the worldwide lowest frequency of 112 MHz [18]. The third SRF gun of this type was developed in University of Wisconsin, working at 200 MHz, for a 2.2 GeV X-ray FEL [19].

The third category refers to the SRF gun in Deutsches Elektronen SYnchrotron (DESY), which is a 1.6 TESLA cell gun developed for the Free electron LASer in Hamburg (FLASH) as well as European X-ray Free Electron Laser (XFEL) [20]. This gun features the “all superconducting” design without a normal conducting cathode, while the back wall of the niobium cavity is coated with lead as the electron emitter. Such a design sacrifices high Quantum Efficiency (QE) but assures the cleanness of the cavity, which is ideal for CW applications with moderate bunch charge.

As the fourth category, a very recent TESLA cell based SRF gun project at KEK started in 2013 for the KEK 3 GeV ERL project, aiming to provide a 100 mA beam at 1.3 GHz for CW operation, with a bunch length of 3 ps and an emittance below 1 μm [21]. Besides these impressive parameters, an interesting design is the back illuminated cathode for shaping the laser profile easily with a shorter focal distance [22]. The structure of the cathode is shown in Fig. 1.2. $LiTi_2O_4$ is a new material featuring both transparency and superconductivity, which allows the laser to pass through and the RF to be reflected at the same time. The top layer of K_2CsSb has a very high QE which is over 30% at 405 nm, while at KEK the 355 nm Ultra Violet (UV) laser has been applied.

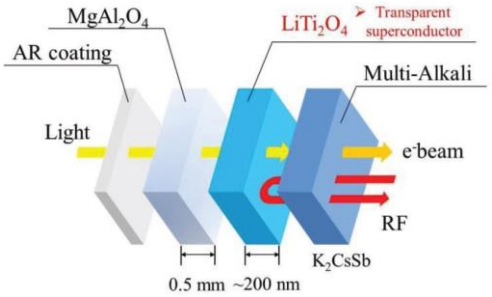

Fig. 1.2 The structure of the back illuminated photocathode of the SRF gun at KEK [22].

Besides the above four categories of SRF gun projects having been or being constructed, a conceptual design of SRF gun was made in STFC Daresbury Laboratory for Euro FEL Design Study, aiming to provide a strong current of 100 mA [23]. The specialty in this design is three separated 120°-mounted couplers with "pringle" shaped antennas minimizing the RF penetration into the beam pipe, shown in Fig. 1.1. This design is supposed to provide high level coupling ($Q = 10^5$) as well as highly asymmetric RF fields.

1.1.2. Development of SRF guns at HZDR

At HZDR, the research on SRF guns started in 1997. In 2002, for the first time worldwide, an electron beam was obtained from the SRF gun named DROSSEL [24]. A 1.3 GHz half-cell niobium cavity accelerated electron bunches from normal conducting photocathodes to 900 keV kinetic energy, and then the beam was injected to a dedicated diagnostics beamline. DROSSEL was the first proof that the combination of a normal conducting photocathode inside, while isolated from a superconducting cavity can work stably.

From 2004 to 2014, a 3.5 cell cavity based gun was developed and commissioned [25]. A UV laser system as well as a new diagnostics beamline was developed in collaboration with DESY, HZB and Max-Born-Institute (MBI). The cavity was designed in HZDR and produced by the company Research Instruments (RI). This gun was installed as one of the electron injectors of the "superconducting Electron Linac for beams with high Brilliance and low Emittance (ELBE)", hence, it was named "ELBE SRF Gun I". In 2013 it was utilized for the generation of an infrared FEL with a bunch charge of 20 pC and a current of 260 μA [26].

The ELBE SRF Gun I was designed to provide beams with the energy of 9.5 MeV, the maximum bunch charge of 1 nC and the emittance of 1 μm. But the cavity gradient could not reach the designed value due to scratches during high pressure rinsing and later its performance became even worse after several times of cathode changing. As the best performance of the cavity, this gun reached a CW gradient of 6.5 MV/m with kinetic beam

energy of 3.3 MeV and a pulsed RF gradient of 8 MV/m with kinetic beam energy of 4 MeV. The maximum current extracted from the Cs_2Te cathode has reached 400 μA.

In 2014, the upgraded ELBE SRF Gun II was installed and tested with a copper cathode [27]. The gradient was enhanced to 10 MV/m by a new constructed fine grain niobium cavity, in which field strength near the cathode is also higher than that of the old cavity for the same gradient, therefore the space charge effect has less influence. Besides the higher gradient, ELBE SRF Gun II contains a superconducting solenoid installed inside the cryostat for emittance compensation [28].

In 2015, a serious contamination happened in the process of cathode exchanging. The Cs_2Te cathode was polluted as well as the cavity itself. The gradient limitation was reduced to 7 MV/m and then gradually increased to 8 MV/m by RF power processing of the cavity. New cathode transfer chambers have been constructed to avoid the contact of the cathode and the vacuum tube. Meanwhile, magnesium cathodes are prepared as a safer replacement to produce some hundreds of pC electron bunches. The experiments presented in this thesis are all conducted with magnesium cathodes.

In the following of this thesis, the value of the (average) gradient of ELBE SRF guns is always about twice of the possible maximum kinetic energy value of the outcome electron bunches, as the length of the cavity is about 0.5 m.

1.1.3. Setup of ELBE SRF Gun II

This section introduces the current setup of ELBE SRF Gun II [29]. Fig. 1.3 is the cutaway view into the cryostat.

The core part of the SRF gun is a 3.5 cell fine grain niobium cavity, tested in Thomas Jefferson Laboratory [30]. The gradient at the entrance plane of the cavity is about 80 percent of the peak gradient. The 1.3 GHz RF is coupled from the main coupler with two RF windows applied to insulate the coupler. The resonance frequency can be achieved by tuning the cavity, realized by mechanically squeezing the niobium cells. The quality factor of the cavity is 5×10^9.

The cathode is located several millimeters outside of the cavity entrance plane, to generate a transverse focusing RF field to control the emittance growth [28]. As another applied method of emittance compensation, a superconducting solenoid is located 40 cm downstream of the cavity. The SRF cavity and the solenoid are cooled down by liquid helium to 2 K, while

the cathode nearby works at 77 K, cooled by liquid nitrogen. Twelve titanium strings fix the low temperature parts to the cryostat, as well as separating them from room temperature.

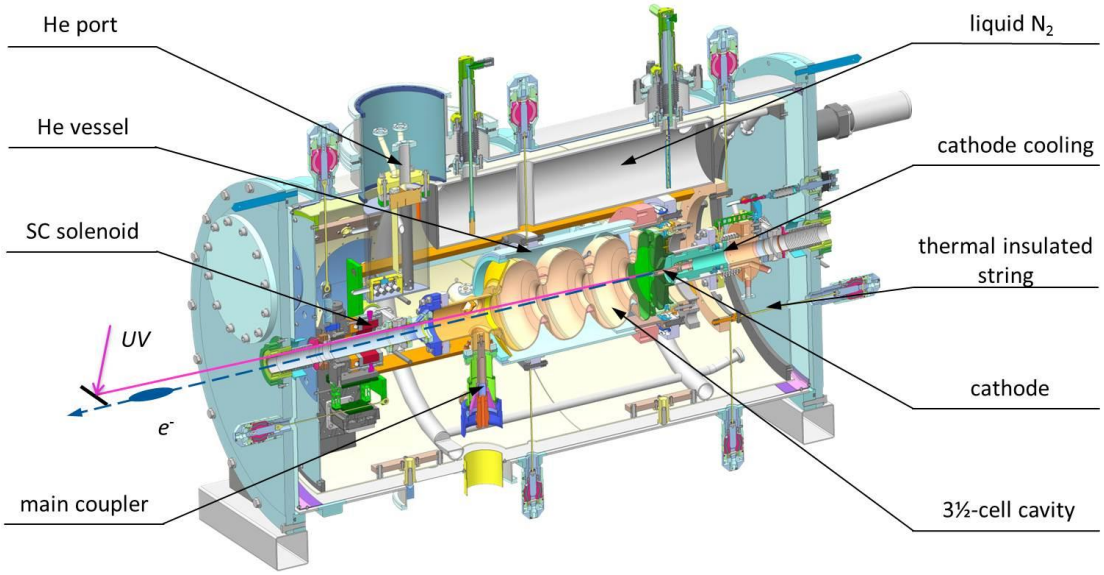

Fig. 1.3 The cutaway view of ELBE SRF Gun II.

A UV laser beam with a wavelength of 263 nm illuminates the photocathode to produce initial electron bunches [31]. The maximum power of the laser is 1 W, working at 13 MHz with the Full Width Half Maximum (FWHM) bunch length of 3 ps, or 100~500 kHz with the FWHM bunch length of 12~15 ps.

The development of photocathodes with high QE, long lifetime, low thermal emittance and prompt time response plays an important role in photoinjectors. Copper, magnesium and Cs_2Te cathodes are designed to be used for ELBE SRF Gun II. Copper cathodes provide a QE of 10^{-5} with the bunch charge of several pC, used only for the demonstration of the cavity and the first commissioning. Magnesium cathodes have a higher QE of 10^{-3} after laser/ion-beam cleaning [32~34] and provide bunch charges of some hundreds of pC. Cs_2Te cathodes have the highest QE in the order of 10^{-2}, but the preparation process is more complicated and the requirement to the vacuum is also higher.

At HZDR, Cs_2Te cathodes are prepared in a chamber with the vacuum of 10^{-9} mbar in a clean room. As shown in Fig. 1.4, up to 6 cathodes can be loaded inside the transport chamber. The working cathode can be exchanged using the manipulator. The highest QE up to now is 1×10^{-2} and the longest lifetime is over 1 year, with 234 C of electrons extracted.

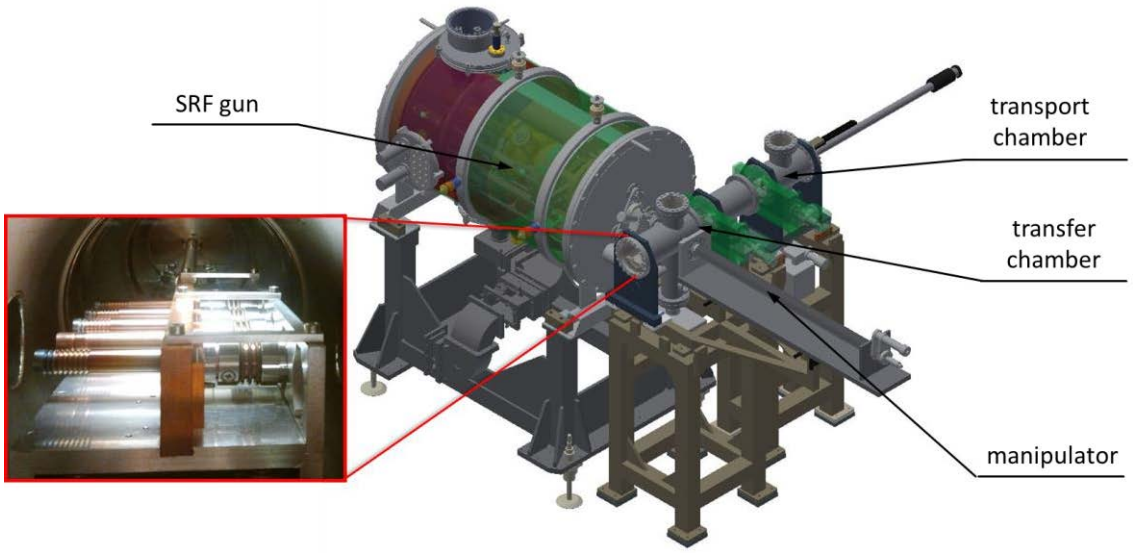

Fig. 1.4 Cathodes transport and transfer system of ELBE SRF Gun II.

The magnesium cathodes are cleaned by the same UV laser as used for bunch generation, but focused to produce a higher photon density. The cleaning is operated in the transport chamber when it is connected to the SRF gun. The QE of the magnesium cathode reached 1×10^{-3}, while the best QE in literature is 2×10^{-3} [33].

1.2. ELBE accelerator

The ELBE accelerator is a high-power radiation sources open for users all over the world. The main radiation is an SRF Linac based, CW operating electron beam with the maximum energy of 40 MeV and the maximum current of 1.6 mA [35]. Fig. 1.5 illustrates the layout of ELBE.

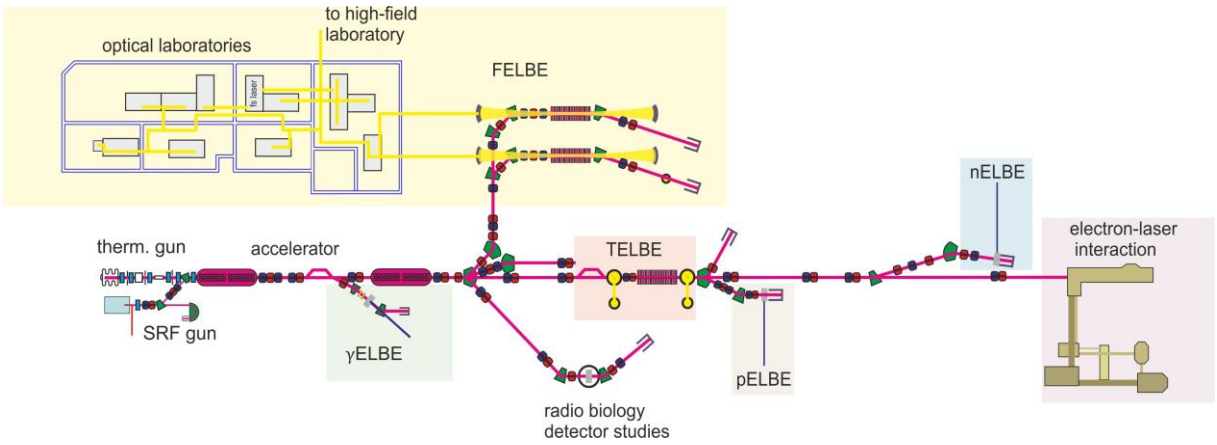

Fig. 1.5 The layout of ELBE.

The injector routinely used in ELBE is a DC gun with a grid-pulsed thermionic cathode [36]. It provides a pulsed electron beam with an energy of 250 keV, a maximum bunch charge of 77 pC, a normalized transverse emittance of 13 μm and a bunch length of 500 ps. Electron bunches are first compressed in the subsequent drift path by the energy modulation produced in a subharmonic buncher running at 260 MHz, then further compressed in the following 1.3 GHz fundamental buncher before entering the first superconducting cavity.

The electron beam from the DC thermionic gun is accelerated by two SRF Linacs. Each Linac contains two 9-cell Nb TESLA cavities working with 1.3 GHz standing wave. The operation temperature is 2 K, cooled by superfluid helium. The designed energy gain of each cavity is 10 MeV and the quality factor is 10^{10}. Two chicanes are installed for bunch compression. One of them is located between the two Linacs and the other is after the second Linac. Each chicane consists of 4 dipoles, arranged in a D-shape.

The direct use of the electron beam includes radiobiology research and the interaction with ultra-intense lasers for Thomson scattering experiments. In addition, the electron bunches are also used to generate secondary user beams of two FELs operating in the IR/THz regime; a fast neutron beam; a Bremsstrahlung gamma-ray beam; a low-energy positron beam, patented single-electron test beams and THz radiation [35].

1.3. High bunch charge applications

1.3.1. Positrons (pELBE)

At ELBE a monoenergetic positron beam is created by pair production from the primary electron beam at a multi-layer tungsten target. The positron experiment station is referred to as pELBE. The energy of the positron beam is adjustable in the range from 0.5 to 15 keV. The positron flux is 10^6 /s and the time structure inherits that from the electron beam.

One of the applications of the positron beam is to measure the size of defects in certain materials [37]. Nowadays Complementary Metal-Oxide-Semiconductor (CMOS) with low dielectric constant shows the potential of increasing the computer performance by faster response and lower heat consumption. One way of reducing the dielectric constant is to generate defects in the material.

Positrons can be trapped in these defects in the form of positronium, which is a combination of a positron and an electron behaving like a hydrogen atom. A positronium with the total spin of 1 is called ortho-positronium (o-Ps), while one with the total spin of 0 is called para-positronium (p-Ps). The average lifetime of an o-Ps is over 1000 times of that of a p-Ps. The size of the defects determines how frequently positroniums collide with material wall, that is, how frequently a long-lifetime o-Ps has a chance to be transferred to a short-lifetime p-Ps and annihilates immediately. Therefore, by measuring the emitted photon beam intensity with respect to time, the lifetime of positroniums can be measured and correspondingly the dimension of the defects can be calculated.

For the measurement of average positron lifetime, a lower frequency of the electron beam enables a wider measurement range, while higher bunch charge leads to higher positron intensity, which increases the measurement accuracy. Therefore, pELBE requires the bunch charge of the electron beam to be as high as possible, which is one of the motivations of developing the SRF gun for ELBE.

At 140 mm before the target, there is a 0.2 mm thick, 8 mm diameter beryllium window, isolating the vacuum of the beamline. The beryllium window scatters the beam, and by the theory of multiple scattering through small angles [38] the rms scattered angle can be estimated by:

$$\theta_0 = \frac{13.6\ \mathrm{MeV}}{vp} Z \sqrt{\frac{s}{S_0}} \left[1 + 0.038 \ln\left(\frac{s}{S_0}\right)\right] \tag{1-1}$$

where v, p and Z denote the velocity, momentum and the charge number of the incident particle respectively, while s/S_0 is the thickness of the scattering medium over the radiation length. For beryllium, the radiation length S_0 is 35.3 cm, and θ_0 is calculated to be 30 mrad for a typical 30 MeV beam.

The designated transverse beam diameter on the tungsten target is 5 mm, while the overall target is a 10 mm × 10 mm square. In order to transport most of the scattered beam into the target, the phase space of the electron beam on the beryllium window is preferred to be inside the region of:

$$|r_{be} + l(r'_{be} \pm \theta_0)| \leq R_{tar} \tag{1-2}$$

where r_{be} and r'_{be} are the transverse position and divergence of the electron beam respectively, l is the distance from the beryllium window to the target and R_{tar} is the maximum possible radius on the target. The solution of Equation (1-2) is shown in Fig. 1.6 where the area between two lines in the phase space accepts the beam with an angle smaller than θ_0. If this condition cannot be satisfied, a suboptimal condition should be applied, which is described in Section 1.3.2 for neutron beamlines.

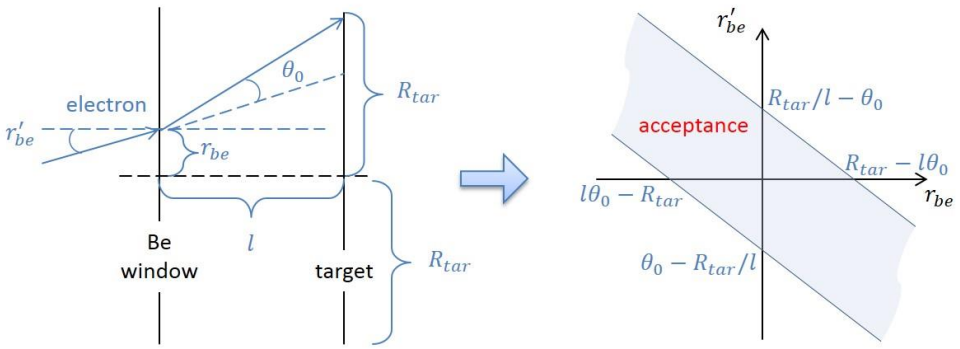

Fig. 1.6 Geometries of the scattered electron beam on the beryllium window and the target (left). The area of acceptance on the beryllium window (right).

The requirements on the electron beam for the positron generation are summarized in Table 1.1. The requirements on the energy spread and the bunch length are satisfied in most cases. The total energy depends on the performance of SRF cavities. A high bunch charge and the transverse phase space at the window are the main challenges of beam transport.

Table 1.1 Requirements of pELBE & nELBE on the electron beam.

parameter	pELBE & nELBE requirement
bunch charge	as high as possible
energy	as high as possible
energy spread	≤ 5%
bunch length	≤ 20 ps overall
transverse bunch size	≤ 8 mm overall
transverse divergence	required by the Be window
transverse emittance	—
dark current	as low as possible

1.3.2. Neutrons (nELBE)

A very compact neutron Time-of-Flight (ToF) system has been built at ELBE, named nELBE [39]. Electron beams are injected into a liquid-lead neutron radiator to produce neutrons with a continuous range of energies, together with the bremsstrahlung by the interaction of electrons and lead nucleus. With an electron beam of which the repetition rate is 0.2 MHz, the measurable energy range for neutrons is from 100 keV up to 10 MeV. In this energy range, the measurement of the cross section for neutrons is demanded by basic scientific researches and technical applications. Also, the long term needs of the nuclear data have been formulated [40].

The neutrons are emitted almost isotropically from the radiator, while most of the electrons and the bremsstrahlung photons mainly travel in the forward direction. To obtain a higher neutron-to-photon rate, the 90° scattered neutrons are selected by a collimator to perform ToF measurements. A BaF_2 scintillation detector array is built to capture neutrons. Li-glass scintillators and a plastic scintillator wall have been developed to detect neutrons[41].

The neutron intensity at the measurement position is determined by the radiator dimensions, the length of the neutron flight path and the power of the electron beam. Besides, with the same energy and the same average current, a higher bunch charge increases the Signal to Noise Ratio (SNR). In addition, a lower repetition rate increases the measurable flight time of neutrons, corresponding to a wider measureable energy range. To achieve higher bunch charges and lower repetition rates, the SRF gun is designed to have a 100 ~ 500 kHz laser

mode with the maximum current of 1.6 mA, which is limited not by the gun itself but by the Helium system for the whole accelerator.

A beryllium window is also used for nELBE to separate the vacuum before the liquid-lead target, located 190 mm before the target. The thickness of the window is 0.2 mm and the diameter is 8 mm. The requirement of the transverse phase space should be the same to that for pELBE, however, for an energy lower than 34.2 MeV, the geometric setting of the window in nELBE satisfies $R_{tar} \leq l\theta_0$, implying that the acceptance area in Fig. 1.6 will vanish. In this case, to obtain the highest electron current on the target, the phase space of the incident beam should be manipulated to meet:

$$\varphi_b = \frac{1}{2}\tan^{-1}\left(\frac{-2\alpha}{\beta-\gamma}\right) = -\frac{1}{l} \tag{1-3}$$

where α, β, γ are the Twiss parameters of the electron beam, and $\varphi_b = 1/2 \cdot \tan^{-1}[-\alpha/(\beta-\gamma)]$ defines the orientation of the phase ellipse [42], illustrated in Fig. 1.7. The requirements of the electron beam at nELBE are the same as for pELBE, listed in Table 1.1.

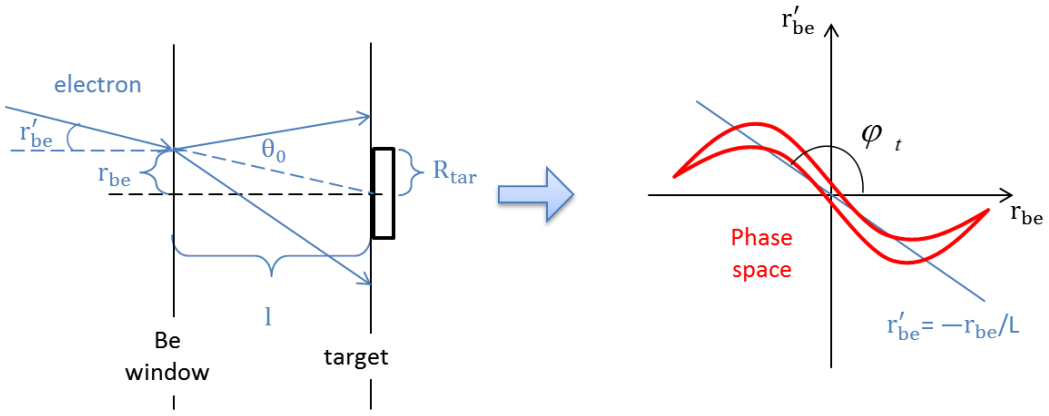

Fig. 1.7 Indication of the case in which the scattered beam is larger than the target, even when the incident beam has zero radius and zero divergence (left). In this case, the incident beamlet at any position of the beryllium window should point to the center of the window, therefore the orientation of the phase space should be $-1/l$.

1.3.3. THz radiation (TELBE)

The high-field high-repetition-rate THz user facility TELBE has been built up and commissioned recently [43]. An undulator and a silicon mirror with a 4 mm diameter aperture are installed as two radiators at TELBE. The undulator generates 8 cycle radiations with the frequency tunable from 100 GHz to 3 THz. The silicon mirror generates single cycle of the Coherent Transition Radiation (CTR) or the Coherent Diffraction Radiation (CDR).

Radiations generated by both the undulator and the silicon mirror are intrinsically synchronized to each other, as they originate from the same electron beam of ELBE.

THz radiations from short relativistic electron bunches carry information of the arrival time, the charge and the pulse's longitudinal profile. TELBE aims to develop the THz based Beam Arrival-time Monitor (BAM) and the Bunch Compression Monitor (BCM) for fs-diagnostics of quasi-CW electron beams. Meanwhile, with the worldwide unique repetition rates up to the MHz regime, the high-field THz pulses can also be used for THz driven dynamics, such as duty-cycle hungry spectroscopic techniques [44] and time-resolved near-field microscopy [45].

The typical compressed electron bunch at ELBE has the bunch length of 1 ps, much shorter than the period of the THz radiation. In this case, the coherent radiation dominates the radiation intensity, which is proportional to the square of the longitudinal charge density. Therefore, the bunch charge of the electron beam is crucial for the THz generation, so is the bunch length.

Other requirements are listed in Table 1.2. The requirement of the 4 mm diameter comes from the aperture of the silicon mirror, and the high energy influences the cutoff of the measured signal.

Table 1.2 Requirements of TELBE on the electron beam.

parameter	THz requirement
bunch charge	as high as possible
energy	as high as possible
energy spread	—
bunch length	FWHM as short as possible
transverse beam size	≤ 4 mm diameter
transverse divergence	—
transverse emittance	—
dark current	—

1.3.4. Compton backscattering (CBS)

Compton backscattering (CBS) is one of the most effective methods of gaining energy for photons [46], producing intense pulses tunable from hard X-rays to γ rays with finite bandwidth [47,48]. The mechanism of Compton scattering is also referred to as Thomson scattering when the recoil of electrons is negligible [49], which is the case at ELBE.

The longest beamline of ELBE delivers the electron beam to perform the CBS experiments with a 150 TW laser which is the DResden lAser aCceleration sOurce (DRACO) [50,51]. The electric field of the laser pulse acts on electron bunches like a traditional undulator, but with a much smaller spatial period, which is the laser wavelength. Compared to those facilities operating at GeV regime with kilometers long traditional undulators such as LCLS, SACLA and XFEL, Thomson scattering requires a much lower energy from the electron beam, for emitting photons with the same energy [49]. The development of such a compact laser-electron-interaction based source for ultra-short ($\leq$ 1 ps), hard (1 keV) X-ray pulses is motivated by the single exposure experiments in the scientific fields like ultrafast phase transitions [52], structural dynamics [53] and (bio)chemical reactions [54].

The DRACO laser spot can be expanded to a maximum FWHM diameter of 35 μm, which is a quite small dimension for electron beams with bunch charges over 100 pC. The number of electrons that can be focused into this region dominates the intensity of the generated X-ray. A Final Focusing System (FFS), which consists of four strong permanent magnet quadrupoles, has been developed to focus the electron bunch just before the interaction point. In this application, the challenge for the SRF gun is not only the higher bunch charge required, but also a small emittance for the crucial transport requirements.

The measurement range of the current photon detector requires the energy of the electron bunch to be less than 25 MeV. The bunch length is preferred to be less than 1 ps. The energy spread and transverse emittance are important before the FFS, which will influence the minimum size of the focused beam. All requirements are listed in Table 1.3.

Table 1.3 Requirements of CBS experiments on the electron beam

parameter	CBS requirement
bunch charge	as high as possible
energy	$\leq$ 25 MeV
energy spread	as small as possible before the FFS
bunch length	$\leq$ 1 ps
transverse beam size	FWHM 35 μm the best
transverse divergence	—
transverse emittance	as small as possible before the FFS
dark current	as low as possible

1.4. User-motivated optimization

This PhD work is based on the current setup of ELBE SRF Gun II, aiming to optimize the beam quality according to the requirements of the high-bunch-charge applications. Both the operation of the gun and the beam transport are relevant to this purpose.

From the aspect of the SRF gun itself, the first challenge comes from the gradient which is currently lower than the designed value. When an electron bunch with several hundreds of pC is initially generated from the cathode with its energy less than 1 eV, it is strongly space charge dominated and will expand in the 3D space meanwhile the emittance will also increase. The space charge effect declines with energy, thus, a lower gradient reduces the highest possible bunch charge. It is of importance for developing the SRF gun project to improve the beam quality in addition to increasing the gradient.

The second challenge of the SRF gun is the dark current. For high bunch charge operation at 100 kHz for example, the duty factor of a typical 10 ps bunch is 1×10^{-6}, while the field emission of the CW 1.3 GHz RF cavity produces a dark current in about 60% of the time. Therefore, for nELBE, pELBE and CBS experiments where detectors perform accumulation of measured signals, the dark current contributes to the main part of the noise.

From the aspect of the beam transport, space-charge-relevant effects like coherent synchrotron radiation, wake potential and longitudinal space charge should be carefully considered in ELBE beamline, as the beamline is not designed for the SRF gun with a high-bunch-charge beam in the first place. Studies in this thesis indicate that these effects influence the beam quality substantially.

To optimize the gun parameter and the beam transport according to the requirement of experimental stations, a proper optimization procedure is necessary. Instead of scanning all parameters of the beamline which is almost impossible in both experiments and simulations, independent optimization tasks are separated and conducted in simulations, which are also used to guide the experiments in this thesis.

The simulation based optimization is presented in Chapter 2. Necessary beam diagnostics are improved or developed as presented in Chapter 3. Experimental results are shown and analyzed in Chapter 4. The purpose of the entire work is not to achieve certain parameter records of an SRF gun, but to make the gun serve better in the ELBE center.

2. Theory and simulation

2.1. Introduction

Parallel to the hardware development of ELBE SRF guns including cavity test, cathode preparation, installation and commissioning, a simulation tool has been built up to study the dynamics of the gun and the accelerator. It is flexible to process most settings of the SRF gun and has been used to optimize the transport of high-bunch-charge beams to user stations.

In this simulation tool, the emission of the electron bunch and its acceleration in the gun cavty are simulated with ASTRA [55], using RF field distributions calculated with Superfish [56]. The following beam transport is simulated with Elegant [57], with the Green's function of Screen-stations calculated in CST [58] to estimate wake potentials. To execute ASTRA and Elegant sequentially, a LabVIEW interface is programmed, which can also be used to process the simulation results.

This chapter is organized as follows: frequently used parameters in the following chapters are described or defined first in Section 2.2. In the next, important physical effects included in the simulation are generally investigated and exemplified in Section 2.3 - 2.5. Then the simulation tool is introduced in Section 2.6. After that, the dependence of beam quality on gun parameters are presented, as well as choices of optimized gun-parameter combinations for different purposes of beam transport in Section 2.7. With these combinations, optimization methods for beam transport are proposed based on the setting of ELBE, followed by optimization results for pELBE, nELBE, TELBE and CBS presented and analyzed in Section 2.8.

As mentioned, the ELBE beamline was not designed in the first place for the SRF gun. For the first time, this simulation study has analyzed challenges of experiments at ELBE using the SRF gun and has provided guidance on how to improve the beam quality.

2.2. Parameterization of beam quality

This section introduces parameters used in this thesis to represent the beam quality. Some of the parameters are commonly used in accelerator science, while others are newly defined to simplify the following analysis.

The coordinates of all particles in the 6D phase space of (x, x′, y, y′, t, E) contains the complete information about a bunch, where x is the horizontal coordinate, x′ is the horizontal angle, y is the vertical coordinate, y′ is the vertical angle, t is the temporal coordinate and E is the energy. The origin for x, x′, y, y′ or t is the numerical average of all particles. Statistical averages of parameters are used to describe the bunch instead of coordinates for all particles.

Using u to represent x or y, the statistical average parameters for a bunch of n electrons used in this thesis include:

- $\overline{E}$: The average energy of all electrons.
- σ_u: The rms horizontal/vertical bunch radius, $\sigma_u = \sqrt{1/n \cdot \sum u^2}$.
- Δu: The FWHM value of the horizontal/vertical bunch radius.
- $\sigma_{u\prime}$: The rms horizontal/vertical bunch divergence, $\sigma_{u\prime} = \sqrt{1/n \cdot \sum u'^2}$.
- ε_u: normalized rms horizontal/vertical emittance.

  $\varepsilon_u = \beta\gamma\sqrt{\sigma_u{}^2 \cdot \sigma_{u\prime}{}^2 - (1/n \cdot \sum u \cdot u')^2}$, where β and γ are relativistic parameters of the bunch center.
- σ_t: The rms bunch length, $\sigma_t = \sqrt{1/n \cdot \sum t^2}$.
- Δt: The FWHM bunch length.
- σ_E: The rms energy spread, $\sigma_E = \sqrt{1/n \cdot \sum (dE)^2}$, where $dE = E - \overline{E}$.
- α_u: rms Twiss parameter, $\alpha_u = -\sqrt{(1/n \cdot \sum u \cdot u')}/\ \varepsilon_u$.
- β_u: rms Twiss parameter, $\beta_u = \sigma_u{}^2/\varepsilon_u$.
- γ_u: rms Twiss parameter, $\gamma_u = \sigma_{u\prime}{}^2/\varepsilon_u$.

From the definitions above, Twiss parameters satisfy the following equation:

$$\beta_u\gamma_u - \alpha_u{}^2 = 1 \tag{2-1}$$

The relation between Twiss parameters and the phase ellipse in Transverse Phase Space (TPS) is shown in Fig. 2.1. φ_t is the orientation angle of the phase ellipse, which will be introduced in the following paragraphs.

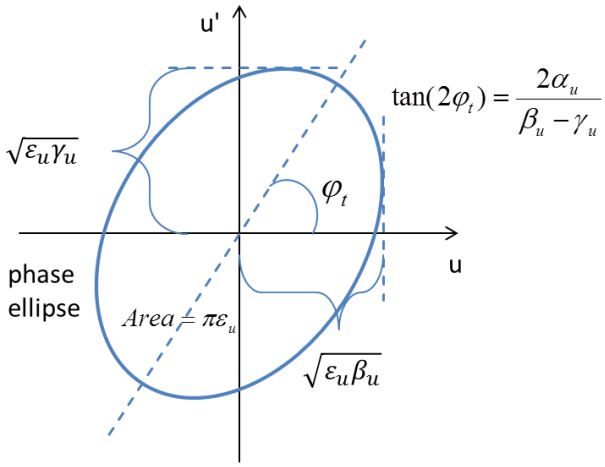

Fig. 2.1 Twiss parameters in phase space.

Electron bunches from the SRF gun are accelerated by the RF field of a 3.5 cell standing-wave cavity. Electrons at different longitudinal positions experience different fields. It leads to different distributions of slices along the bunch in TPS, as a result of which the transverse emittance can be enlarged. This phenomenon is referred to as "slice mismatch." To study the slice mismatch quantitatively, following parameters are defined:

- φ_u: The "mismatch phase" of an individual slice in the horizontal/vertical phase space, $\varphi_u = \varphi_{us} - \varphi_{ut}$, where φ_{us} and φ_{ut} are the orientation angles of an individual slice and the total bunch respectively.
- $O_{\varphi u}$: The overlap ratio of the mismatch phase. This parameter is defined to represent the degree of orientation-overlap among all slices throughout the bunch. $O_{\varphi u} = (\varphi_{u,max}\text{-}\varphi_{u,min})/\sum_{i=1}^{n_s-1}\left|\varphi_{u,i}\text{-}\varphi_{u,i-1}\right|$, where $\varphi_{u,max}$ and $\varphi_{u,min}$ are the maximum and minimum mismatch phases for all slices, n_s is the number of slices and i is the slice index. The intuition of this parameter will be explained in Section 2.5.1.
- φ_{unor}: Normalized mismatch phase, $\varphi_{unor}=\varphi_u\cdot\sigma_{\varphi u}^{-1}\cdot O_{\varphi u}$, where σ_φ is the standard deviation of mismatch phases for all slices.
- k_u: Horizontal/vertical kick of an individual slice, which is the horizontal/vertical distance between the slice center and the bunch center. Through dipoles, slices with different energy have separated positions at the exit.

- O_{ku}: The overlap ratio of the horizontal kick of slices, representing the degree of transverse-position-overlap among all slices throughout the bunch. $O_{kx} = (k_{umax} - k_{umin}) / \sum_{i=1}^{n_s-1} |k_{u,i} - k_{u,i-1}|$, where k_{umax} and k_{umin} are the maximum and minimum horizontal kick for all slices.
- k_{unor}: normalized kick by rms beam size, $k_{unor}=k_u \cdot \sigma_u^{-1}$
- $\varepsilon_{ave.s.u}$: The weighting average of the horizontal/vertical slice emittance in the bunch. The weight is the number of particles in each slice.

For the purpose of bunch compression, it is of interest to study the bunch distribution in Longitudinal Phase Space (LPS). In addition to bunch length and energy spread, the following two longitudinal parameters are defined:

- k_l: The slope of the linear fitting in the LPS of the entire bunch.
- DoN: This parameter is to quantify the nonlinearity of the distribution in LPS. $DoN = 1/n \cdot \sum |E - E_f|$, where E_f Is the linearly fitted energy of an individual particle.

The above slice-based parameters are shown in the phase space in Fig. 2.2.

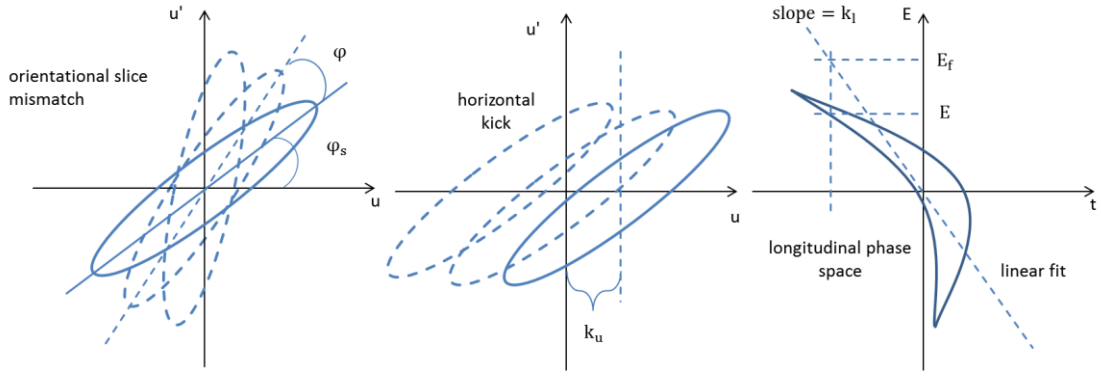

Fig. 2.2 The slice-based parameters.

Simulations to be presented in the following are conducted with 10^5 particles. For output bunches of ASTRA, electrons are recorded at the same time at different longitudinal positions. To compare simulated emittance with usual measurements at a fixed position, the "projected emittance" is applied such that all particles are drifted to their longitudinal center along the tangent of individual movement before the emittance calculation. However, for output bunches of Elegant, the emittance is calculated directly since electrons are recorded at the same longitudinal position. Moreover, "emittance" here always refers to the transverse normalized rms emittance, either by default for the entire bunch or as indicated for slices. All

numbers concerning the bunch size, the bunch length and the energy spread are rms values, unless indicated otherwise.

2.3. Initialization from cathodes

The cavity of ELBE SRF Gun II was tested with a Cu cathode, which generates less than 1 pC electron bunches. The Cu cathode was also used for studying dynamics of the SRF gun without space charge effects. For high-bunch-charge operations, Mg cathodes and Cs_2Te cathodes were prepared and applied. In simulations the initialization of the bunch emitted from these three kinds of cathodes is included.

For all cathodes, the spatial distribution of electrons is assumed to be a classic distribution by ASTRA, e.g., Gaussian or uniform distribution, in 3 dimensions. The momentum distribution, however, is different between metal and semiconductor.

In Cs_2Te, electrons are first excited by photons from the valence band to the conduction band, and then migrate to the solid surface. If the energy of the electron is higher than the threshold of the surface potential barrier, it is possible for the electron to cross the surface [59]. If the UV laser with the photon energy of 4.72 eV (wave length of 263 nm) hits the surface of Cs_2Te, some electrons will be excited to an energy state lower than the photon energy value (tunneling is neglected). As shown in Fig. 2.3, the state density below 4.72 eV is the highest around the energy band of 4.05 eV, therefore most electrons will be excited to this energy band. After conquering the surface potential barrier of 3.5 eV, the majority of emitted electrons will have the kinetic energy of $E_{kin} = 0.55$ eV.

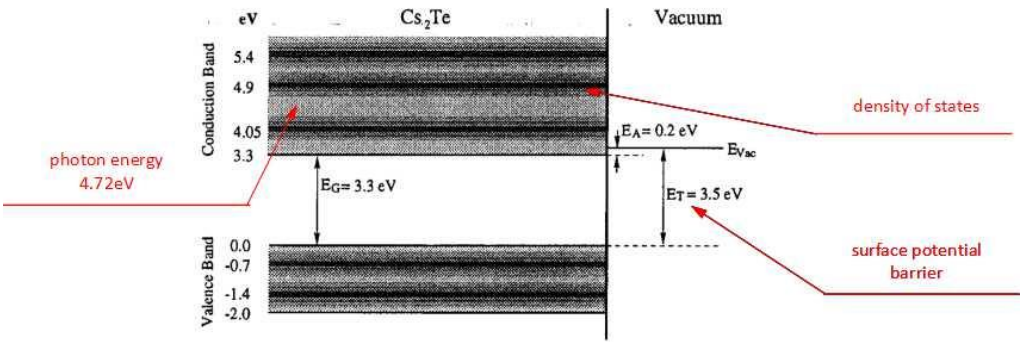

Fig. 2.3 Schematic band structure of Cs_2Te. Dark lines indicate the density of energy states [59].

The momentum directions of the emitted electrons are assumed isotropic in a half-sphere facing outward the cathode surface, resulting in the following thermal emittance of Cs_2Te cathodes:

$$\varepsilon_u(Cs_2Te) = \sigma_u \cdot \sqrt{\frac{2E_{kin}}{3E_0}} \tag{2-2}$$

where σ_u is the rms bunch size and E_0 is the rest energy.

The electron emission from metals (in this thesis for Cu and Mg) is calculated in Reference [60]. The distribution of electrons in the cathode obeys Fermi Dirac function. Photons excite electrons to an energy of higher than the Fermi energy, and the electrons escape the surface into vacuum. The spill-out electrons experience electric fields from the mirror charge, as well as the applied field from the cavity. The total field is called "Schottky potential" which influences the work function of the metal. Accordingly, the effective work function with the Schottky effect considered is:

$$\phi_{eff} = \phi_w - \sqrt{\frac{eF_a}{4\pi\varepsilon_0}} \tag{2-3}$$

where ϕ_w is the work function of the metal and F_a is the applied field on the cathode. Fig. 2.4 illustrates the emission procedure and the effective work function.

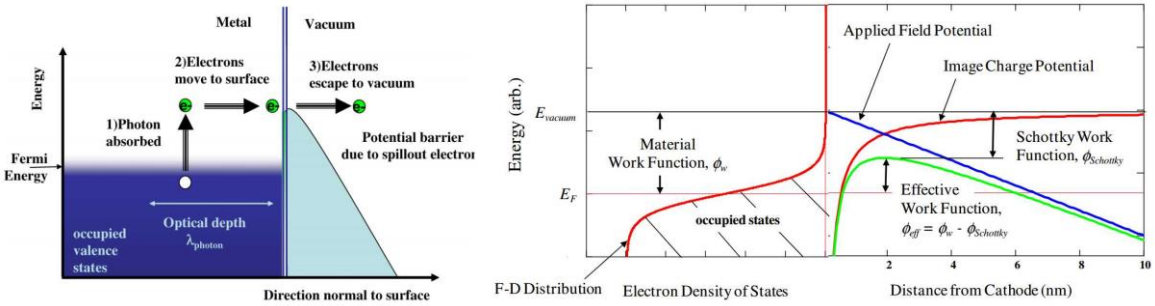

Fig. 2.4 Photoelectric effect based electron emission from metal surface [60].

Calculations in Reference [60] solved the distribution of the 3D momentum which is applied here to initialize the bunch. The thermal emittance of the bunch is:

$$\varepsilon_u(\text{Metal}) = \sigma_u \cdot \sqrt{\frac{E_p - \phi_{eff}}{3E_0}} \tag{2-4}$$

where E_p is the energy of the incident photons.

2.4. ASTRA simulation for the gun

2.4.1. Physics and approximations

After the bunch generation, the coordinates of particles are tracked with the RF field of the gun-cavity and the DC field applied on the cathode to suppress the multipacting emission of secondary electrons. 1D DC and RF fields are calculated in Superfish and then called by ASTRA. Field data with typical parameters (DC voltage = 5 keV, gradient = 7.5 MV/m, see Section 2.7) for different cathode positions are shown in Fig. 2.5, which are further expanded to generate the 3D field distributions [55].

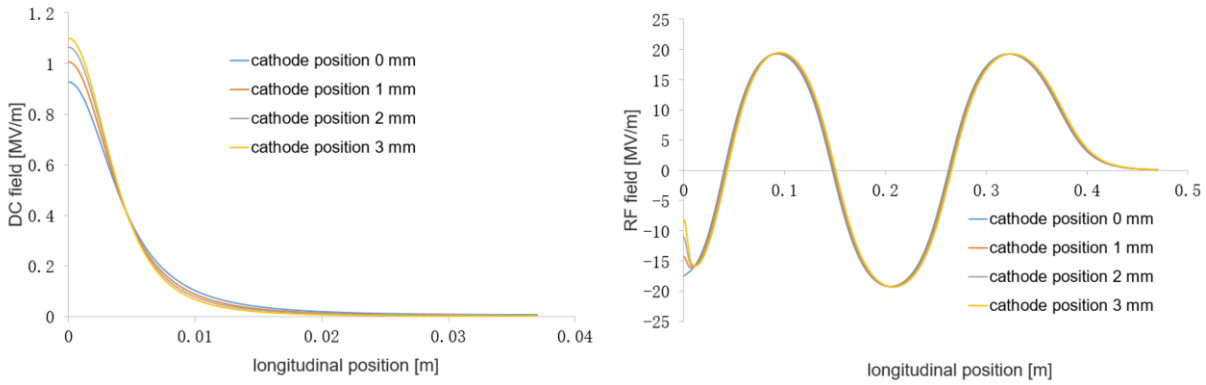

Fig. 2.5 DC and RF fields calculated in Superfish with different distances between the cathode and the back plane of the cavity. The DC field is about one magnitude lower than the RFfield and decays in a few millimeters.

Except for applied fields, the extracted bunches also experience self-induced electric field from the surface of the cathode. ASTRA calculates the mirror charge, assuming that the cathode surface is an infinite plane. However, in reality the geometric borders of the cathode and the back plane of the cavity are more complicated. The cathode is retreated several millimeters to perform an RF focusing of the generated bunch [61], resulting in new mirror charges from the cavity tube, through which the cathode is inserted towards the cavity. The complex geometries for mirror charges are simplified in ASTRA, but the RF focusing is included. High order terms of the expanded 3D fields are important to obtain sufficient accuracy in calculations of the RF focusing.

The space charge effect is calculated in ASTRA in three steps. Firstly, space charge fields are calculated in grid cells based on the initial distribution of electrons. Secondly, the kicks to the coordinates of electrons in 6D phase space are calculated in a time step. Thirdly, the space charge field is scaled by the new 3D distribution of the bunch. If the scale parameter is larger than what the user has defined as the threshold, a new space charge field will be calculated.

The accuracy of the space charge calculation depends on the proper choice of the grid which has to be specified by the user. On one hand, if the number of grids is too small, the field is not smooth enough. On the other hand, too many grids result in artificial structures of the field [62]. The number of grids covering the bunch is set to be 35 longitudinally and 25 radially as the optimum.

Another effect influencing the particle tracking is the wake potential of all geometrical irregularities, including the cavity, the cathode and the beam tube. The wake potential of ELBE SRF gun has been studied locally with CST [63] but it is not included in ASTRA simulations. Although ASTRA has the built-in element “Wake” to perform a local wake kick with an input pseudo Green’s function, the convolution of the Green’s function assumes a constant bunch size, which changes significantly in practice in the gun cavity.

To summarize, in ASTRA simulations of ELBE SRF gun, the electron emission, the acceleration, the RF focusing and the self-space-charge forces are well considered. The mirror charge effect is approximated using a model of infinite-plane cathode. The wake potential is temporarily neglected.

2.5. Elegant simulation of the beam transport

2.5.1. Slice mismatch

One of the features of SRF guns that is different from DC guns is the acceleration in the standing-wave RF cavity. Longitudinal slices experience different RF fields, and as a result, they have different energies. Meanwhile, in TPS the slices can also be separated, resulting in a large emittance. In the following, "slice mismatch" will be used to describe the non-perfect overlap among slices in TPS.

The beam transport in the ELBE accelerator is calculated to the third order in Elegant. Transverse emittance variation has been observed in the 2nd and 3rd order. The following analysis shows that the variation is induced by chromatic effects which change the slice mismatch state: when propagating through a magnetic field, slices with different energies evolve differently in transverse phase space. The emittance of the entire bunch is minimized when every slice lies within the same area of the transverse phase space.

Fig. 2.6 illustrates an example of the emittance variation with a bunch passing through only one quadrupole. The incident bunch has an energy of 24.6 MeV, an energy spread of 396 keV, a horizontal size of 5.3 mm and a vertical size of 1.8 mm. When the strength of the quadrupole (marked as k) increases, the horizontal emittance is reduced by 50% and then increases. The two curves scaled on the secondary vertical axis, named "overlap ratio" will be explained in the following paragraphs.

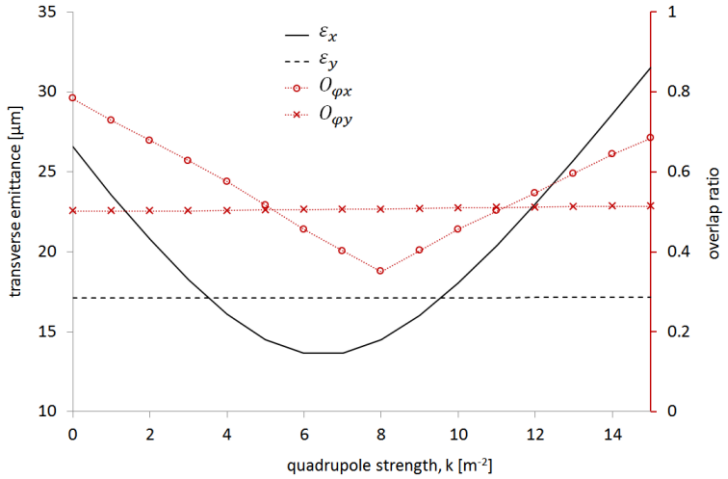

Fig. 2.6 Transverse emittance variation induced by one single quadrupole. $O_{\varphi x}$ and $O_{\varphi y}$ are the horizontal and vertical overlap ratio respectively. The overlap ratio shows similar trend as that of the bunch emittance.

The strength of the quadrupole is denoted by k:

$$k = qg/p \tag{2-5}$$

where q is the charge of the electron, g is the field gradient in the quadrupole and p is the momentum of the bunch. Similar emittance variations with respect to the quadrupole strength have also been observed and well analyzed [64], where the chromatic-induced emittance is estimated to be:

$$\varepsilon_c = (kl)^2 \sigma_u{}^4 (\sigma_E/E)^2 \tag{2-6}$$

where l is the effective length of the quadrupole. The bunch is assumed to have the minimum emittance with the quadrupole strength of zero and the energy spread is assumed to be uncorrelated to TPS.

From Equation (2-6), the chromatic-induced emittance is proportional to the 4th order of beam size. That explains why the emittance variation is much more obvious in the x direction than the y direction in Fig. 2.6, where the transverse beam radius is roughly three times the vertical radius.

To demonstrate how emittance variation is caused by slice mismatch in detail, the bunch is divided into 100 slices by energy, making each slice quasi-monenergetic. Slice emittance is calculated for all slices with different quadrupole strengths, as shown in Fig. 2.7. The small slice emittance at the head and the tail of the bunch is due to low particle numbers of these slices. For each individual slice, the emittance variation is negligible compared to that of the whole bunch.

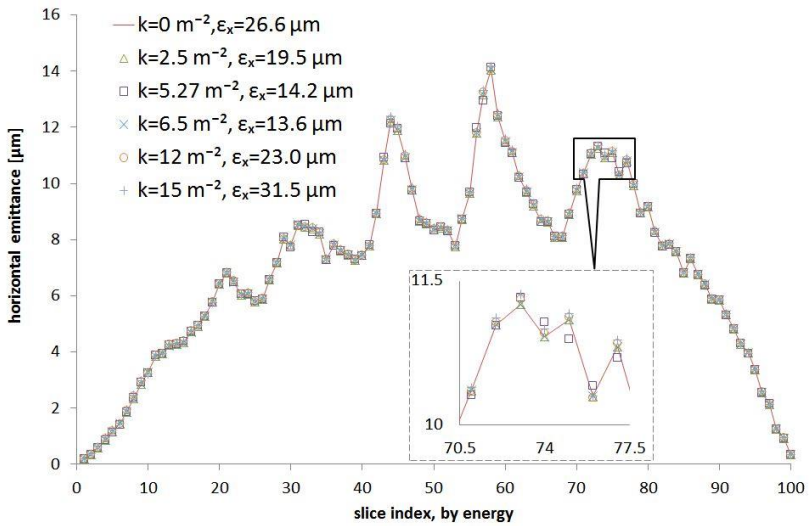

Fig. 2.7 Slice emittance for different quadrupole strengths (k). The emittance of the bunch is listed in the legend. It shows that although the bunch emittance changes with the quadrupole strength, the slice emittance stays almost constant.

To investigate how the "slice mismatch" acts on the transverse emittance, it is necessary to quantify the overlap between slices. Generally, "beta mismatch" and "mismatch phase" have been defined to represent the proportion difference and the orientation difference of any two ellipses in a transverse phase space [42]. The ellipses can represent slices, bunches or even design optics. Similarly, a Twiss-parameter-based definition of the "mismatch parameter M" was used in literature [65]. As defined in Section 2.2, the concepts of the mismatch phase φ_u, the normalized mismatch phase φ_{unor} and the overlap ratio $O_{\varphi u}$ are applied in this thesis.

φ_u is normalized by $\sigma_{\varphi u}$ in order to compare the mismatch phase along the beamline. As slices will rotate in drift spaces, the absolute value of φ_u depends strongly on the observation location. $O_{\varphi u}$ parameterizes the degree of overlap for all slices, as shown on the secondary vertical axis in Fig. 2.6 which exhibits the same trend as the bunch emittance.

It is more intuitive to explain the definition of the overlap ratio $O_{\varphi u}$ in Fig. 2.8, where normalized mismatch phases of the 100 slices with different quadrupole strengths are presented. In spite of undulations on the curves, it can be seen how mismatch phase influences the emittance: For large and small k values (e.g., k = 0 m^{-2} & k = 15 m^{-2}), the mismatch phase changes monotonically with slice index, implying that slices rotate in the same direction over the entire bunch, leading to a larger emittance. However, for moderate values of k (e.g., k = 6.5 m^{-2} & k = 5.27 m^{-2}), the rotation of slices reverses in the middle of the bunch, i.e., the tail of the bunch overlaps with the head in TPS therefore the emittance is smaller.

The mathematical expression of $O_{\varphi u}=(\varphi_{umax}-\varphi_{umin})/\sum_{i=1}^{n_s-1}\left|\varphi_{u,i}-\varphi_{u,i-1}\right|$ is proposed to quantitatively interpret how much the rotation reverses and thus how much slices overlap with others. The numerator $(\varphi_{umax}-\varphi_{umin})$ is the orientation range of the actual bunch and the denominator $\sum_{i=1}^{n_s-1}\left|\varphi_{u,i}-\varphi_{u,i-1}\right|$ is the orientation range possible when every slice rotates in the same direction in respect of its former slice. A larger $O_{\varphi u}$ indicates that the actual rotation of all slices is closer to the single-direction rotation which means no overlap, and thus a larger emittance.

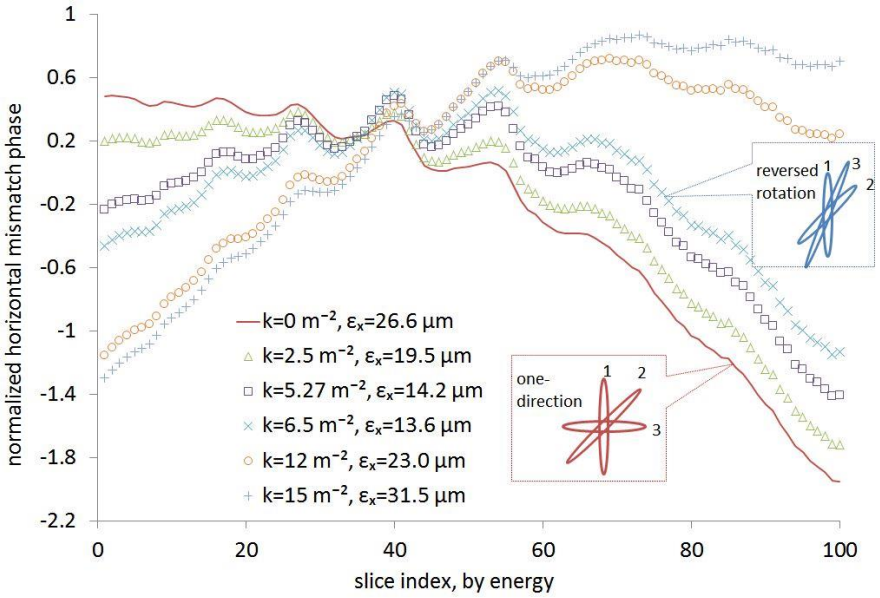

Fig. 2.8 Mismatch phases with different quadrupole strengths (k). The emittance of the bunch is listed in the legend. The mismatch phase is monotonic for small and large values of k in spite of undulations on the curves, while for moderate values of k the trend of the mismatch phase reverses in the middle of the bunch, corresponding to small emittance.

2.5.2. Coherent Synchrotron Radiation (CSR)

In bending magnets, electron bunches emit radiation into a cone towards the tangent direction of the beam. The radiation propagates in the vacuum chamber and on a straight path at the cone edge it will catch up with front electrons in the same bunch that travelling along the dipole arc. In the final portion of a dipole, the radiation can also propagate further into the connecting drift tube.

If the electron bunch is short enough, the radiation becomes coherent at wavelengths comparable to the bunch length and generates an energy modulation over the bunch. The energy modulation then becomes modulations of the orientation (exemplified in Fig. 2.8) or the transverse kick on slices, leading to different projected bunch emittance, formularized by Equation (2-7). Depending on the incident beam, it is not necessary for the projected bunch emittance to be always enlarged by this effect. The impact of the dipole-induced radiation on the quality of the electron beam is referred to as the Coherent Synchrotron Radiation (CSR) effect, illustrated in Fig. 2.9. The calculation of the CSR effect in Elegant for dipoles and connecting drift spaces has been presented in Reference [66]. For incident beams with perfectly overlapping slices, the enlarged emittance is given by [67]:

$$\varepsilon_{CSR} = \varepsilon_{inc}\sqrt{1+\frac{\eta_u^2+(\beta_u\eta_u'^2+\alpha_u\eta_u)^2}{\beta_u\varepsilon_{inc}}\cdot\left[\left(\frac{\sigma_E}{\overline{E}}\right)_{CSR}\right]^2} \qquad (2\text{-}7)$$

where ε_{inc} is the emittance of the incident beam, η_u is the energy dispersive function, η_u' is its first derivative with respect to the curvilinear longitudinal coordinate and $(\sigma_E/\overline{E})_{CSR}$ is the CSR-induced rms relative energy spread.

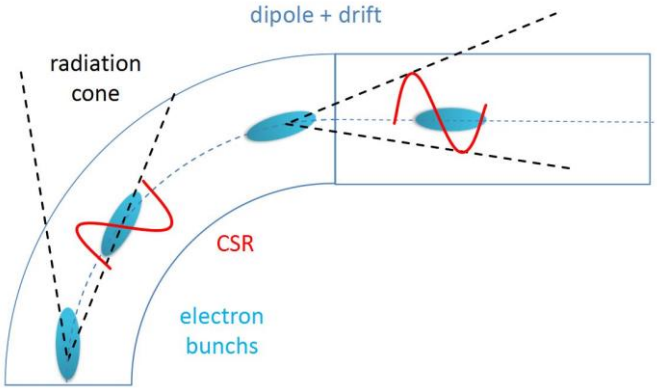

Fig. 2.9 The illustration of the CSR effect in dipoles and connecting drifts.

As part of the ELBE accelerator beamline, two 4-dipole D-shape chicanes are installed to compress the bunch. Besides, several bending dipoles are used to guide the beam to targets. the CSR effect is included in simulations for all dipoles and the connecting drifts right after dipoles. As the bunch will be compressed to be very short in chicanes, there the CSR effect is of more interest compared to that in bending dipoles.

The above influence of CSR on bunch emittance is not completely suitable for chicanes, since the temporal structure of the bunch is strongly changed by chicanes and hence, temporal slices do not stay constant. The mixing between slices results in an increase of the slice emittance as well as the bunch emittance. However, in spite of the energy modulation in the bunch, the energy distribution in general is very similar through the chicane. Therefore the bunch is sliced by energy, which is also consistent with the analysis of slice mismatch in quadrupoles, presented in Section 2.5.1.

Simulations show that the impact of CSR on the longitudinal phase space is negligible, but the irreversible growth of the average slice emittance has been observed. As an example, a 500 pC electron bunch transported through a 4-dipole D-shape chicane with an energy of 14.3 MeV, a bunch length of 7 ps, an energy spread of 377 keV, a horizontal size of 5.8 mm and a vertical size of 2.6 mm, is studied for five cases: no compression (chicane turned off); maximum compression with/without CSR; and over compression with/without CSR. The

interest in the over compression cases will be further discussed in Section 2.8.1. For all of the five cases studied, the bunch emittance, the slice emittance and the overlap ratio are presented in Fig. 2.10.

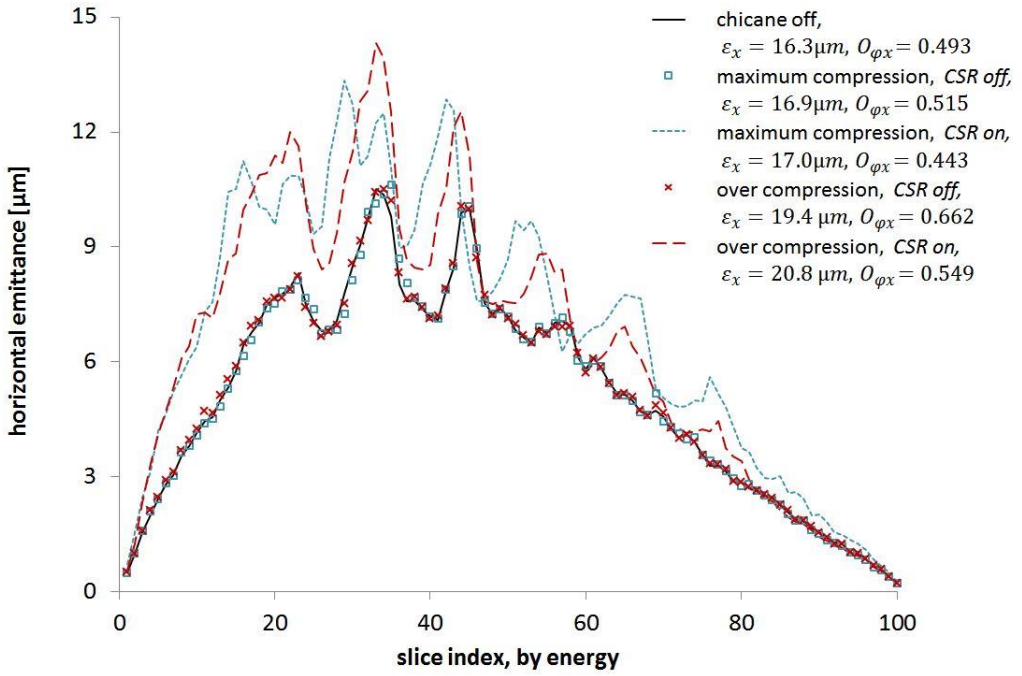

Fig. 2.10 The influence of the CSR effect in a chicane for maximum compression and over compression. $O_{\varphi x}$ and $O_{\varphi y}$ are the horizontal and vertical overlap ratio respectively. If the CSR effect is turned off, the slice emittance stays the same in both maximum compression and over compression. Furthermore, it is not necessary to increase the emittance more for the over compression compared to maximum compression.

The maximum compression happens at the bending angle of 11.8°, where the bunch length is compressed from 7 ps to 0.7 ps. When CSR is included in the simulation, the bunch energy is reduced by 60 keV while the energy spread remains the same. In the over compression cases with a bending angle of 18° and an output bunch length of 9.7 ps, CSR reduces the energy by 20 keV and decreases the energy spread slightly by 6 keV. As the total energy of electrons and the radiation should be conserved, the smaller energy-decrease in over compression cases indicates a weaker CSR. Although the over compression with a larger bending angle leads to stronger incoherent synchrotron radiation, it also increases the bunch length and the horizontal size. Consequently, the reduced charge density results in less intensity of coherent radiation.

The weaker CSR is also evident in the simulation results of the slice emittance. When the CSR effect is turned off, the slice emittance becomes independent of the bending angle. In contrast, the slice emittance increases in those cases when the CSR effect is considered. Moreover, compared to the maximum compression, the over compression leads to a larger

bunch emittance and a larger overlap ratio, but not necessarily results in the growth of the slice emittance. The average slice emittance is 6.05 μm, 8.22 μm, 7.70 μm respectively in the cases of no compression, maximum compression and over compression.

In addition to different orientations of the slices, their horizontal movement due to the CSR field is another reason for the emittance growth, especially in circular accelerators. However, as the main function of a chicane is to change the temporal structure of bunches, temporal slices become mixed. This is referred to as "phase mixing" which can explain the growth of the slice emittance [68].

2.5.3. Longitudinal Space Charge (LSC) effect

Longitudinal space charge (LSC) has an important impact on the energy spread of the bunch. Generally speaking, the head of the bunch gains energy and the tail loses energy. The initial density modulation normally results later in energy modulation. For the ELBE accelerator and its analogs in the energy regime below 1 GeV, the LSC effect in long beamlines can damage the desired longitudinal phase space, unless transport schemes which compensate for this effect are applied.

To address this, the LSC effect is included in Elegant [69]. A 47 m linear beamline from ELBE without cavities and chicanes is selected to determine the influence of the LSC effect. The input bunch has an energy of 24.5 MeV, a bunch length of 1.7 ps and an energy spread of 394 keV, with a negative energy chirp in which the head of the bunch has a lower energy than the tail. The bunch charge is scanned from 0 to 500 pC and the results are shown in Fig. 2.11

Although the bunch is quasi-relativistic with a speed of 0.9998c, the bunch length at the ps level is still sensitive to the velocity compression. When the bunch charge is increased, the LSC effect becomes stronger and the energy spread is reduced, as a resuly the velocity compression is weaker.

The energy spread after the bunch compression should be carefully chosen to compensate the LSC effect in the following beamline, such that the energy spread of the bunch at target position can be minimized. From another perspective, the LSC effect reduces the energy spread that is needed for dispersive bunch compression schemes.

However, the minimum energy spread is limited by the nonlinearity of LSC effect, which leads to a nonlinear distribution in longitudinal phase space after the long drift. Note that

when the bunch is 3D-ellipsoidally distributed, the LSC effect is linear and the correlated energy spread can be compensated completely [65].

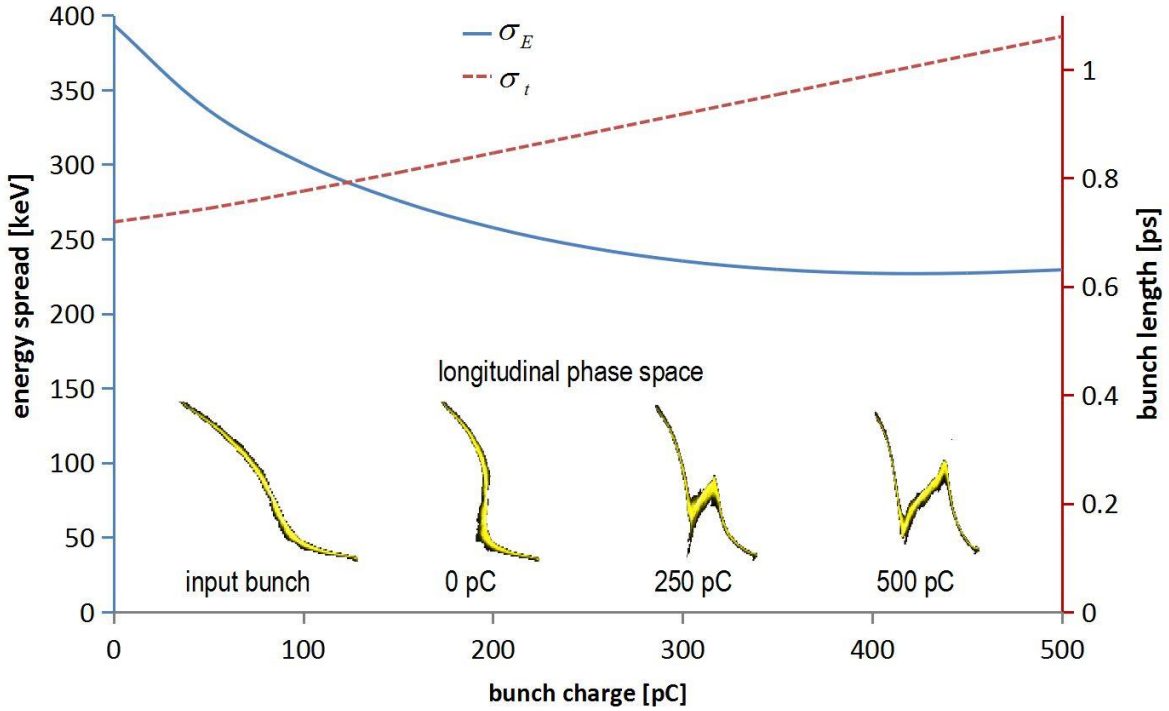

Fig. 2.11 The influence of the LSC effect on energy spread and bunch length for a 47 m linear beamline with different bunch charges. Higher bunch charge results in a compensated energy spread and less velocity compression.

2.5.4. Short range longitudinal wake effect

When an electron passes through an accelerator section, a movement of electrons on inner surfaces of the section will be induced. Later the surface-electron movement oscillates and the field inside the section oscillates correspondingly. The oscillating field is normally calculated by introducing the mirror charge. As the field oscillation is similar to the generation of a wake in liquid, this field is called “wake field”. The wake field will affect the following electrons, resulting in an impact on beam quality, which is represented by the term of “wake effect” [70,71].

In a uniform tube, the wake effect comes from the impedance of the surface resistance, which vanishes in perfect conductors. While in a complicated structure, the geometry contributes the main part of the wake effect.

The wake effect decays with time after the source electron passes through. For a typical electron beam in ELBE, the bunch length is several pico-seconds while the period of bunches is 77 ns at 13 MHz. Hence, it is assumed that the wake effect within the same bunch is much

more important compared to that between bunches. The wake effect within the same bunch is called “short range wake effect.”

The longitudinal impact of wake fields is reflected in an energy reduction, as well as a different energy distribution. In following simulations only the short range longitudinal wake effect is considered and the “wake effect” is used as the abbreviation of the “short range longitudinal wake effect”, or indicated otherwise.

The wake effect on a single particle comes from a large number of particles in front of it. To solve the energy change of a particle numerically is computationally complex, depending on the structure of the beamline section and the distribution of the bunch. However, considering that the overall energy change is the sum of that from individual particles, the Wakefield effect from a unit point charge can be calculated, for only once, and then applied for any charge distributions.

Assume a unit point charge passing through a fixed structure with relativistic speed, and set $G(t)$ as the wake-effect-induced energy kick on another unit point charge travelling behind with a time lag of t, then the energy kick from a point charge Q_1 on another point charge Q_2 can be written as:

$$dE(Q_1,Q_2,t) = Q_1 Q_2 G(t) \tag{2-8}$$

Assuming that the source charge has a distribution of $Q_1(t)$, the total charge is still Q_1, then the energy kick is:

$$dE(Q_1(t),Q_2,t)=Q_1 Q_2 \cdot W(t) \tag{2-9}$$

where

$$W(t) = \int_{-\infty}^{\infty} Q(\tau)\, G(t-\tau) d\tau \tag{2-10}$$

is called “wake potential”, which is the energy kick per charge on a following unit charge and has the fundamental unit of V/C. The wake potential is the convolution of the charge distribution and the energy kick between the two unit point charges.

Furthermore, the energy kick on a bunch with a charge distribution $Q(t)$, a total charge of Q_t from the bunch itself is given by:

$$dE(Q(t),t) = Q_t Q(t)\, W(t) = Q_t Q(t) \int_{-\infty}^{\infty} Q(\tau)\, G(t-\tau) d\tau \qquad (2\text{-}11)$$

Equation (2-9), Equation (2-10) and Equation (2-11) indicate that the complexity of the geometry is represented by the unit energy kick between the two unit point charges, $G(t)$. $G(t)$ is called "wake function" and also has the fundamental unit of V/C. In some simulation codes such as Elegant, $G(t)$ is also called "Green's function", as usually it has the form of a Green's function mathematically. $G(t)$ depends only on the geometric and electric boundaries of the beamline section. If the Green's function of a particular structure is calculated, then the self-energy-kick of any charge distribution can be calculated according to Equation (2-11).

In Elegant, the wake effect is calculated by introducing a Green's function for a beamline section and convoluting it with the longitudinal charge distribution. Normally the calculation of the wake potential is usually performed in the frequency domain, where for a point charge infinite modes of wake fields are excited, making the calculation impossible. The method of obtaining the Green's function applied here is to deconvolve the wake potential and the corresponding charge distribution.

In ELBE accelerator, wake effects come from the impedance of inner surfaces of beam pipes and the irregular geometry borders of screen-stations, cavities, couplers and bellows. The wake effect for screen-stations has been studied with CST and elegant, as they are the largest in number (e. g., 31 stations from the SRF gun to the CBS experiment station) and their structures have sharp edges at tube connections.

The wake potential is calculated by Andre Arnold (HZDR) using CST, for Gaussian distributed bunches with different bunch lengths of 1.5 mm and 3 mm. Screen-stations are symbolized by a 3D cross model as shown in Fig. 2.12, with perfect conducting material as boundaries.

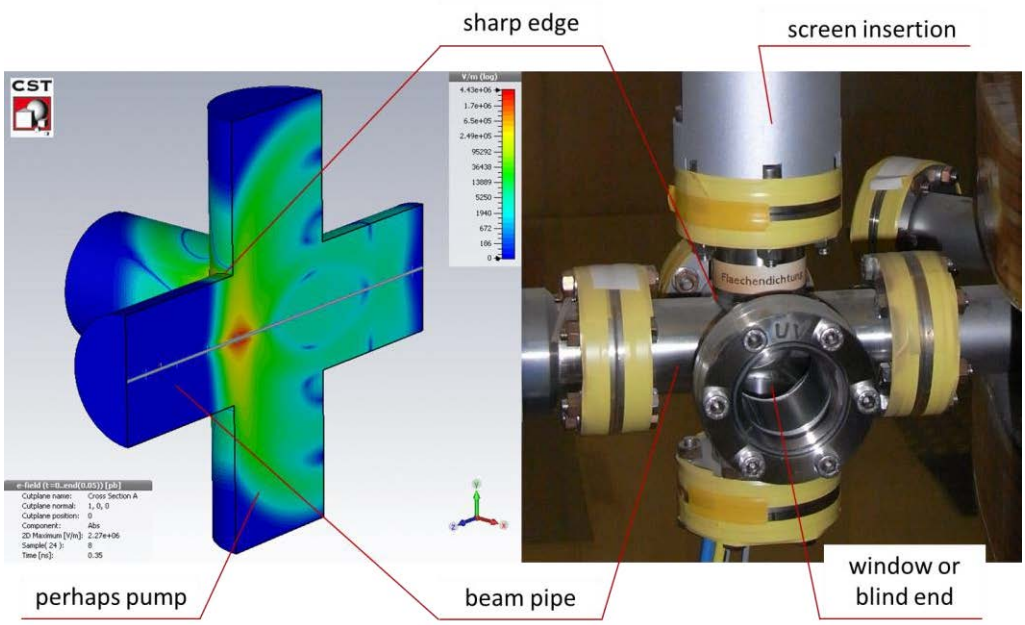

Fig. 2.12 Simplified geometries of screen-stations (left) and a typical screen-station in ELBE (right).

The wake potential is calculated up to 100 mm from the head of the bunch, covering all possible bunch lengths in ELBE, as shown in Fig. 2.13.

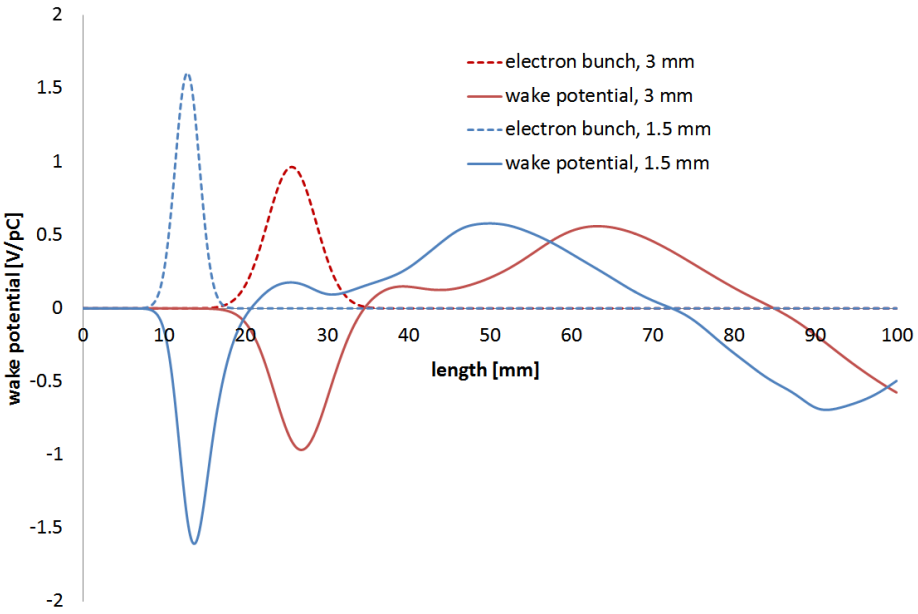

Fig. 2.13 Wake potentials and corresponding charge distributions for different bunch lengths. The wake potentials are simulated by Andre Arnold, with CST.

The deconvolution of wake potential is based on Fast Fourier Transform (FFT). Using the symbol "$*$" to present the convolution, the following equation holds generally:

$$\mathrm{F}\big(\mathrm{Q(t)}*\mathrm{G(t)}\big) = \mathrm{F}\big(\mathrm{Q(t)}\big)\cdot\mathrm{F}\big(\mathrm{G(t)}\big) \tag{2-12}$$

where F is the FFT operation, Q(t) and G(t) are the charge distribution and the Green's function respectively. As a matter of fact, Equation (2-12) also holds for any two functions of t. From Equation (2-10) and Equation (2-12), the Green's function can be calculated by:

$$G(t)=F^{-1}\left[\frac{F(W(t))}{F(Q(t))}\right] \tag{2-13}$$

F^{-1} is the inverse operation of FFT. In numerical computations, the FFT based deconvolution is interfered by noise. As the Fourier transform appears in the denominator of Equation (2-13), small errors will be amplified to tremendous values in the frequency domain of the Green's function. A method of suppressing the noise by calculating the quasi-Green's function has been introduced in Reference [72] which is applied here.

In this thesis, it is also found that the deconvolved Green's function is sensitive to the interpolation number of W(t) and Q(t), shown in Fig. 2.14. The strategy of determining the best interpolation number here is to convolve different Green's functions with the bunch distribution of another bunch length, and then compare the convolved wake function to the simulated one from CST. The best quasi-Green's function is identified by finding the minimum absolute difference between convolved and simulated wake functions, as shown in Fig. 2.14.

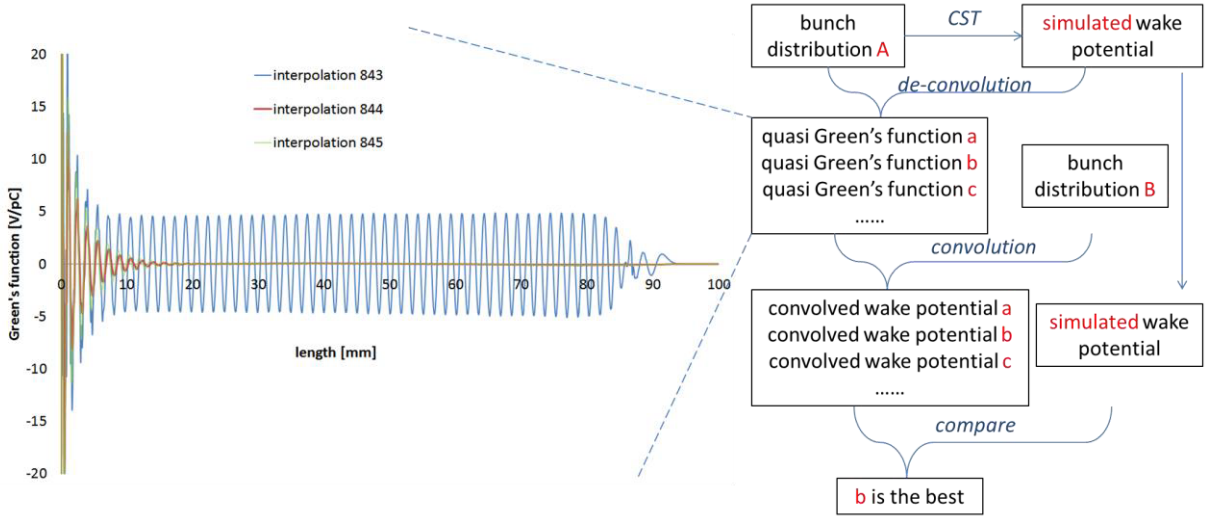

Fig. 2.14 Green's functions deconvolved with different interpolation numbers (left). Illustration of how to determine the best interpolation number (right).

The best Green's function deconvolved from the 1.5 mm bunch and its wake potential is later convolved with the 3 mm bunch and the result is compared with CST simulations.

Similarly, the best Green's function from the 3mm bunch is convolved to compare with the wake function from the 1.5 mm bunch. Results are shown in Fig. 2.15.

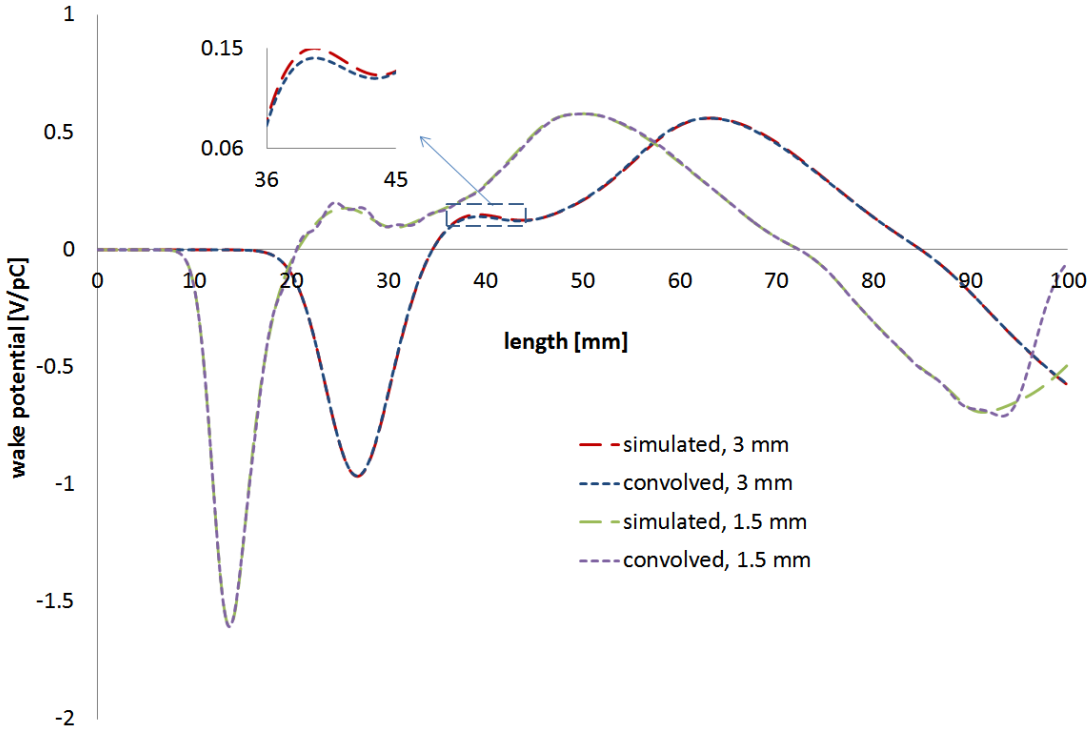

Fig. 2.15 Simulated and convolved wake potentials of both 1.5 mm and 3.0 mm bunches. The difference is negligible in the 3.0 mm case, where a Green's function deconvolved from the 1.5 mm case is used and thus chosen as the quasi-Green's function for simulations in this thesis. It is represented by the red curve in Fig. 2.14.

After the comparison between simulated and convolved wake functions, the quasi Green's function as the red curve in Fig. 2.14 is chosen to represent the real Green's function for the 3D cross model of screen-stations. For instance, for an 80 m transport with 31 screen-stations, the energy loss of a 24.5 MeV electron bunch is only some tens of keV. Nevertheless, the wake effect for screen-stations is still taken into account in simulation.

2.5.5. Simplex optimization

Elegant can optimize beamline parameters by maximizing/minimizing a function of beam quality parameters. One of the recommended optimization methods is the "simplex optimization" [73], which is applied in simulations of this thesis.

The automatic simplex optimization has been used for finding proper strength values for quadrupoles and the superconducting solenoid, as well as distances between permanent magnet quadrupoles of FFS. Normally a beamline section including less than 6 parameters is selected according to calculation time, and the following function is to be minimized:

$$f_{op} = w_u \max(\sigma_x,\sigma_y) + w_{u'} \cdot \max(\sigma_{x'},\sigma_{y'}) + w_\varepsilon \cdot \max(\varepsilon_x,\varepsilon_y) + 100 w_u |\sigma_x - \sigma_y| + 100 w_{u'} |\sigma_{x'} - \sigma_{y'}| + 100 w_\varepsilon |\varepsilon_x - \varepsilon_y| \quad (2\text{-}14)$$

where w_u , $w_{u'}$ and w_ε are the user-defined weighting factors of beam size, beam divergence and transverse emittance respectively. max( ) is to choose the larger value in parentheses, realized by the following equation, but in the reverse Polish notation (rpn) format which is required by Elegant:

$$\max(a, b) = \frac{a}{2} + \frac{a}{2} \cdot \left(\frac{|a-b|}{a-b}\right) + \frac{b}{2} + \frac{b}{2} \cdot \left(\frac{|a-b|}{a-b}\right) \quad (2\text{-}15)$$

where a and b represent any two values.

Whether or not to include the last three terms in Equation (2-14) can be customized by users. E. g., if a round beam is desired, the term $100 w_u |\sigma_x - \sigma_y|$ should be included. f_{op} satisfies most demand of transverse beam transport. Usually the optimization should be performed repetitively so that the weighting factors can be iteratively improved, i. e., to increase the weight if the optimized corresponding term (size, divergence or emittance) is still too large. When a chicane is included in the optimization, it usually requires large w_ε to control the irreversible slice emittance growth. However, for magnets in FFS, only w_u should be non-zero because the only purpose of beam transport is to generate small a beam size.

2.6. LabVIEW based simulation tool

2.6.1. Functions

A LabVIEW based simulation tool has been developed to simplify the operation of simulations. Fixed parameters of ELBE are set in the simulation tool, while other changeable parameters can be input by users. ASTRA and Elegant are executed subsequently, where the output data from ASTRA are automatically transferred to the input file of Elegant. Other functions are programed with LabVIEW, including plotting and saving results properly, scanning parameters and setting optimization requirements. The interface of the simulation tool is shown in Fig. 2.16.

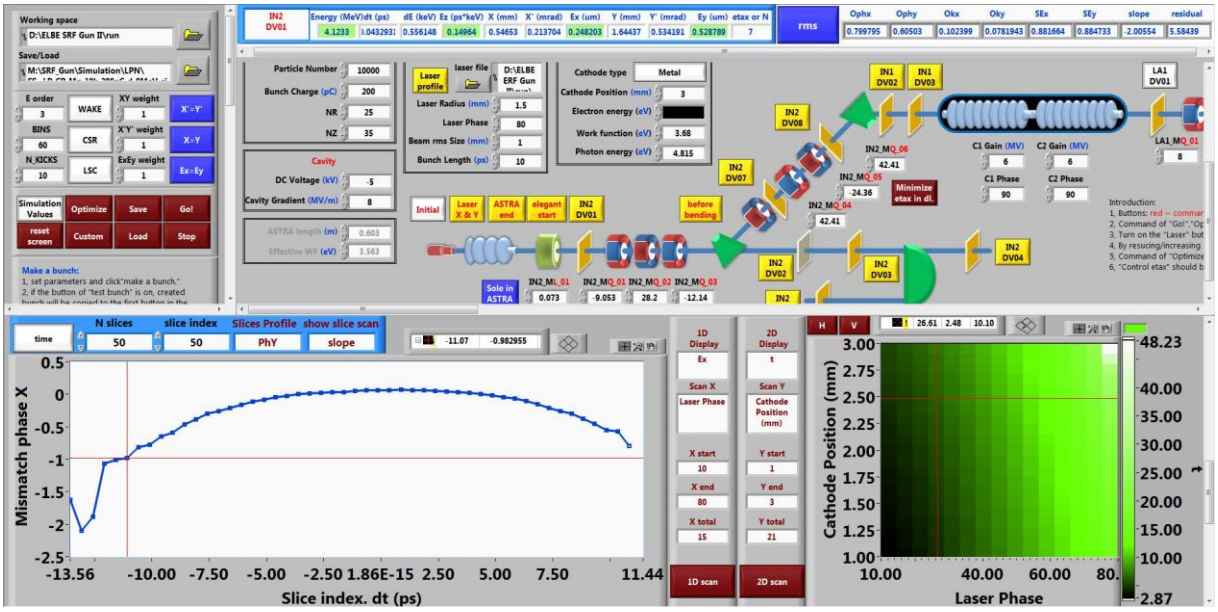

Fig. 2.16 The simulation tool for ELBE SRF Gun II and the ELBE accelerator. The left-upper subpanel contains action buttons and toggle switches. The right-upper subpanel is the sketch of the ELBE accelerator, showing currently the SRF gun, the dogleg and the first linac. The bottom panel presents the results including phase spaces, beam size/emittance profiles, sliced parameters and the parameter scanning. What is shown here is the sliced energy spread on the left, and the result of a 2D parameter scan in the color chart on the right.

The simulation tool covers the beamline from the SRF gun to the four high-bunch-charge experimental stations introduced in Section 1.3: pELBE, nELBE, TELBE and CBS. The entire beamline can be visited using scroll bars as shown in Fig. 2.17.

Fig. 2.17 The beamline included in the simulation tool.

Yellow buttons on the interface are screen-stations or important positions of the beamline, where a data file containing 6D coordinates of all particles will be created after each simulation. The program takes the beamline between the first two turned-on yellow buttons as the section to be simulated. All needed input files of ASTRA and Elegant will be created according to the user-input parameters of this beamline section. The incident bunch is loaded from the 6D coordinates file which is saved from previous simulations, or defined by providing all necessary statistical average parameters, e. g., emittance, beam size and energy spread. If the simulation starts from the beginning of the cathode, an initial bunch will be generated by emission models presented in Section 2.4.1. By double clicking yellow buttons, parameters defined in Section 2.2 for both the entire bunch and slices are calculated and shown altogether with the phase space histogram. The entire result panel is shown in Fig. 2.18.

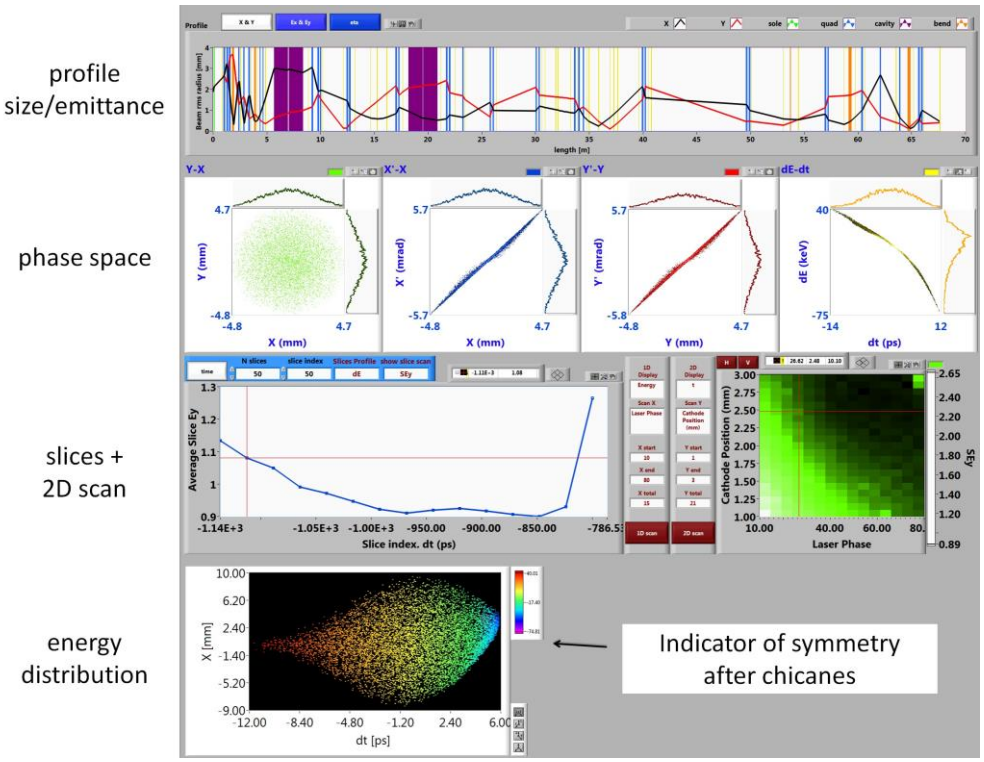

Fig. 2.18 The entire result panel of the simulation tool.

Blue buttons are toggle switches, e. g. for turning on/off CSR, LSC and the wake effect. Red buttons are command buttons, with functions including executing a single simulation, optimizing a beamline section, scanning parameters, saving/loading and so on.

The parameters of magnets used in simulation can be transferred to operational current values according to the individual design of those magnets. The transformation needs the beam energy therefore a simulation must be executed first.

Simulations in ASTRA run slower than those in Elegant. After every execution of ASTRA the outcome file of complete particle coordinates is saved with the filename containing all relevant parameters. If the same combination of parameters is found from saved files, ASTRA will not start, while instead, the saved file will be read into memory for further simulations.

The scan function includes setting one or two parameters for scanning as well as the scanning range and step. In the simulation tool, every decrease/increase of a numerical parameter triggers the command that making this parameter the first/second to be scanned. The scanning is composed of multiple simulations according to the scanning range and step.

The optimization has been introduced in Section 2.5.5. All relevant parameters in the selected beamline section will be optimized. If a parameter should be fixed instead of optimized, by double clicking, its background color will be changed to red and it will be ignored in the optimization.

2.6.2. Highly adaptable design

In addition to realizing the functions introduced in Section 2.6.1, the simulation tool has also been developed with the possibility of extension to various beamlines, based on case structures in LabVIEW.

A beamline table is written to define the order of elements used in simulation. Names, types, physical lengths and positions of elements are recorded to generate necessary input files for ASTRA and Elegant. The names of elements are the same to buttons and numerical parameters in the front LabVIEW panel. In a simulation, the program will search in the beamline table for the first two turned-on buttons and establish the beamline section with all elements between these two buttons. Branches of the beamline are marked with the element "tree".

If a new section of the beamline is added to the simulation tool, its elements should be first inserted to the beamline table with the correct order. After that, the corresponding yellow screen buttons with the same names and numerical parameters representing magnets and cavities should be created in the front panel of the program. In addition, the newly created buttons and numerical parameters should be added to the defined cases in the back panel. The cases include "double clicking buttons", "double clicking numerical parameters" and "numerical parameters value change". As described in 2.6.1, the case of "double clicking buttons" triggers the presentation of the bunch at the corresponding button. The case of "double clicking numerical parameters" includes/excludes the numerical parameter in the

optimization. The case of “numerical parameters value change” triggers the selection of parameters for scanning. With all of the new buttons and numerical parameters added into the above three cases, extension of the new beamline is finished.

In order to save or load all relevant parameters without coding for newly added elements, every time a numeric or button is used in simulation, its name and value are saved in two global arrays. Saving/ loading is realized by transferring data between these two global arrays and an external file. In this case, the command of “save” or “load” always affects all parameters used in simulation.

2.7. Optimization of gun parameters

During operations of ELBE SRF Gun II, the gradient of the gun-cavity is usually set to the possible maximum value. The power of UV laser is also tuned to its maximum but the proportion transported to the cathode is changeable using a wave plate and a polarizer to generate the desired bunch charge. The SC solenoid should be adjusted together with quadrupoles to minimize beam-loss of the entire beamline.

In addition, other parameters which should be optimized according to users' requirements include DC voltage, laser spot size, laser pulse length, laser phase and cathode position, as illustrated in Fig. 2.19. The dependence of beam quality on these free parameters has been studied with ASTRA-based simulations, as well as to determine their values for high-bunch-charge applications.

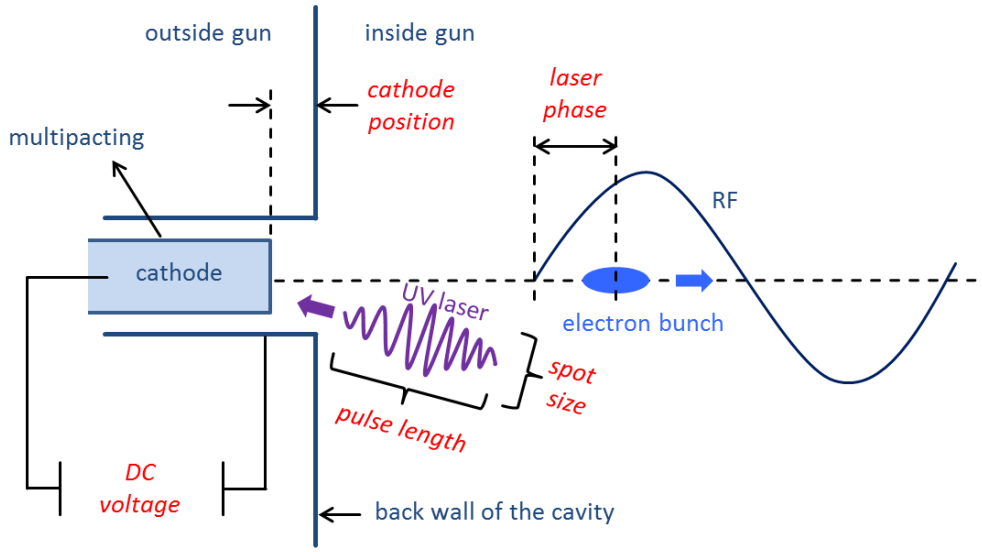

Fig. 2.19 Free parameters of the ELBE SRF gun.

2.7.1. DC voltage

DC voltage is the voltage applied between cathode and cavity (ground level) to suppress multipacting [74]. Fig. 2.5 indicates that the strength of DC fields is one magnitude lower than that of RF fields at the surface of the cathode and decays in a few millimeters, therefore the influence of the DC voltage on the energy gain is negligible compared to RF fields.

In light of a measurement described in Section 4.2 showing that a positive DC voltage reduces the transverse emittance, SRF gun settings with different DC voltages are simulated and analyzed, as shown in Fig. 2.20. The applied gradient of the cavity is 8 MV/m, the bunch charge is 200 pC, the cathode position is 1.4 mm, the bunch is uniformly distributed

transversely with an overall diameter of 4 mm and Gaussian distributed longitudinally with an rms bunch length of 7 ps. Different laser phases are scanned with different DC voltages.

The laser phase for the maximum beam energy decreases with the DC voltage. This phenomenon can be interpreted as an accelerating field (negative DC voltage) pushing electrons to catch up with earlier RF fields, which is equivalent of a smaller laser phase.

Fig. 2.20 also shows that generally the simulated electron bunch becomes longer when the DC voltage increases. larger bunch length reduces the space charge density, and hence, the space charge force. As a result, a smaller emittance with positive DC voltage is also observed in simulation, which is consistent with measurements.

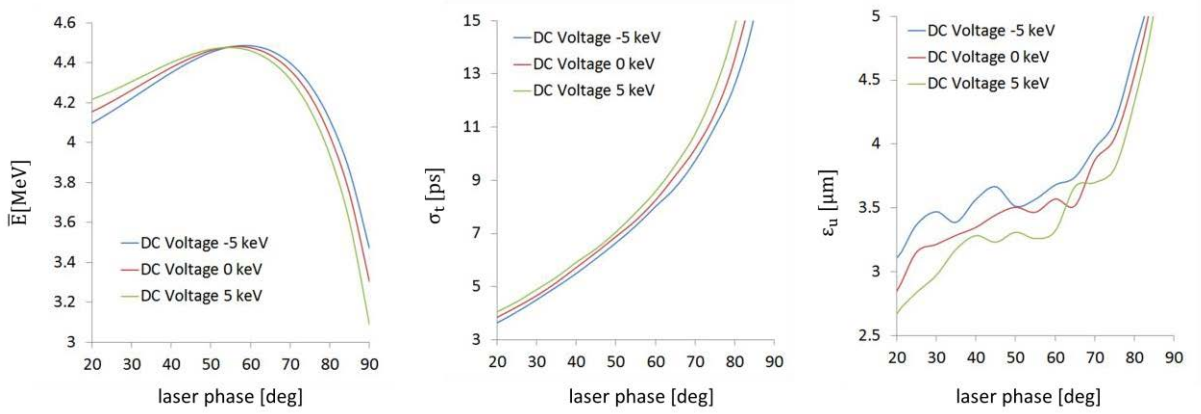

Fig. 2.20 The impact of the DC voltage on beam quality at difference laser phases. The effect of the DC voltage on the energy is equivalent to pushing/delaying the bunch to a different laser phase. Positive DC voltages lead to longer bunches (weaker space charge forces) and thus smaller emittance. Parameters used in this simulation: the gradient is 8MV/m, the bunch charge is 200 pC, the cathode position is 1.4 mm, the laser spot size is 4 mm of overall diameter and the bunch length is rms 7 ps.

2.7.2. Laser spot size

In simulation, the spot size of the laser is expressed by its overall diameter, which is about 3.6 times of the rms size for a round, flattop distributed laser spot. It initializes the transverse size of electron bunches and directly affects the space charge density for a fixed bunch charge. A larger spot size corresponds to a larger thermal emittance, meanwhile the space charge density is reduced and induces smaller transverse emittance growth. The balance between thermal emittance and space-charge-induced emittance growth depends on the bunch charge, the gradient of the cavity, the cathode position and also the bunch length.

Fig. 2.21 shows simulated beam quality while the laser spot size and the laser phase are scanned for a magnesium cathode. In the simulation, the laser pulse length is 7 ps, the cathode

position is 1.6 mm, the DC voltage is 5 keV, the bunch charge is 200 pC and the gradient is set to both 8 MV/m and 18 MV/m for comparison.

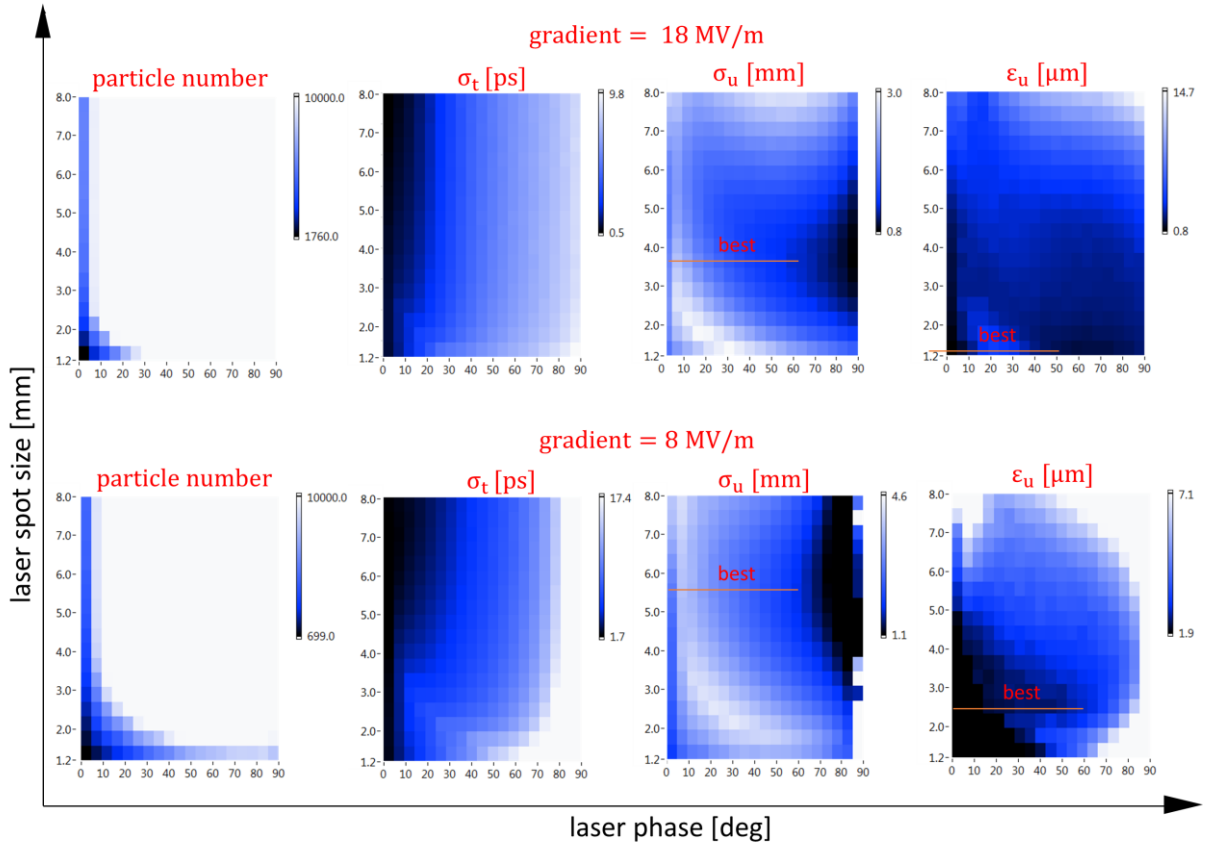

Fig. 2.21 The impact of laser spot size on beam quality. Parameters used in this simulation: the bunch charge is 200 pC, the DC voltage is 5 keV, the cathode position is 1.6 mm and the bunch length is rms 7 ps.

The diagrams for “particle number” in Fig. 2.21 indicate areas without beam-loss in the 2D parameter map. Except for these areas, the bunch length decreases with laser spot size. The laser spot size for the best bunch size is different to that for the best emittance. At the gradient of 18MV/m, the laser spot size of 3.8 mm is the best for emittance and 1.2 mm is the best for bunch size. At the gradient of 8 MeV, the space charge effect is stronger therefore larger laser spot sizes with overall diameters of 5.5 mm and 2.5 mm are needed for achieving the best bunch size and emittance respectively.

In practice, photocathodes for ELBE SRF Gun II are 10 mm in diameter and the coated/cleaned areas for Cs2Te/Mg cathodes are less than 8 mm in diameter. Considering that the geometric center might not be the electric center of the gun, i. e., a deviation of laser spot from the cathode center might be required, the diameter of the laser spot is set to 4 mm, which satisfies requirements of beam transport in the following simulations.

2.7.3. Laser pulse length

The pulse of the UV laser is Gaussian distributed longitudinally, with the pulse length expressed by rms values in this section. The laser pulse length strongly affects the space charge density and thus longer pulses are desired. However, longer pulses increase the DoN in longitudinal phase space and as a result damage the compression of electron bunches. The balance of the above two conflicting effects varies with bunch charge. Fig. 2.22 provides beam parameters at the exit of the gun-cavity with the rms laser pulse length and bunch charge scanned.

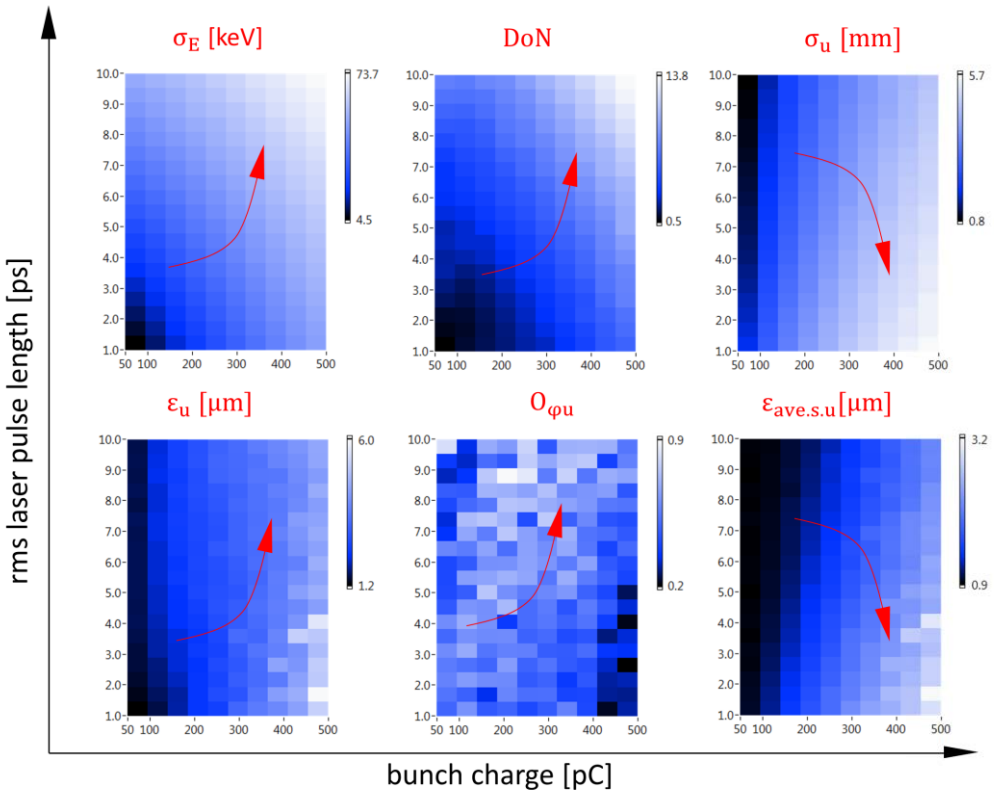

Fig. 2.22 Beam quality with different laser pulse lengths and bunch charges. Parameters used in this simulation: the gradient is 8 MV/m, the cathode position is 1.6 mm, the laser phase is 50°, the DC voltage is 5 keV, the laser spot size is 4 mm of overall diameter.

When the laser pulse length increases from 1 ps to 10 ps, energy spread and DoN of the beam also increase due to the RF field in gun-cavity. Meanwhile, the bunch size decreases as the bunch charge density decreases in longer bunches. The left-bottom diagram shows that the bunch emittance slightly increases with laser pulse length, although the transverse bunch size is smaller. The mechanism can be revealed by examining the overlap ratio of slices which increases with laser pulse length. The emittance of an individual slice should be smaller as the space charge effect is weaker, which is verified by the right bottom diagram of Fig. 2.22

where the trend of the average slice emittance is opposite to that of the bunch emittance and the overlap ratio.

The current rms pulse length of the UV laser is about 7 ps, which is measured in Section 4.1 and set as the default electron bunch length in simulations. Applications of different laser pulse lengths experimentally by changing relevant crystals have been scheduled for future development of the ELBE SRF gun.

2.7.4. Laser phase and cathode position

The laser phase indicates the arrival time of the UV laser at the cathode, quantified by the RF phase. The origin of the RF phase is defined as the moment when the its strength is zero. The RF phase at the moment when the center of a laser pulse hits the cathode is defined as the "laser phase". Laser phase at 90° generates the highest extraction field which compresses the space charge force and therefore benefits the beam size and emittance. But the final energy of electron bunches from the gun is not necessarily maximum at 90°, as electrons are not synchronized to the RF with low energy when just emitted from the photocathode.

The cathode position is the distance between the cathode surface and the backplane of the cavity. As introduced in Section 1.1.3, the cathode is installed several millimeters outside of the cavity to provide an RF focusing near the cathode.

To choose proper parameter combinations of the SRF gun, laser phase and cathode position are scanned and results are shown in Fig. 2.23. In this simulation, the gradient is 7.5 MV/m and the bunch charge is 200 pC. The overall diameter of the uniformly distributed laser spot is 4 mm and the length of the Gaussian distributed laser pulse is 7 ps.

Fig. 2.23a shows the area without beam loss, marked by the red frame. Fig. 2.23b presents the energy distribution where the red frame is based on an additional condition that the energy loss should be less than 10%. A third condition is proposed in Fig. 2.23c that the energy spread should be smaller than 50 keV so that the bunch is not dispersed to hit the dogleg wall. The last condition comes from the inner diameter of ELBE beam pipe which generally requires the rms beam radius to be less than about 5 mm, marked in Fig. 2.23d. Other beam quality parameters have no definite requirements.

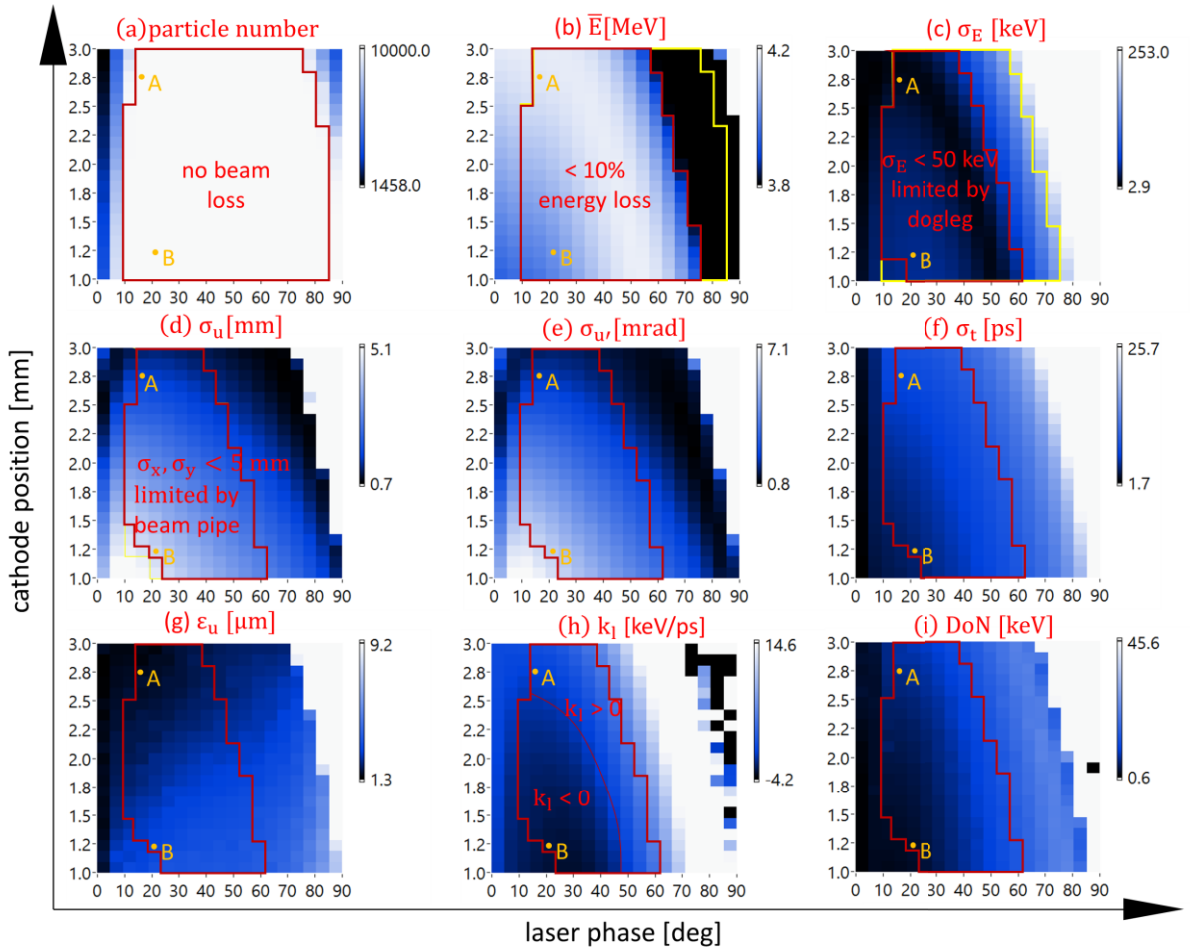

Fig. 2.23 Beam quality with the laser phase and the cathode position scanned. The red/yellow frame marks the current/previous satisfying parameter area. A and B are two candidates for high-bunch-charge applications. Parameters used in this simulation: the gradient is 7.5 MV/m, the bunch charge is 200 pC, the DC voltage is 5 kV, the laser spot size is 4 mm of overall diameter and the laser pulse length is rms 7 ps.

In the parameter map of laser phase (LP) and cathode position (CP) in Fig. 2.23, the high-LP-high-CP corner generates small bunch size and small divergence, however, emittance is the smallest at low-LP-high-CP corner. The phenomenon that low bunch size and low divergence do not lead to low emittance can be also found in Fig. 2.21. Here the reason is illustrated in Fig. 2.24, where with the same CP of 2.8 mm, three LPs of 15°, 40° and 65° are applied and phase spaces are shown. When LP increases, the bunch becomes positively chirped (shown by energy distribution along the bunch in color) and a second component appears at the longitudinal head and tail of the bunch. Although the statistical average bunch size and divergence becomes smaller at high LPs, the emittance becomes larger due to worse overlap of slices in TPS. This is an important reason why large LPs are not chosen for operating the SRF gun.

Low-LP-low-CP combinations in Fig. 2.23 benefit the bunch length as well as the slope and the DoN in LPS. If bunch compression is targeted in beam transport, the beam should be negatively chirped, corresponding to the area marked by $k_l<0$ in Fig. 2.23h.

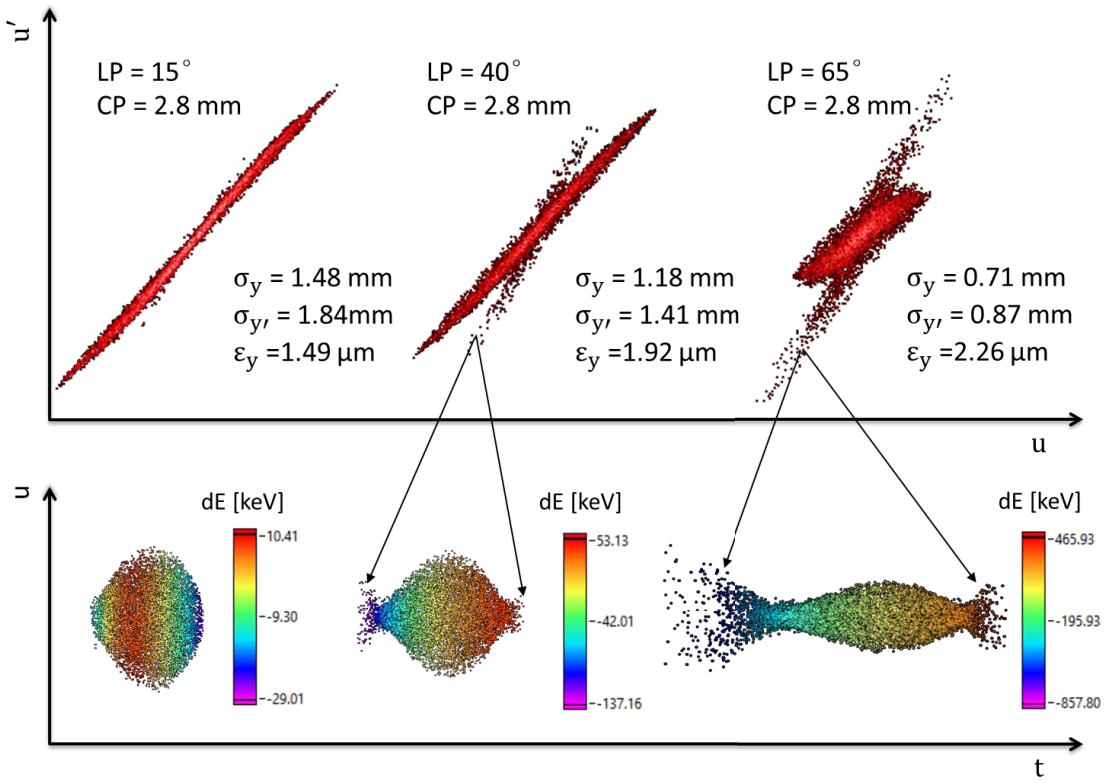

Fig. 2.24 Bunches with lower bunch size and lower divergence can have larger emittance. When the laser phase increases, longitudinal terminals of the bunch behaves differently in TPS compared to other parts of the bunch.

As a result, two combinations of LP and CP have been chosen as candidates for further applications with 200 pC bunch charge, marked as A (LP = 15°, CP = 2.8 mm) and B (LP = 20°, CP = 1.2 mm) in Fig. 2.23. Parameter combination A is chosen for the best transverse beam quality while longitudinal parameters are neglected, which is usually the requirements of pELBE and nELBE. Parameter combination B focuses on optimizing longitudinal parameters for bunch compressing, while transverse beam quality still lies within the satisfying area.

2.7.5. Summary of optimized gun parameters

Given the above studies of the five free parameters based on the current status of ELBE SRF gun, the preferred operation status of the gun for high-bunch-charge applications is summarized in Table 2.1. The phase space at the exit of gun-cavity is shown in Fig. 2.25. Beam quality parameters are listed in Table 2.2.

In Table 2.1, the chosen gradient of 7.5 MeV is close to the maximum long-term stable gradient of the cavity. The bunch charge of 200 pC is set as the current target for high-bunch-charge applications which is a progress compared to the DC thermionic gun (77 pC). This bunch charge has not reached the limitation in simulation if the alignment of the beamline is assumed perfect, as shown in Section 2.8. The DC voltage of 5 keV is chosen to optimize the transverse beam quality. The laser spot diameter of 4 mm is a practical value currently, which can be larger as an enhancement in future if the effective area of the cathode becomes larger and the alignment of the gun is improved. The optimized value for laser pulse length depends on the bunch charge. The current value of 7 ps satisfies all applications of 200 pC in simulation, but a shorter bunch length might be better, which will be addressed in Section 2.8.

The laser phase and cathode position in parameter combination C and D are both adjusted from parameter combination B for optimizing the beam transport of TELBE and CBS. The reason of the adjustment will be presented in detail in Section 2.8.4 and 2.8.5.

Table 2.1 Optimized operation status of the ELBE SRF gun.

parameter	A	B	C	D
gradient	7.5 MV/m			
bunch charge	200 pC			
DC voltage	5 keV			
laser spot diameter	4 mm			
rms laser pulse length	7 ps			
laser phase	15°	20°	20°	20°
cathode position	2.8 mm	1.2 mm	1.7 mm	1.8 mm

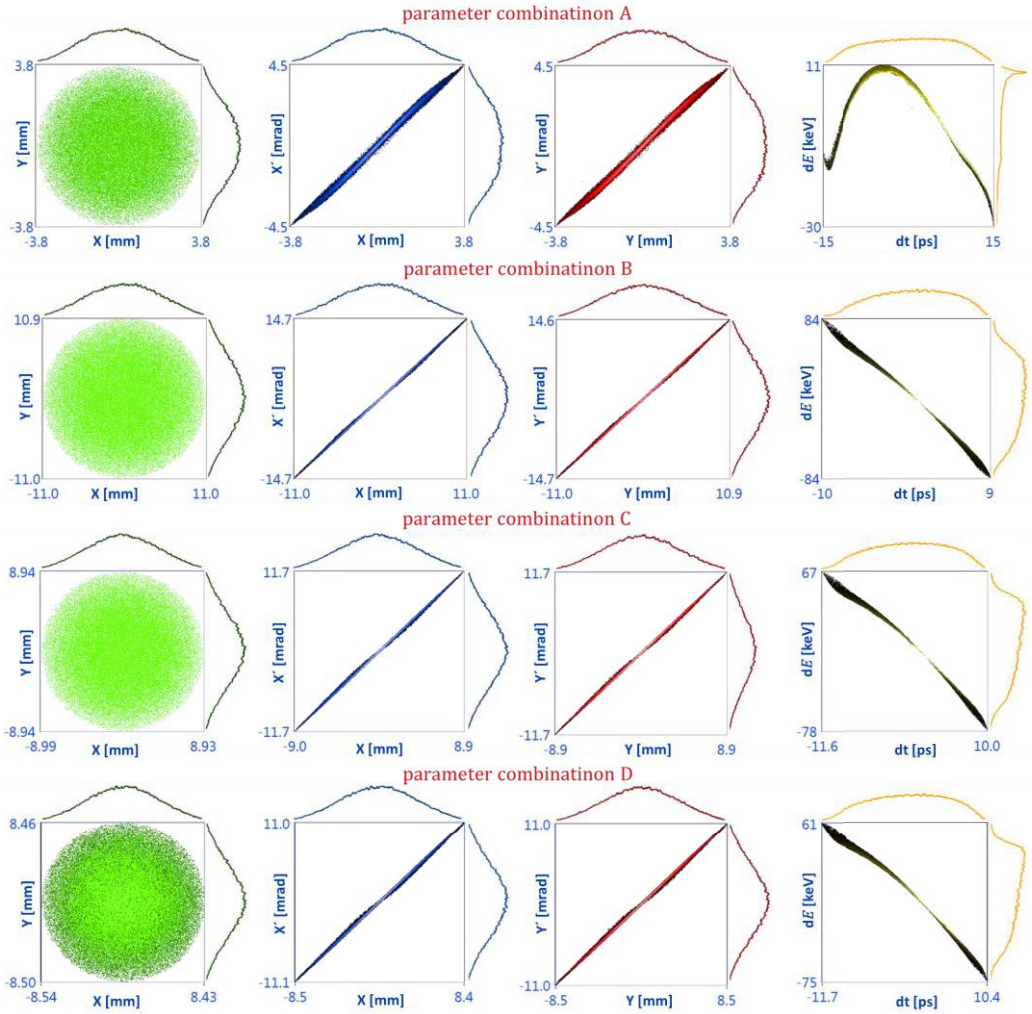

Fig. 2.25 Phase spaces for the four chosen parameter combinations.

Table 2.2 Beam quality parameters for the four chosen parameter combinations.

parameter	A	B	C	D
$\bar{E}$[MeV]	4.20	4.03	4.10	4.11
σ_t [ps]	7.12	4.15	4.82	4.97
σ_E [keV]	8.6	35.1	30.6	29.3
σ_u[mm]	1.48	4.41	3.50	3.30
$\sigma_{u'}$[mrad]	1.83	5.84	4.56	4.28
ε_u [μm]	1.48	4.02	2.89	2.75
k_l [keV/ps]	-1.75	-15.0	-13.0	-12.3
DoN [keV]	6.18	2.37	3.27	3.47

2.8. Optimization of beam transport

2.8.1. Longitudinal transport strategies

The evaluation of the distribution in LPS is important for an optimal beam transport. Section 2.5.1 has shown that chromatic effects strongly affect the bunch distribution in TPS. The bunch length also plays an important role in all space-charge-related effects, including CSR, LSC, wake effect and so on. Furthermore, the nonlinearity of the distribution in LPS determines the minimum possible bunch length of bunch compression.

In this section, two strategies for longitudinal transport are introduced based on the specific setting of ELBE. One is to generate a quasi-linear distribution in LPS for better bunch compression. The other is to utilize the LSC effect to compensate energy spread, which is important for beams to be bent or strongly focused in further transport. As discussed in Section 1.3, pELBE and nELBE do not demand strong bunch compression. Therefore, these two strategies will be explained only with respect to TELBE and CBS. The essential beamline components for the longitudinal beam transport are shown in Fig. 2.26. The SRF gun is connected to the ELBE accelerator via a dogleg which is composed of two edge focusing dipoles and a quadrupole triplet. In the accelerator after the dogleg, the following components are arranged sequentially: Linac 1, Chicane1, Linac 2 and Chicane 2. Each linac contains two 9-cell TESLA cavities. The THz radiation station is located directly after Chicane 2 and it is followed by a 47 m long transport line to the CBS station.

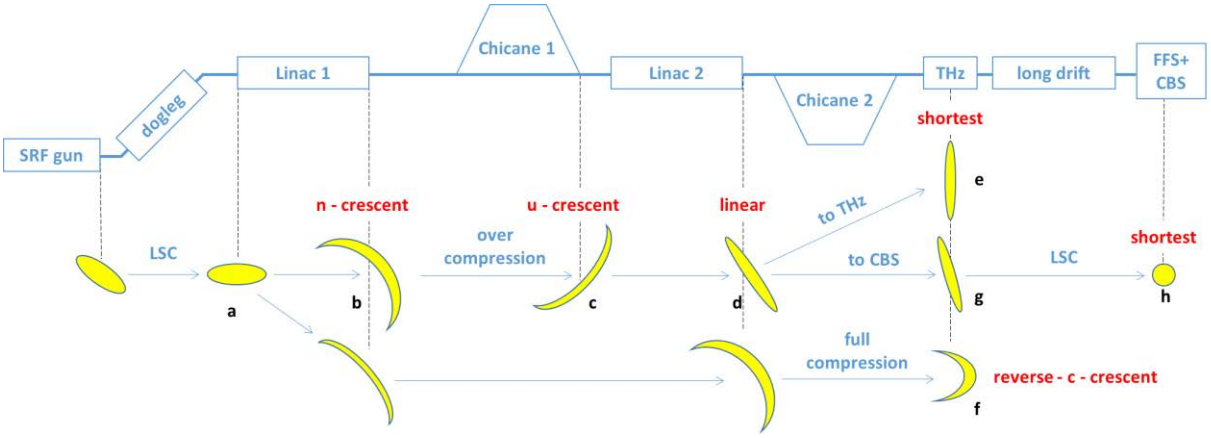

Fig. 2.26 Longitudinal beam transport strategies for THz and CBS stations.

The cavities, operating at 1.3 GHz, introduce nonlinear energy chirps to the bunch at any practical accelerating phase. In the following, the nonlinear chirped longitudinal phase space is referred to as an “n-crescent” or a “u-crescent”, depending on its direction, as shown in Fig. 2.26b and Fig. 2.26c respectively. The nonlinearity will maintain if the bunch is compressed

via chicanes from an n-crescent, generating a “reverse-c-crescent” (Fig. 2.26f) in which the correlated energy spread is transformed to the spread of time, limiting the minimum possible bunch length. The reverse-c-crescent can potentially be compressed even shorter if the nonlinearity is reduced. One technology is to use an extra cavity in the deaccelerating phase introducing an opposite nonlinear chirp. This cavity must provide the same degree of nonlinearity but smaller change of energy than the accelerating cavity does, and hence must be operating at higher frequency. A practical application is described in Reference [75] using a 3.9 GHz cavity to compensate the nonlinearity from a 1.3 GHz cavity.

As ELBE does not include such a high-frequency cavity, another scheme to alleviate the nonlinearity is to over-compress the bunch with the first chicane, and thus an “n-crescent” from the first linac will be converted into a “u-crescent”, shown in Fig. 2.26c. Consequently the nonlinear chirp from the second linac will be added onto the u-crescent and a linear energy chirp can be achieved as shown in Fig. 2.26d.

Based on the linear energy chirp, bunches are compressed to the possible minimum length by the second chicane (Fig. 2.26e) for the THz experiments. For CBS the compression should not be complete. Instead, a negative energy chirp (Fig. 2.26g) is required to compensate the LSC effect in the following beamline. The goal is to minimize the energy spread in front of FFS, as illustrated by Fig. 2.26h. The influence of LSC in drift spaces on energy spread has been experimentally verified at Photo Injector Test Facility at DESY, Location Zeuthen (PITZ), presented in Section 4.3.

Although pELBE and nELBE do not require bunches to be very short, dipoles are used in their beamlines. If the dispersed beam becomes too large and hits the beam pipe after dipoles, off-crest accelerations with negative chirps can be applied to reduce the energy spread at dipoles.

The discussed longitudinal transport strategies are studied numerically in simulations. An example of a 500 pC bunch transported in ELBE is presented in Fig. 2.27. The indexes of phase space diagrams in lower case letters correspond to the same positions in Fig. 2.26.

Fig. 2.27a shows the particle distribution in LPS before Linac 1, where energy spread is minimized by a negative chirp from the gun-cavity, Additionally, the bunch is always longitudinally compressed before Linac 1 to reduce nonlinear energy chirp in the following cavities. In the next step, Linac 1 chirps the bunch negatively and generates the inevitable n-crescent with DoN of 20 keV, as shown in Fig. 2.27b. After that, Chicane 1 over-compresses the bunch, converting its shape into u-crescent with the DoN of 42 keV (Fig. 2.27c). This u-

crescent is then injected into Linac 2 and its DoN is alleviated to 14 keV, generating a quasi-linear bunch (Fig. 2.27d). With the reduced nonlinearity, the bunch is longitudinally compressed to the minimum possible length of 0.30 ps FWHM, as shown in Fig. 2.27e where the reduced nonlinearity still forms the head and tail in LPS, enlarging the bunch length. Here the bunch length is optimized and expressed with FWHM values because the FWHM bunch length is more important than rms bunch length for THz.

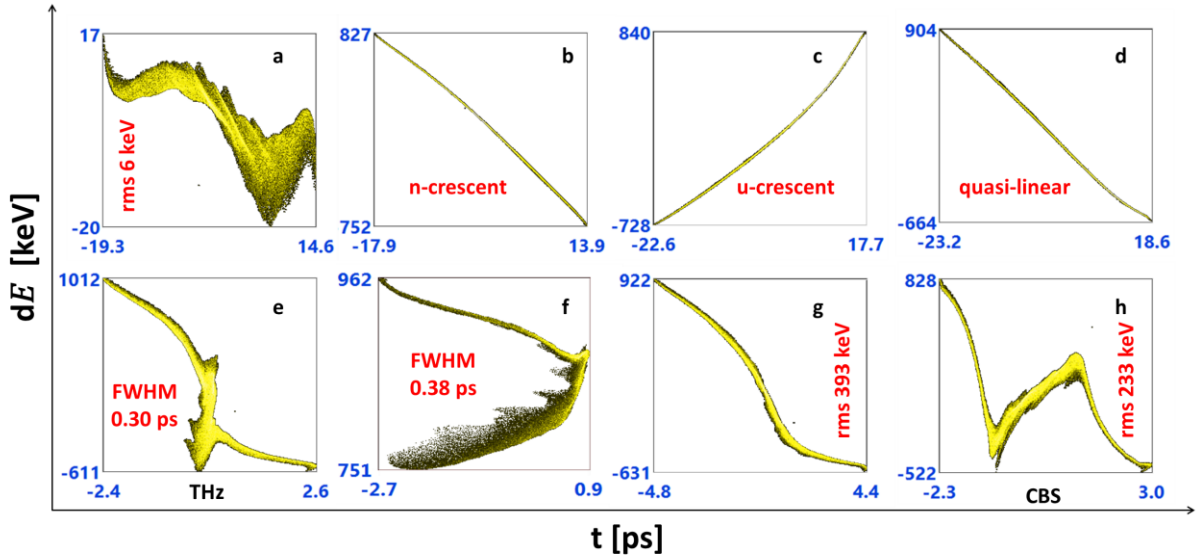

Fig. 2.27 Longitudinal phase spaces at each of the following positions: (a) before Linac 1; (b) after Linac 1, the n-crescent appears; (c) after Chicane 1, the bunch is over-compressed to obtain the u-crescent; (d) after Linac 2, quasi-linear chirp is achieved; (e) at the THz station, the bunch is compressed to a minimum FWHM bunch length of 0.30 ps; (f) after Chicane 2 for the case of compressing the bunch without alleviating the n-crescent; (g) after Chicane 2 with a proper quasi-linear negative chirp for CBS experiments; (h) at the CBS station, after 47 m of drifting, the influence of LSC is compensated by the negative energy chirp.

For comparison, the bunch in Fig. 2.27a is also transported according to the bottom procedure line in Fig. 2.26, where both linacs provide n-crescents and the first chicane is not used. In this case the output bunch from Linac 2 has similar energy (about 24.5 MeV) and energy spread (about 400 keV) to the quasi-linear bunch in Fig. 2.26d/Fig. 2.27d, but its DoN is enlarged by both linacs to 36 keV. Such a bunch can be compressed to the minimum possible length of only 0.38 ps FWHM. Furthermore, the FWHM bunch length cannot fully represent the longitudinal quality of an electron bunch. Fig. 2.28 shows that the compression based on the quasi-linear chirp results in a better longitudinal bunch profile with a higher peak and a lower tail.

When the quasi-linear bunch shall be transported to the CBS station where a smaller energy spread is desired, the bunch will be negatively chirped in Chicane 2 as shown in Fig. 2.27g.

The energy spread can be further compensated by the LSC effect during drift space and the compensated bunch distribution in LPS in front of the FFS is shown in Fig. 2.27h. If the alleviation of nonlinearity is not applied (Fig. 2.27f), it is not possible to compensate the energy spread utilizing the LSC effect.

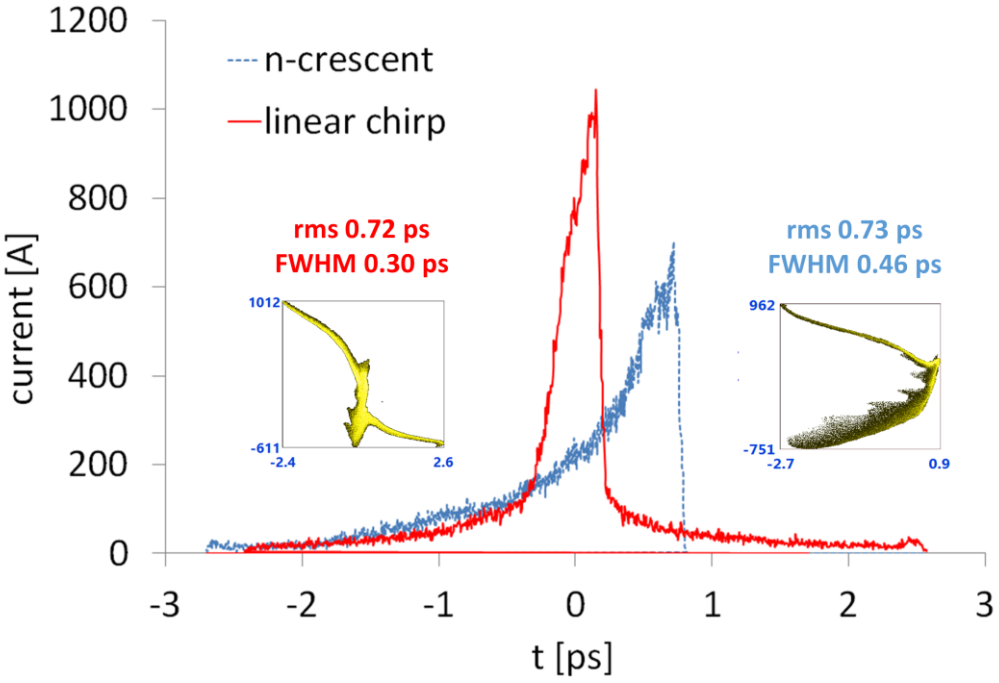

Fig. 2.28 Longitudinal profile of the compressed bunch based on the n-crescent or the linear chirp.

For bunch charges lower than 200 pC, small laser phases result in bunches short enough that the nonlinear chirp from Linacs are negligible. In this case, another effect should be considered that the dogleg generates a u-crescent. The mechanism will be discussed case wise in Section 2.8.4.

2.8.2. Optimization for pELBE

In this section, the beam optimization for pELBE is presented. According to Section 2.7, parameter combination A in Table 2.1 is chosen for pELBE. Beam size and emittance are displayed along the beamline in Fig. 2.29. The energy gain of the four cavities sequentially along the beamline is set to the possible maximum of 12 MeV, 9 MeV, 7 MeV and 7 MeV.

The beam is focused before entering the dogleg (beam line is shown in Fig. 2.17) and diverted at the exit of the dogleg. The two solenoids between the dogleg and Linac 1 are fabricated for beams from the thermionic gun at ELBE, the kinetic energy of which is only 250keV. For the SRF gun these two solenoids do not have obvious effects and they are not used in simulation, although shown in Fig. 2.29.

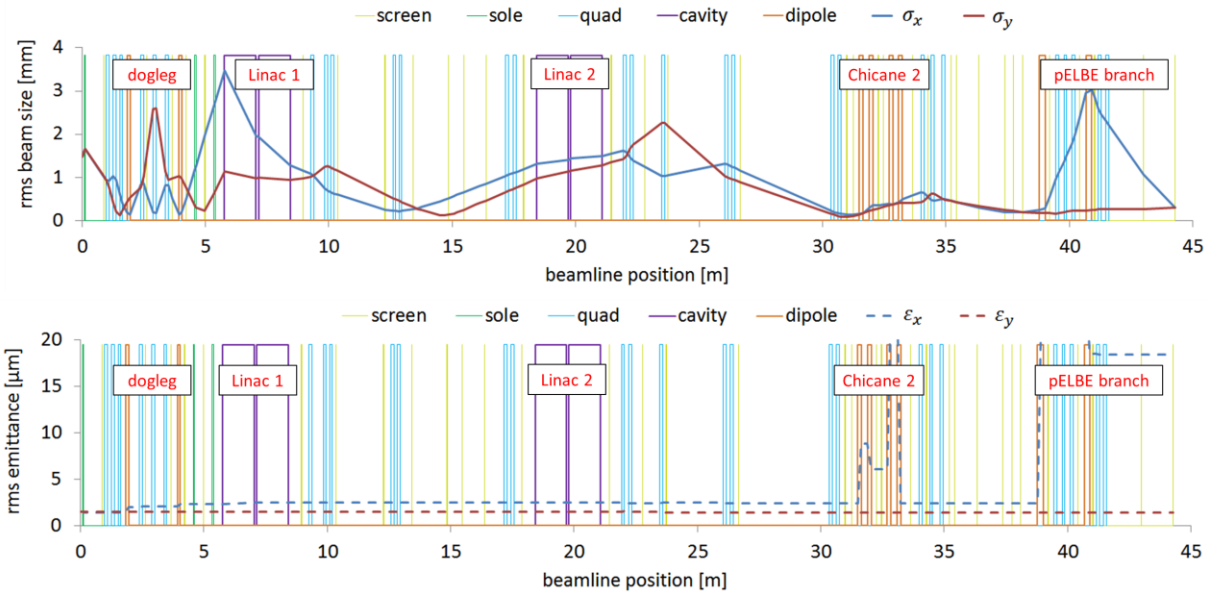

Fig. 2.29 Beam size profile (top) and emittance profile (bottom) of pELBE beam transport using parameter combination A.

The beam size becomes the largest at the entrance of Linac 1, as shown in Fig. 2.30. Linac 1 focuses the beam while accelerating it, therefore the output beam is transversely smaller. From there on, the simplex optimization presented in Section 2.5.5 is applied to control transverse beam size and emittance.

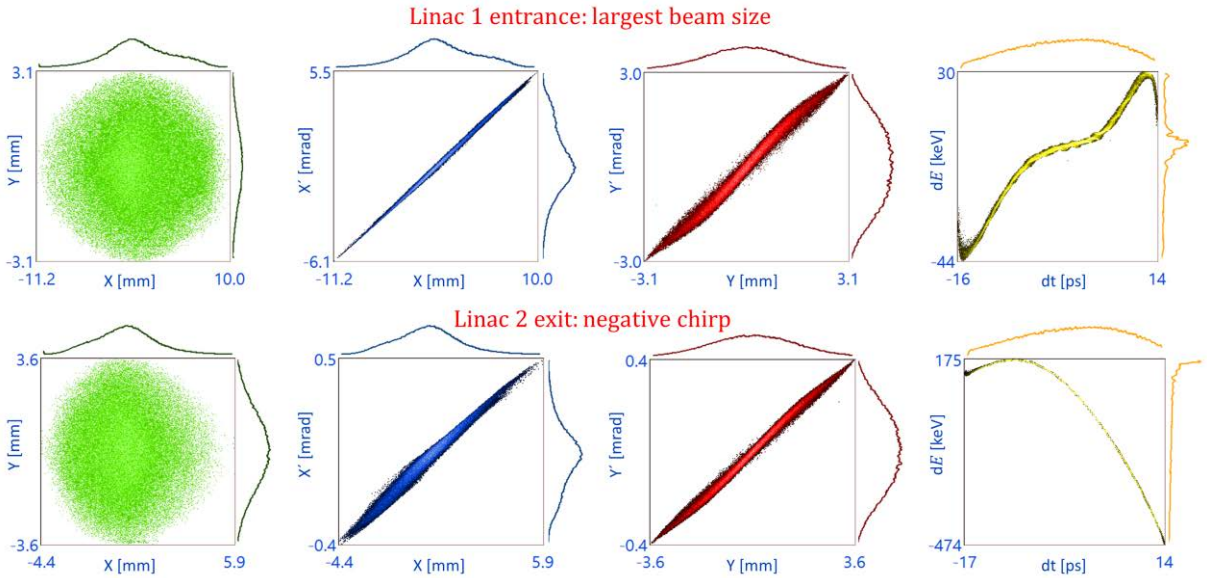

Fig. 2.30 Phase space at important positions of 200 pC beam transport for ELBE. The first row shows the largest beam size at the entrance of Linac 1 where the overall beam size reaches 21.2 mm but still smaller than the inner diameter of the beam pipe, which is 38 mm. The second row shows the chirped bunch at the exit of Linac 2, with an overall bunch length of 31 ps and an rms energy spread of 182 keV.

As longitudinal parameters are scarified by applying parameter combination A, the overall length of the electron bunch (31 ps) is longer than the requirement of pELBE (20 ps) in Table 1.1. To compress the bunch, Linac 2 chirps the beam negatively, generating an energy spread of 182 keV as shown in Fig. 2.30.

Based on the chirp, Chicane 2 compresses the bunch slightly to an overall bunch length of 29 ps instead of the desired 20 ps, because of a stronger compression observed in simulation in the final beamline branch of pELBE. This phenomenon is shown and explained in Fig. 2.31: At the entrance of the first dipole the input bunch is negatively chirped (Fig. 2.31a), which is then dispersed horizontally by the first dipole (Fig. 2.31b). Observed along the travel direction of the bunch, low-energy electrons travel on the right and high-energy electrons on the left. The dispersed beam is focused by quadrupoles but it is not crossed horizontally and the beam size increases (Fig. 2.31c). Such a bunch enters the second dipole with those low-energy particles in the front of the bunch, travelling on the right side and passing through the second dipole along a longer trajectory than those high-energy particles at the rear left of the bunch. Therefore, the entire bunch is compressed by the second dipole.

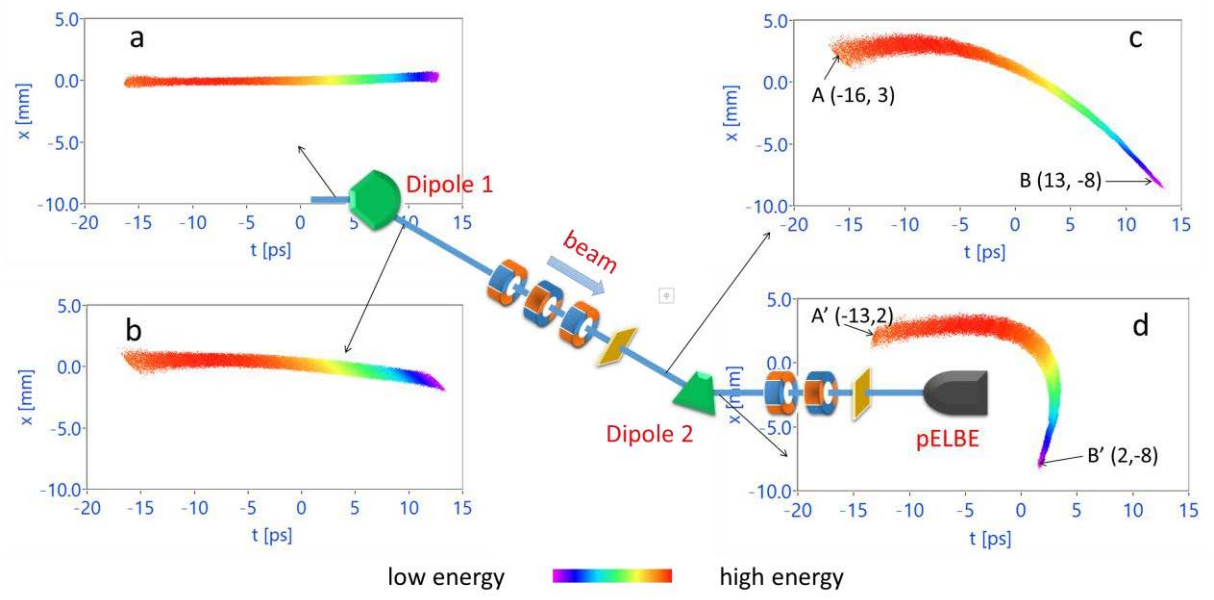

Fig. 2.31 beam compression by the pELBE branch. (a) shows the input bunch from the main beamline of ELBE, with a negative chirp. (b) shows that the beam is dispersed with low-energy/high-energy particles bent more/less and traveling on the right/left side, if observed along the travel direction. (c) shows the input bunch of the second dipole whose entrance angle and exit angle are both zero. (d) is the output bunch of the second dipole, where low-energy/high-energy particles travel a longer/shorter path and therefore the bunch is compressed.

To illustrate this phenomenon quantitatively, two points A (-16 ps, 3 mm) and B (13 ps, -8 mm) are chosen from Fig. 2.31c which are then transported to A' (-13 ps, 2 mm) and B'

(2 ps, -8 mm) in Fig. 2.31d. The temporal interval between them are 29 ps before the second dipole and 15 ps afterwards, i. e., the temporal length compressed by the dipole is about 14 ps.

The sector angle of the second dipole is 22.5°. The entrance and exit angles are both about 0°. In this case, the difference between two trajectories can be calculated simply as $[3\text{ mm}-(-8\text{ mm})]\times 22.5°=4.32\text{ mm}$, where 3 mm and -8 mm are the transverse coordinates of the two points entering the second dipole and 22.5° is the sector angle of the second dipole. For the quasi-relativistic beam here with an energy of 36.8 MeV, this path length difference corresponds to a temporal difference of 14.3 ps, which is consistent with the value observed in simulation (14 ps).

To achieve the above bunch compression in the pELBE beamline branch, a key operation is to avoid crossing the beam horizontally when focusing it after the first dipole, as well as to obtain a large transverse size to generate enough path length difference in the dipole. A relatively large size at the second dipole has another advantage that the beam will be strongly focused in the remaining two quadrupoles after the second dipole, to achieve the desired phase space on the beryllium window before pELBE target.

The final bunch distribution in phase space at the beryllium window is shown in Fig. 2.32. The beam parameters at the pELBE station are listed in Table 2.3 satisfying all requirements of pELBE as introduced in Section 1.3.1. With an energy of 38.8 MeV, the rms scattered angle is 23.2 mrad according to Equation (1-1). The intercepts of the acceptance on position axis and divergence axis are 1.75 mm and 12.5 mrad respectively, calculated with Equation (1-2). The acceptance area is also drawn in Fig. 2.32, covering all electrons transported to pELBE.

To conclude, using parameter combination A of ELBE SRF gun and maximum possible gradients of all cavities, the transverse requirements of beam transport to pELBE can be satisfied by automatic optimization functions of the simulation tool introduced in Section 2.5.5 and 2.6. Longitudinally the bunch has to be compressed to satisfy the requirement of "20 ps of overall bunch length". The compression from the second dipole in the pELBE branch is applied, with the mechanism explained. Parameters used in this simulation can be found in Appendix II.

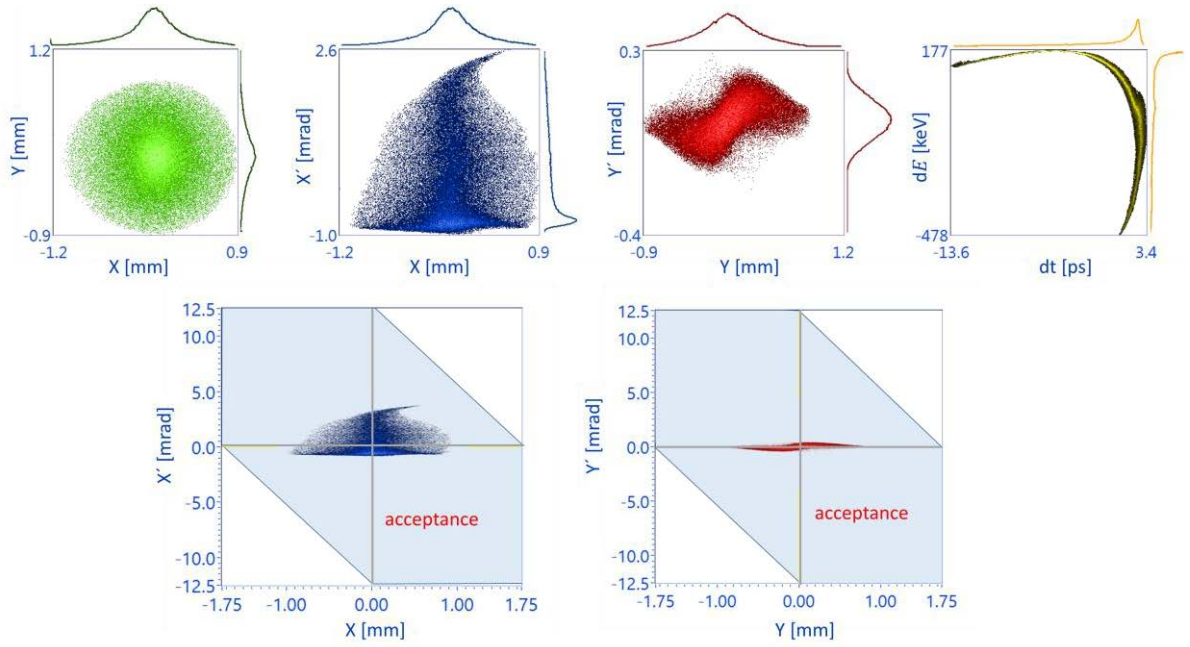

Fig. 2.32 The optimized phase space at the beryllium window of pELBE. Horizontal and vertical phase spaces satisfy the requirements of geometrical settings of pELBE. In the second row, transverse phase spaces are the same as those in the first row but with different scales to partly cover the boundary of the acceptance area.

Table 2.3 Parameters of 200 pC bunch transported to pELBE beryllium window.

$\bar{E}$ [MeV]	38.8	σ_t [ps]	3.7
σ_E [keV]	163	t_{FWHM} [ps]	0.74
σ_x [mm]	0.30	σ_y [mm]	0.3
x_{FWHM} [mm]	0.40	y_{FWHM} [mm]	0.49
$\sigma_{x'}$ [mrad]	0.82	σ_y' [mrad]	0.073
ε_x [μm]	18.4	ε_y [μm]	1.42

2.8.3. Optimization for nELBE

This section presents the beam transport optimization for neutron production at nELBE. The parameter combination A of ELBE SRF gun (Table 2.1) has also been used here with the focus on transverse beam quality. Beam size and emittance profiles of the optimized beam transport for nELBE are shown in Fig. 2.33 The beam transport up to Linac 2 is the same with that for pELBE. After Linac 2, Chicane 2 compresses the bunches from an overall bunch length of 29 ps to 20 ps to satisfy the longitudinal requirements in Table 1.1. Then the beam enters the beamline branch of nELBE which starts with a vertical dipole bending the beam for 4°. Next, a second dipole bends the beam horizontally for -22.5° and vertically for -4°. The

last dipole bends the beam horizontally for 32.5° towards the beryllium window before nELBE target.

The requirements on TPS are challenging for beam transport inside the nELBE branch. As described in Section 1.3.2, for an energy lower than 34.2 MeV, the acceptance area vanishes. With the highest possible gradients of all cavities at ELBE, this simulation yields a final energy of 38.8 MeV in this simulation. Now the smaller scattering angle results in a narrow acceptance area as shown in Fig. 2.34. Strong focusing is required at the last pair of quadrupoles to focus most particles into the acceptance area, which is achieved by increasing transverse size of the input beam for these two quadrupoles.

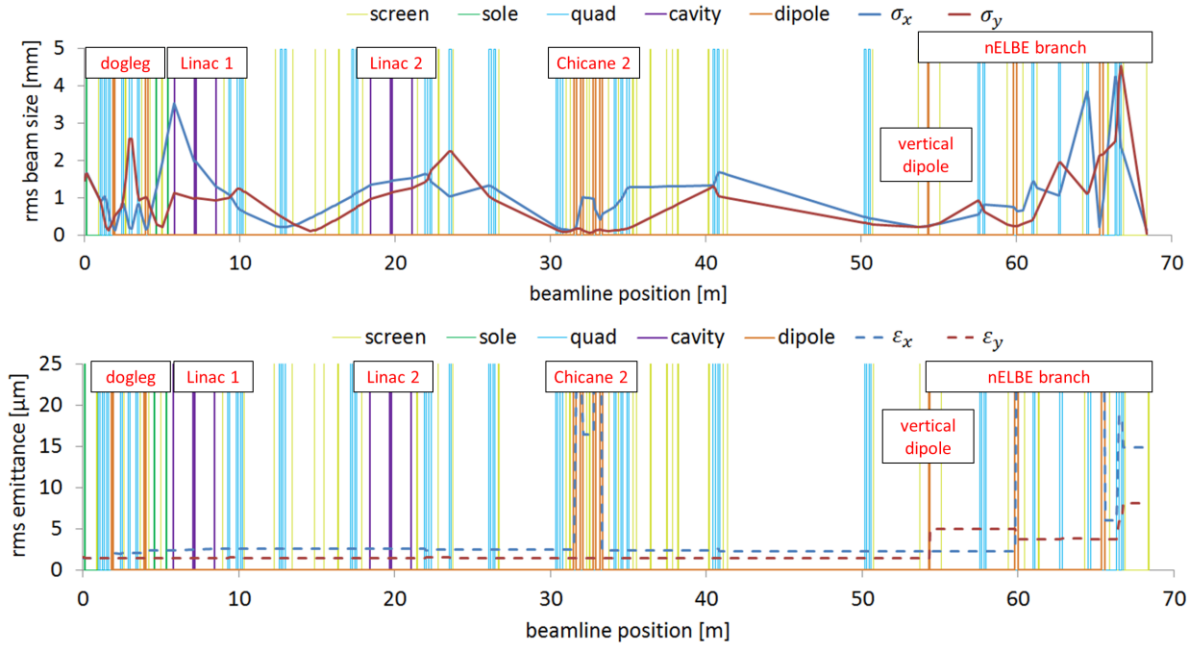

Fig. 2.33 Beam size profile (top) and emittance profile (bottom) of nELBE beam transport (200 pC) using parameter combination A in Table 2.1.

Meanwhile, generating small beams before the dipoles helps to control emittance growth so that the narrow acceptance covers the majority of electrons. As a result, bunch compression from path length difference in dipoles (Section 2.8.2) is negligible, and hence the bunch should be compressed in chicanes to achieve the required overall length of 20 ps. For the 4-magnet D-shape chicane at ELBE, the difference of bunch length before and after the chicane can be calculated by:

$$t_c = \frac{2\theta_c^{\,2}}{c}\frac{\sigma_E}{\bar{E}}\left(l_{dri} + \frac{2}{3}l_{dip}\right) \tag{2-16}$$

where θ_c is the bending angle in dipoles, c is the speed of light, l_{dri} is the distance between the first two dipoles and l_{dip} is the width of dipoles. Equation (2-16) shows that for the same compression strength, a larger bending angle reduces the needed energy spread. Thus the bunch can be chirped by a preceding cavity at a phase corresponding to larger acceleration. In this simulation, Chicane 2 is set to its maximum bending angle of 30° to maximize the final energy.

The transverse beam quality is optimized with large values of the weighting factor of emittance W_{emi} at the end of Chicane 2 and at the last dipole of nELBE branch, as shown in Fig. 2.34. The last two quadrupoles are adjusted manually to match the bunch to the acceptance area. However, for the current setting it is not possible for all electrons. Parameters of the final bunch on the beryllium window are presented in Table 2.4.

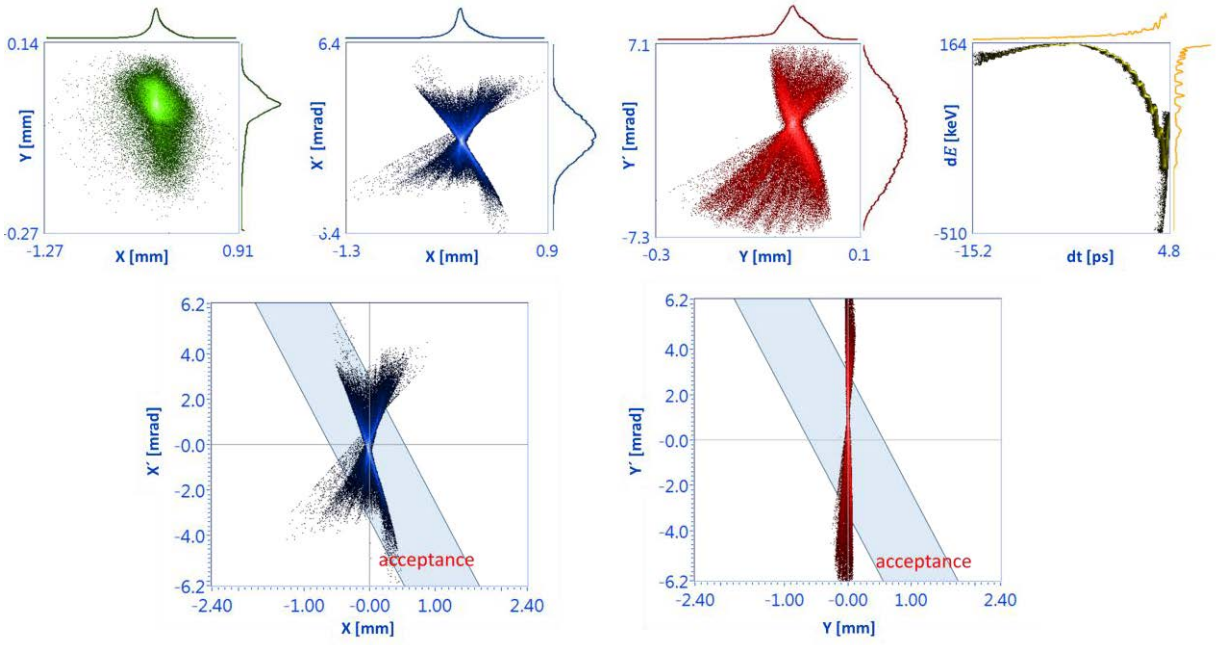

Fig. 2.34 The optimized phase space at the beryllium window of nELBE. 60% of particles satisfy the requirements of geometrical settings of nELBE. In the second row, transverse phase spaces are the same as those in the first row but with different scales to partly cover the boundary of the acceptance area.

Table 2.4 Parameters of 200 pC bunch transported to nELBE beryllium window.

$\bar{E}$ [MeV]	38.8	σ_t [ps]	4.6
σ_E [keV]	142	t_{FWHM} [ps]	1.59
σ_x [mm]	0.13	σ_y [mm]	0.04
x_{FWHM} [mm]	0.12	y_{FWHM} [mm]	0.05
$\sigma_{x'}$ [mrad]	1.39	$\sigma_{y'}$ [mrad]	2.75

ε_x [μm]	14.2	ε_y [μm]	8.25

To sum it up, the acceptance area at the nELBE beryllium window can be very small or even vanish, depending on the energy of the beam. In the presented simulation, bunch compression in Chicane 2 is far from full compression, therefore the transverse emittance can be maintained after it (Fig. 2.34.). In the beamline branch of nELBE, the emittance is controlled but not optimized, as the main target of beam transport is to match a specific distribution rather than the value of emittance. By manually tuning the final quadrupoles, about 60% of 200pC electrons are transported into the critical acceptance. Parameters used in this simulation can be found in Appendix II.

2.8.4. Optimization for TELBE

This section presents and compares beam transport simulations of different parameter combinations for ELBE SRF Gun given in Table 2.1. For the TELBE beamline, the main objective is to obtain a short electron bunch at the THz radiator (silicon mirror). To verify the choice of parameter combination B, the simulation starts with the parameter combination A. In this case the SRF gun generates a long bunch (rms 7.1 ps). Based on the beam transport for nELBE up to Linac 2, full compression with the compressed bunch length of 1.32 ps is provided by Chicane 2, as shown in Fig. 2.35 and marked with "long bunch & nonlinear". With the long bunch and its nonlinearity, the shortest possible bunch has the reverse-c-crescent shape in LPS. Chicane 2 is set to its maximum bending angle, therefore the energy at the silicon mirror is the maximum possible of 37.5 MeV.

Still using the parameter combination A, the DoN of the bunch before compression can be alleviated from 59 keV (for "long bunch & nonlinear") to 22 keV applying the longitudinal transport strategy described in Section 2.8.1. Such a bunch is compressed by Chicane 2 to the rms bunch length of 1.2 ps with more particles in the center of the bunch, as shown in Fig. 2.35 and marked with "long bunch & quasi-linear". In this case, Linac 1 also chirps the beam with an off-crest phase for the following over-compression in Chicane 1, and hence the energy of the bunch is reduced to 34.7 MeV.

Beam size and emittance profiles are shown in Fig. 2.36. In the first chicane, the beam size is large and the beam is bent up to 400 mm from the straight beam axis. But the vacuum chamber of the chicane has a much larger width of 520 mm. The horizontal emittance is minimized at the exit of Chicane 1 by automatically optimizing preceding quadrupoles. The

input beam has a bunch emittance of 2.78 µm, an horizontal average slice emittance of 1.36 µm and a horizontal overlap ratio of 0.42. The average slice emittance is increased in Chicane 1 to 1.60 µm, however the overlap ratio is reduced to 0.35, and as a result the emittance of the output bunch is even smaller, being 2.36 µm.

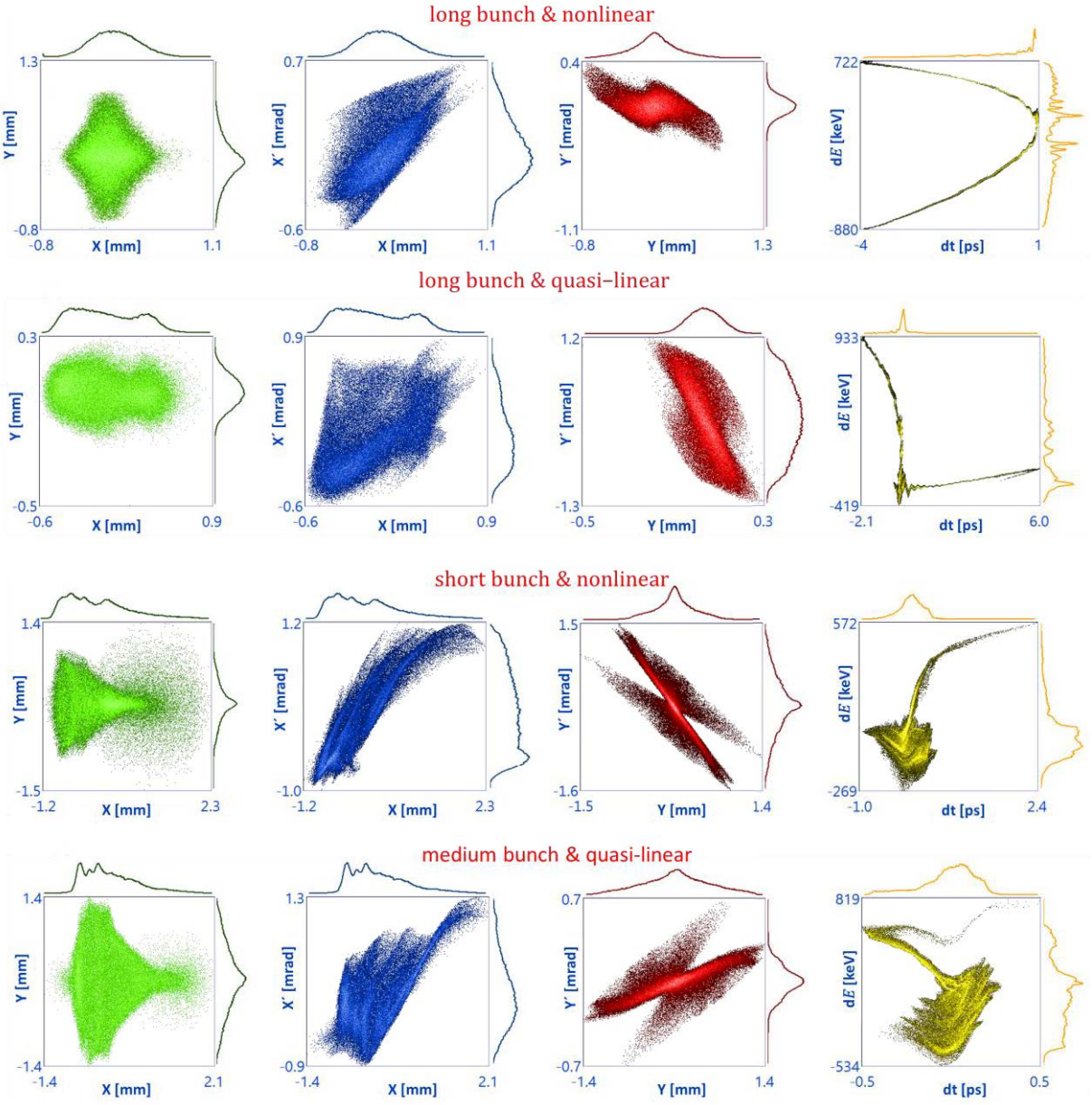

Fig. 2.35 Distributions in phase space at the silicon mirror of TELBE with different beam transport. "Long bunch", "short bunch" or “medium bunch” refers to the output electron bunch from ELBE SRF Gun with parameter combination A, B or C respectively. "Nonlinear" means that the bunch accelerated by cavities are compressed directly by chicanes nonlinearly in LPS; while "quasi-linear" means that longitudinal transport strategies have been applied and hence the non-linearity has been alleviated.

At the silicon mirror after Chicane 2, transverse beam size as well as bunch length is optimized to pass through the 4 mm diameter hole on it, where a small emittance is not a concern. A branch beamline after the THz experimental station serves for dumping the beam,

which starts with a 45° dipole. After the dipole, the dispersed beam size is usually very large. Consequently the beam pipe has a diameter of 100 mm. In this dumping beamline the only purpose of beam transport is to lower beam loss, where emittance is not of concern and reaches 500 µm after the dipole.

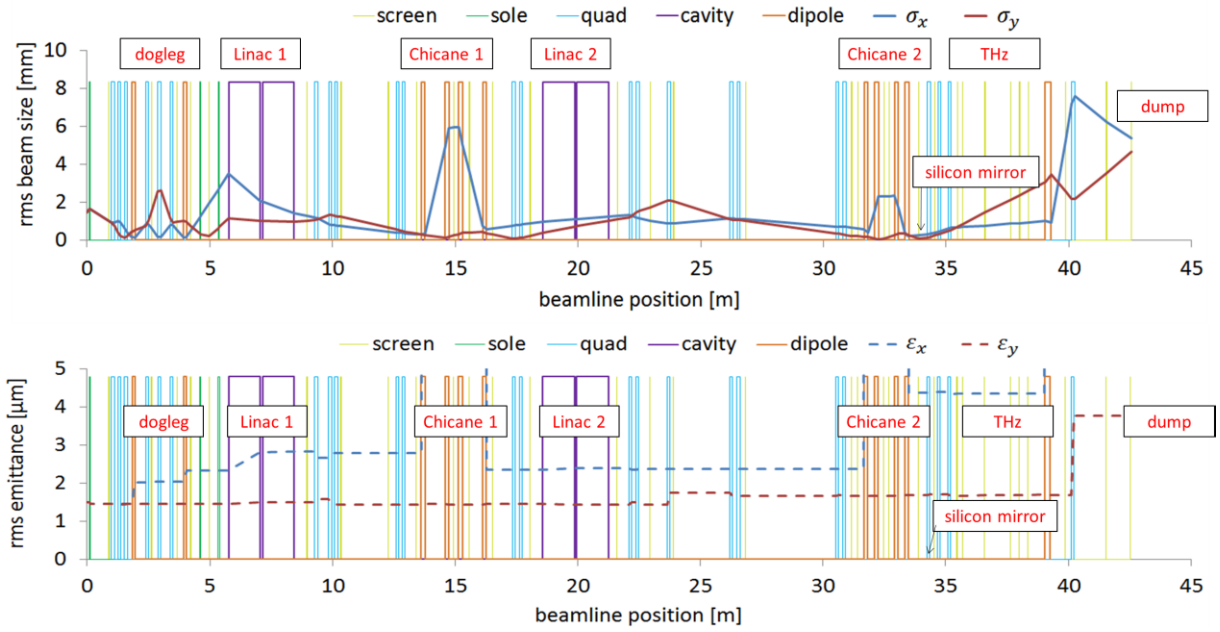

Fig. 2.36 Beam size and emittance profiles of beam transport for TELBE (200 pC), with parameter combination A and the longitudinal transport strategy applied to alleviate DoN in longitudinal phase space.

For the above beam transport based on the setting of "long bunch & quasi-linear", the distribution in LPS has a long leading part, which comes from the remaining DoN. For further reducing the DoN, parameter combination B of ELBE SRF gun is applied and the bunch produced by the gun is shorter.

With the shorter bunch, the LSC effect becomes stronger and the beamline between the gun and Linac 1 provides a u-crescent in LPS, as shown in Fig. 2.37: The output bunch of the SRF gun is negatively chirped and has a DoN of 2.4 keV. The LSC effect and the spontaneous compression due to velocity difference of particles together reduce the DoN to 1.5 keV at the entrance of the dogleg. The designed beam transport of the dogleg is illustrated in Fig. 2.37 where High-Energy Electrons (HEEs) and Low-Energy Electrons (LEEs) travel along longer trajectories compared to medium-energy electrons, and thus both HEEs and LEEs should move relatively to the tail of the bunch through the dogleg. However, HEEs travel faster, which compensates their movement to the tail, compared, those slower LEEs move even further to the tail. As a result, LEEs are longitudinally chirped more than HEEs, forming a density peak at the head of the bunch. The DoN here increased to 4.6 keV due to this complicated process. The density peak then leads to stronger LSC effect on LEEs such that

the energy gain at the head of the bunch is greater than the energy reduction at the tail, generating an obvious u-crescent with a DoN of 10.8 keV.

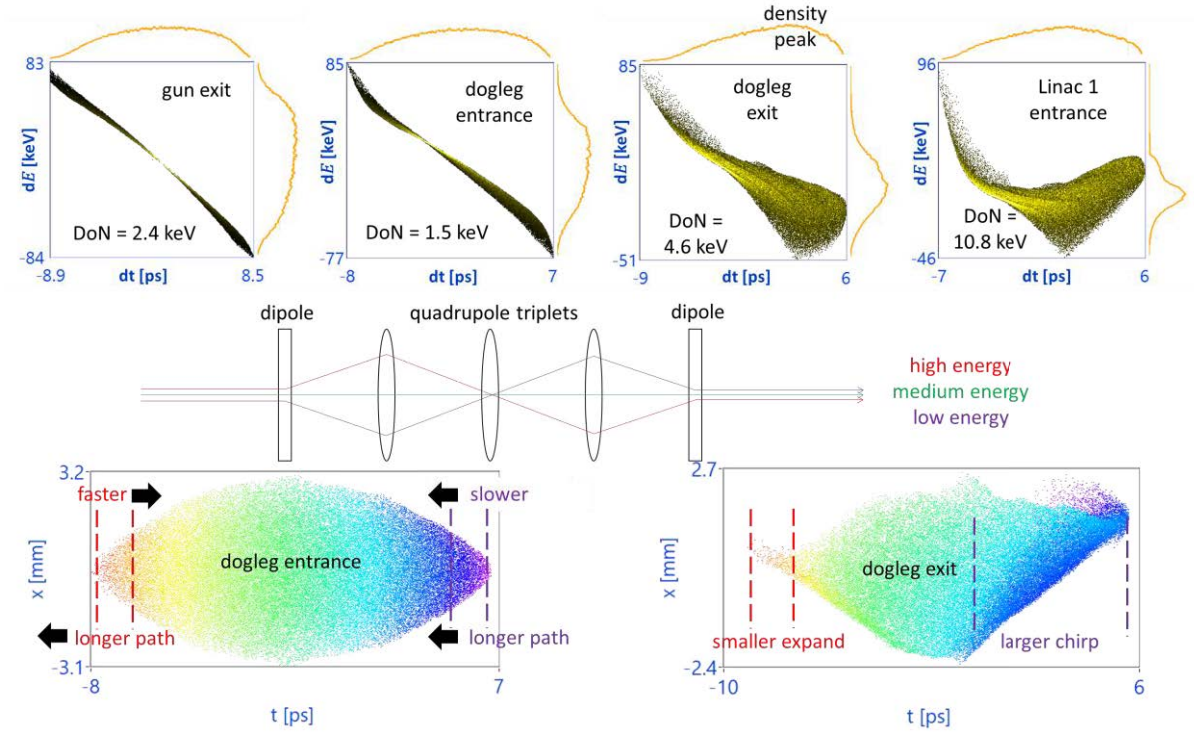

Fig. 2.37 The u-crescent generated in the dogleg for short, negatively chirped bunches applying the parameter combination B of the ELBE SRF gun.

The u-crescent can be alleviated by cavities which always provide n-crescents to the bunch. However, because of the small bunch length from parameter combination B, cavities are not efficient enough to remove the u-crescent. Consequently, the compressed bunch has a c-crescent shape in LPS, as shown in Fig. 2.35 and marked with "short bunch & nonlinear". The final energy of the bunch is 36.7 MeV, which is higher than the "long bunch & quasi-linear" case as Linac 1 is set to its peak phase. But the energy is lower than that of the "long bunch & nonlinear" case as the shorter bunch length requires stronger chirp in Linac 2 to achieve full compression. The rms bunch length of the compressed bunch is 0.34 ps, which is better compared to cases using parameter combination A, but the c-crescent can be further improved.

The last beam transport for TELBE is based on parameter combination C in Table 2.1. It is based on parameter combination B but the cathode position is increased from 1.2 mm to 1.7 mm, which provides bunches with medium length of 4.82 ps, as shown in Fig. 2.23. Longer bunches reduce the LSC effect, therefore the u-crescent from the dogleg can be weaker. Meanwhile, cavities also provide more nonlinearity to longer bunches. Consequently, the bunch becomes more linear, as shown in Fig. 2.35 and marked with "medium bunch & quasi-linear". In this case, the rms bunch length at the silicon mirror of TELBE is 0.12 ps, which is

the best among the above four simulation settings for TELBE. The final energy of the bunch is 35.8 MeV with the optimized bunch length. In this simulation, the limiting factor for the bunch length is no longer the nonlinearity in LPS, instead, it is the modulation due to the LSC effect. Fig. 2.35 also shows that in cases of long bunches, this modulation is negligible.

The complete beam size and emittance profile for this beam transport with the best bunch length is shown in Fig. 2.38. The transverse size of the bunch is optimized at the silicon mirror and optimized beam parameters are listed in Table 2.5. Because of the small bunch length at the silicon mirror, the LSC effect significantly increases the energy spread from 229 keV to 658 keV at the entrance of the TELBE beamline branch to the beam dump, as shown in Fig. 2.39. With such a large energy spread, the dispersed beam in the TELBE branch has the largest overall size of 65 mm at the last quadrupole, but it is still safe in the 100 mm wide beam pipe.

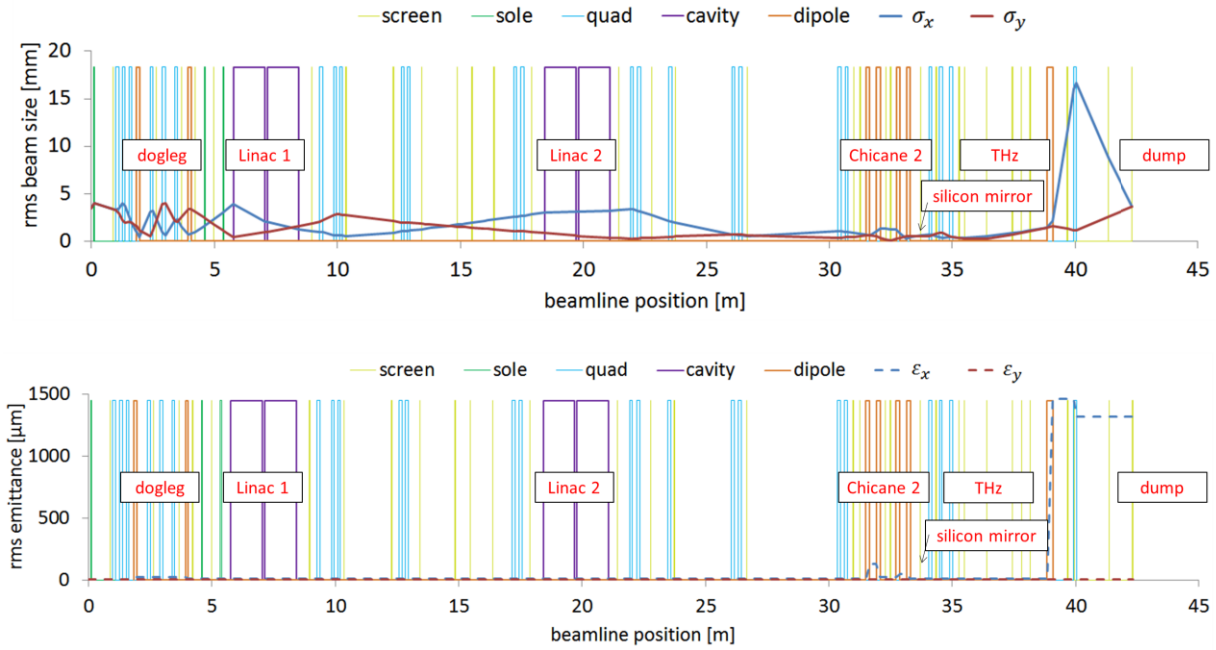

Fig. 2.38 Beam size and emittance profile for TELBE beam transport (200 pC), using parameter combination C of the ELBE SRF gun, generating the shortest bunch.

Table 2.5 Optimized parameters of 200 pC beam at the silicon mirror of TELBE.

$\bar{E}$ [MeV]	35.8	σ_t [ps]	0.12
σ_E [keV]	229	t_{FWHM} [ps]	0.24
σ_x [mm]	0.59	σ_y [mm]	0.53
x_{FWHM} [mm]	1.04	y_{FWHM} [mm]	1.04
$\sigma_{x'}$ [mrad]	0.42	$\sigma_{y'}$ [mrad]	0.10

ε_x [μm]	10.8	ε_y [μm]	3.52

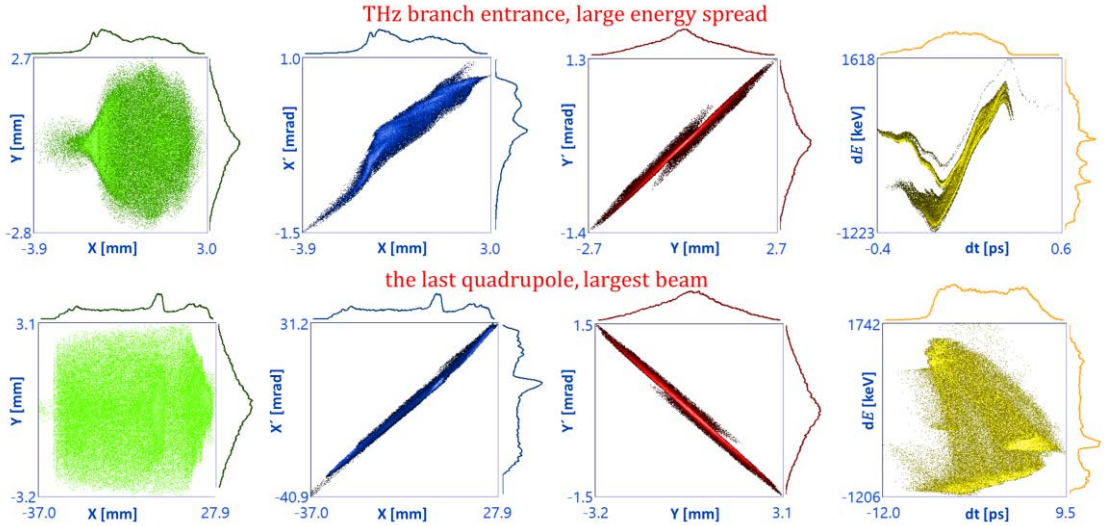

Fig. 2.39 The phase space at the entrance of TELBE beamline branch with large energy spread (top) and the largest beam in the branch (bottom). It is still safe in the 100 mm wide beam pipe of the TELBE branch.

To conclude, four groups of simulations have been made to gradually improve beam quality at TELBE: with long bunch (7.12 ps) and nonlinear LPS; long bunch and quasi-linear LPS; short bunch (4.15 ps) and nonlinear LPS; and medium bunch (4.82 ps) and quasi-linear LPS. For the two cases with the long bunch (parameter combination A), the nonlinearity in LPS dominates the compressed bunch length. The longitudinal transport strategy improves the bunch compression but to a very limited level. Bunch length in the case with short bunch (parameter combination B) is also limited by the nonlinearity in LPS - specifically by the u-crescent from the dogleg. The last case with medium bunch length (parameter combination C) alleviates most of nonlinearity in LPS and the bunch length is limited by the modulation of the bunch due to the LSC effect.

The rms bunch lengths for these four simulations are 1.34 ps, 1.2 ps, 0.34 ps and 0.12 ps respectively. One parameter is not sufficient to describe the longitudinal beam distribution. Additionally, it is completely presented in Fig. 2.40. The case of "long bunch & nonlinear" has the minimum FWHM bunch length but only 14% of electrons are in this range; the case of "long bunch & quasi-linear" has 44% of electrons in the FWHM bunch length of 0.15 ps; the case of "short bunch & nonlinear" includes 72% electrons in the FWHM bunch length but it has the lowest peak charge density. Compared to all other cases, the case of "medium bunch & quasi-linear" is the best, with the highest peak charge density as well as the highest average charge density. Parameters used in this simulation can be found in Appendix II.

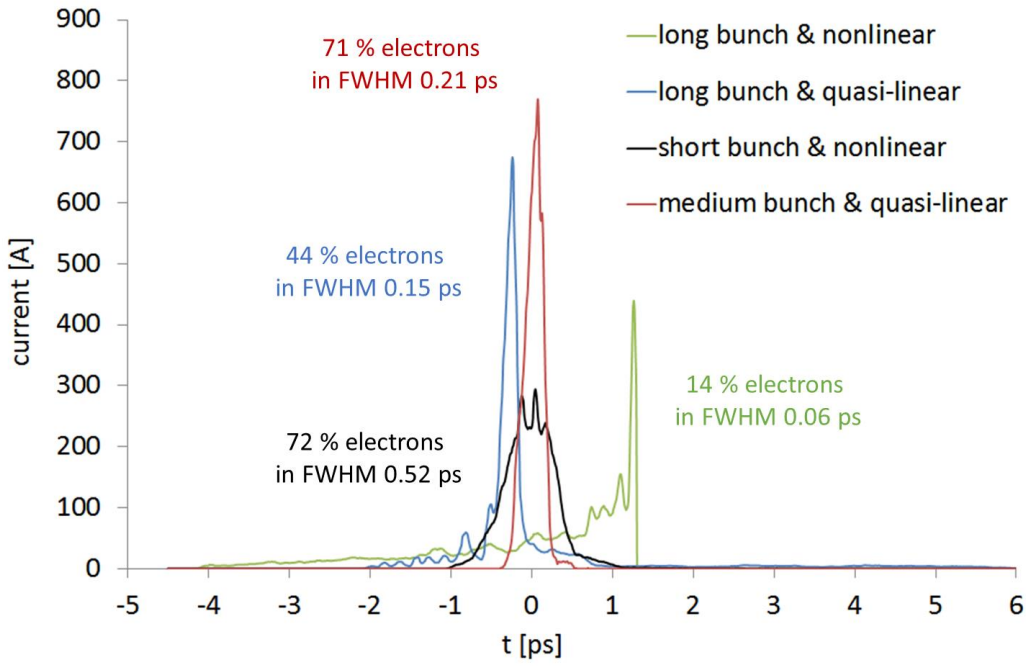

Fig. 2.40 Optimized longitudinal bunch distributions for TELBE beam transport.

2.8.5. Optimization for CBS

The final energy for CBS beam transport is required to be below 25 MeV. In this simulation, the final energy is set to 23 MeV which is the value from previous experiments [49], i. e., cavities cannot be set to their full gradients. Lower gradients lead to smaller cavity-induced nonlinearity for the bunch distribution in LPS, and hence the u-crescent generated in the dogleg cannot be completely cancelled if parameter combination C is used. Again, a longer bunch reducing the u-crescent from dogleg while increasing the n-crescent from cavities is desired. Therefore, parameter combination D with a cathode position of 1.8 mm is applied, generating a bunch that can be linearly distributed in LPS after Linac 2.

Beam size and emittance profiles are shown in Fig. 2.41 with zoom-in subfigures for the final focusing system. The beam size is optimized inside and at the end of the dogleg, staying below 4 mm up to Linac 1. The focusing effect of Linac 1 increases with gradient and the lowest gradient to maintain the beam size is 5.3 MeV for the two cavities of Linac 1. Usually Linac 1 is set to its peak phase and Linac 2 is used for chirping. A lower energy gain from Linac 1 means higher gradient of Linac 2, which leads to larger possible energy chirp and smaller bending angle of Chicane 2, benefiting the emittance.

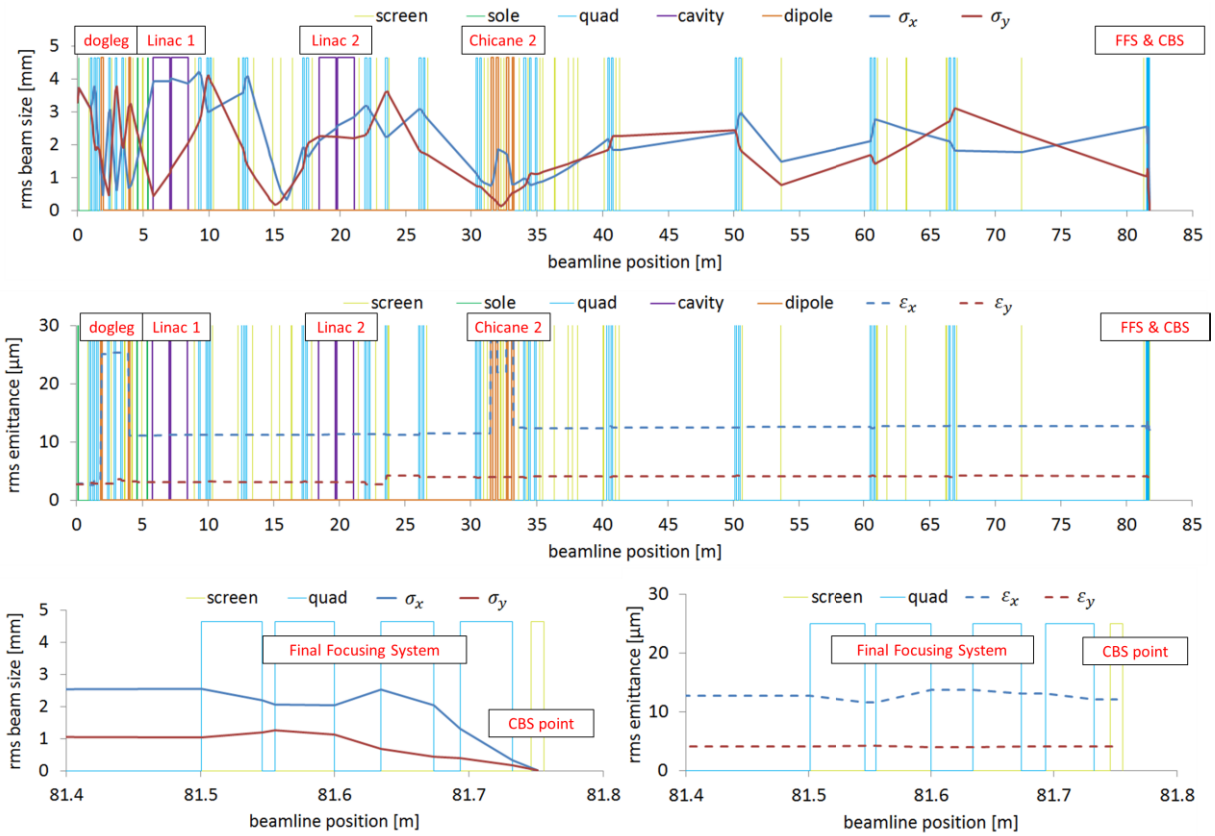

Fig. 2.41 Beam size and emittance profiles for CBS beam transport of a 200 pC beam.

To optimize Linac 2 and Chicane 2, a common gradient for the two cavities in Linac 2 and the bending angle of Chicane 2 are scanned. The accelerating phases are correctly set to keep a total energy of 23 MeV. The beam is transported to the entrance of FFS with bunch length and energy spread displayed in Fig. 2.42.

Between Linac 2 and FFS, the LSC effect dominates longitudinal beam quality. For a fixed setting of Linac 2, the bunch length at FFS first decreases with the bending angle of Chicane 2, while the LSC effect becomes stronger and thus the energy spread of the negatively chirped bunch becomes smaller. When the bunch length at FFS is small enough, strong LSC effect enlarges the energy spread quickly to its peak, with a positive energy chirp which expands the bunch longitudinally generating a peak of the bunch length after its minimum. Near this peak, the LSC effect becomes smaller and the energy spread is reduced again. Consequently, the longitudinal expansion of the bunch is also weaker and the bunch length at FSS is reduced to its second minimum value. After that, the chicane over-compresses the bunch and the bunch length increases as the LSC effect becomes weaker, reducing the energy spread to its original value.

In the energy spread vs. chicane angle diagram of Fig. 2.42, parameter points are marked by solid markers if the bunch length at FFS is below 1 ps, which is one of the requirements for

CBS in Table 1.3. Among these points, the one corresponding to the lowest energy spread is chosen for the beam transport for CBS, which is 5.5 MeV for the gradient of cavities in Linac 2 and 19° for the bending angle of Chicane 2.

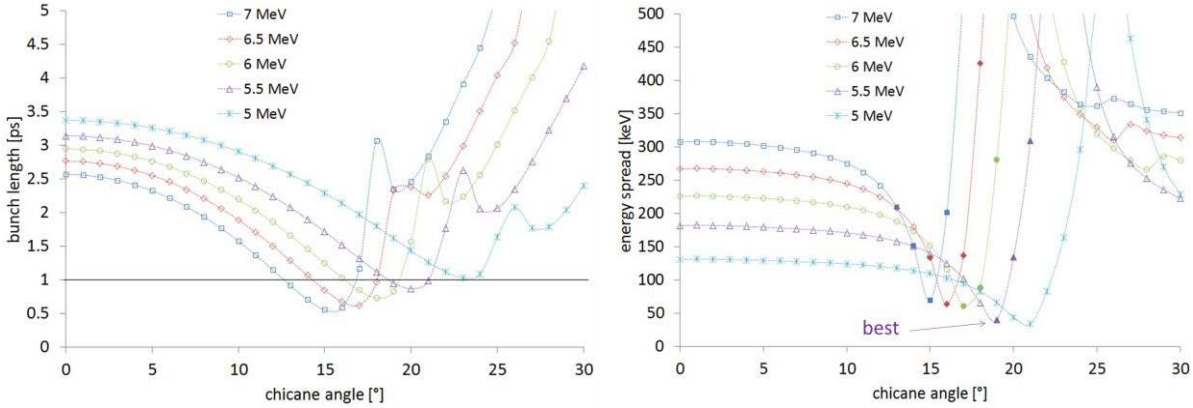

Fig. 2.42 Bunch length and energy spread at the entrance of FFS, with the gradient of Linac 2 and the bending angle of Chicane 1 scanned.

Bunch distributions in LPS at different positions are presented in Fig. 2.43. The u-crescent from the dogleg is alleviated by cavities. After Chicane 2, the bunch length is 4.0 ps and the energy spread is 221 keV (1%). Then in the long distance the bunch length is reduced by velocity compression to 0.96 ps, and the energy spread is compensated by the LSC effect to 33.7 keV (0.15%).

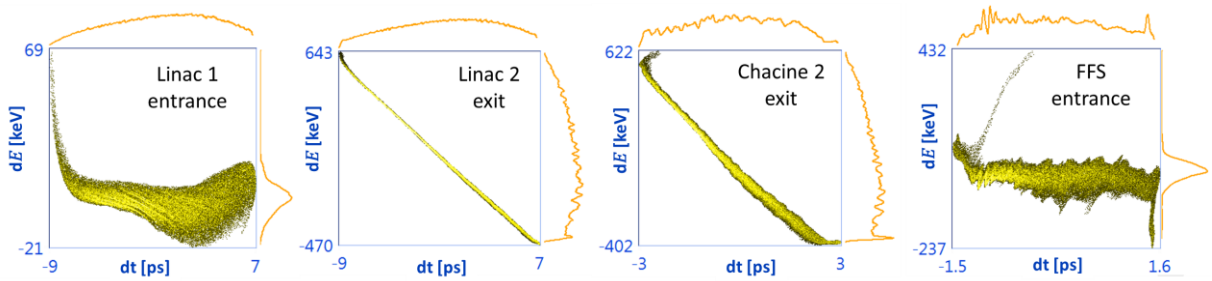

Fig. 2.43 Bunch distributions in LPS at different positions of CBS beam transport. The u-crescent from the dogleg is alleviated to quasi-linear at the entrance of FFS.

The transverse beam transport is performed with automatic optimizations using the simulation tool, keeping the beam size always smaller than the beam pipe. The transverse emittance is optimized at the exit of Chicane 2 as well as at the entrance of FFS. With minimized energy spread and minimized emittance for the input beam, FFS is optimized to achieve the smallest beam spot size at the CBS point where electrons will interact with laser pulses. The bunch distribution is shown in Fig. 2.44, while the parameters of the final bunch are presented in Table 2.6.

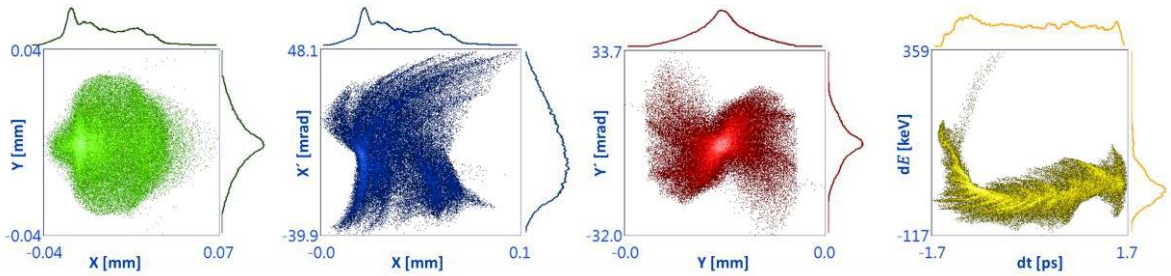

Fig. 2.44 Optimized bunch distribution (200 pC) in phase space at the CBS point.

Table 2.6 Optimized parameters of 200 pC beam for CBS at the electron-laser interaction point.

$\bar{E}$ [MeV]	23.0	σ_t [ps]	1.05
σ_E [keV]	33.8	t_{FWHM} [ps]	0.48
σ_x [mm]	0.016	σ_y [mm]	0.015
x_{FWHM} [mm]	0.017	y_{FWHM} [mm]	0.036
$\sigma_{x'}$ [mrad]	19.7	$\sigma_{y'}$ [mrad]	18.6
ε_x [μm]	14.1	ε_y [μm]	4.3

As the most critical parameter, the FWHM transverse beam size of the final bunch is 17 μm horizontally and 36 μm vertically, although rms sizes (σ_x and σ_y) are very close (Table 2.6). The highest outcome X-ray flux of CBS experiments depends on the spatial matching of the interacting electron bunch and the photon pulse. Usually a symmetric distribution is desired, however, Fig. 2.44 shows that the focused bunch is not horizontally symmetric. By analyzing O_{kx}, the horizontal overlap ratio of slices, it is found that the asymmetry origins from the dogleg. With the bunch divided into 10 slices, O_{kx} at the entrance and exit of dogleg is 0.28 and 0.72 respectively. Then O_{kx}varies by $\pm 10\%$ along the beamline and at the CBS point it is 0.67. In addition to generating the asymmetry, the dogleg is also the main reason for emittance growth, as shown in Fig. 2.41.

To summarize, a 200 pC beam has been transported from the SRF gun to CBS experimental station, with parameters satisfying the requirements in Table 1.3. Parameter combination D is used instead of C, with increased cathode position to generate a linear distribution in LPS. The energy spread and transverse emittance are optimized at the entrance of FFS, which focuses the beam strongly to the minimum possible size of rms 0.16 μm or FWHM 0.36 μm. Parameters used in this simulation can be found in Appendix II.

3. Beam diagnostic methods

3.1. The measurement of laser pulse length

The pulse length of the UV laser determines the initial length of the electron bunch. A well-known method of measuring laser pulse length is “auto-correlation”. In this method the laser is separated to two beams and one of them is delayed. Next, a Second Harmonic Generation (SHG) crystal is used to generate the self-correlated signal from the two laser beams. In the end, the temporal profile of the self-correlated signal is obtained by measuring its intensity while scanning the delay time, which contains the longitudinal information of the initial laser pulse. The setup of this method is illustrated in Fig. 3.1.

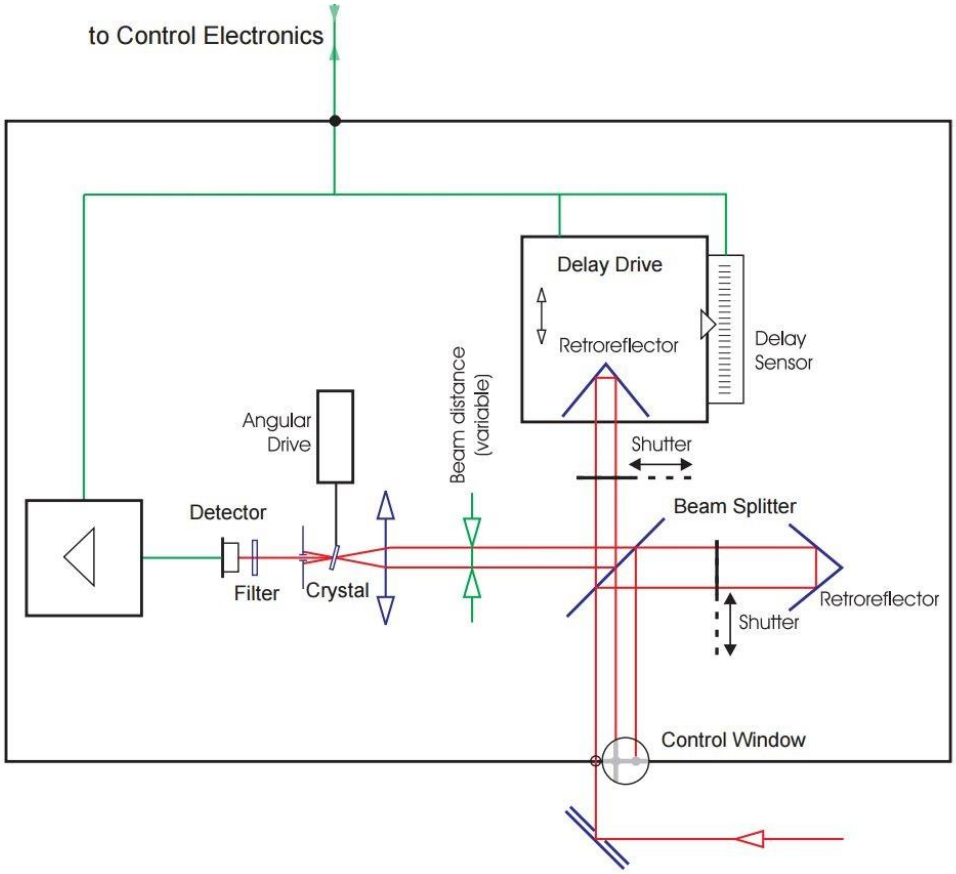

Fig. 3.1 The sketch of the auto-correlation method of measuring the laser pulse length [76].

For a laser pulse which is Gaussian distributed in time, the auto-correlated signal is also Gaussian distributed, and the length of the laser pulse can be calculated by:

$$\sigma_{laser} = \frac{\sqrt{2}}{2}\sigma_{aut} \tag{3-1}$$

where σ_{aut} is the pulse length of the auto-correlated signal.

However, for pulse lengths below 410 nm, e. g., 263 nm of the laser used for ELBE SRF gun, no SHG crystal is available. As a result, the method of cross-correlation has to be applied instead.

The cross-correlation mehod requires a second laser beam with a given temporal profile which will be crossed with the laser to be measured. A Difference Frequency Mixing (DFM) crystal is applied to generate the cross-correlated signal. It is required that the two laser beams have the same repetition rate and overlap well spatially. One of them will be scanned temporally to measure the pulse length of the cross-correlated signal. The pulse length of the unknown beam is:

$$\sigma_{laser}=\sqrt{{\sigma_{cro}}^2-{\sigma_{known}}^2} \tag{3-2}$$

where σ_{cro} and σ_{known} are the pulse length of the cross-correlated signal and that of the second laser beam respectively.

The UV laser used for the ELBE SRF gun is the fourth harmonic of an infrared (IR) laser with a wavelength of 1053 nm. Both lasers have the same repetition rate, thus, the IR laser beam is a good candidate to perform the cross correlation with the UV laser.

A commercial product of auto/cross-correlator from A.P.E Company [76] is used, which is capable of both auto- and cross-correlation by switching the crystal. The correlator and the setup is shown in Fig. 3.2.

The pulse structure of the IR laser is measured by auto-correlation and then used to analyze the UV laser. The scanning range of the optical path in this correlator is 150 ps, limiting the maximum acceptable temporal difference of the incident IR and UV beam to 75 ps for cross correlation. To satisfy this requirement as well as the spatial overlap, an extra section of the laser beamline has been built up as shown in Fig. 3.3. Dichroic mirrors separate different harmonics of the laser. A retroreflector is installed on a delay stage to control the temporal overlap between IR and UV laser beams. A fast diode with 300 ps rise-up time is used to monitor the temporal overlap. The intensity of the IR beam, which is much stronger than the UV beam, can be adjusted with a polarizer and a wave plate. The detector for cross-correlation is very sensitive to the second harmonic (green) and hence the rest green beam is filtered by a Pellin Broca prism.

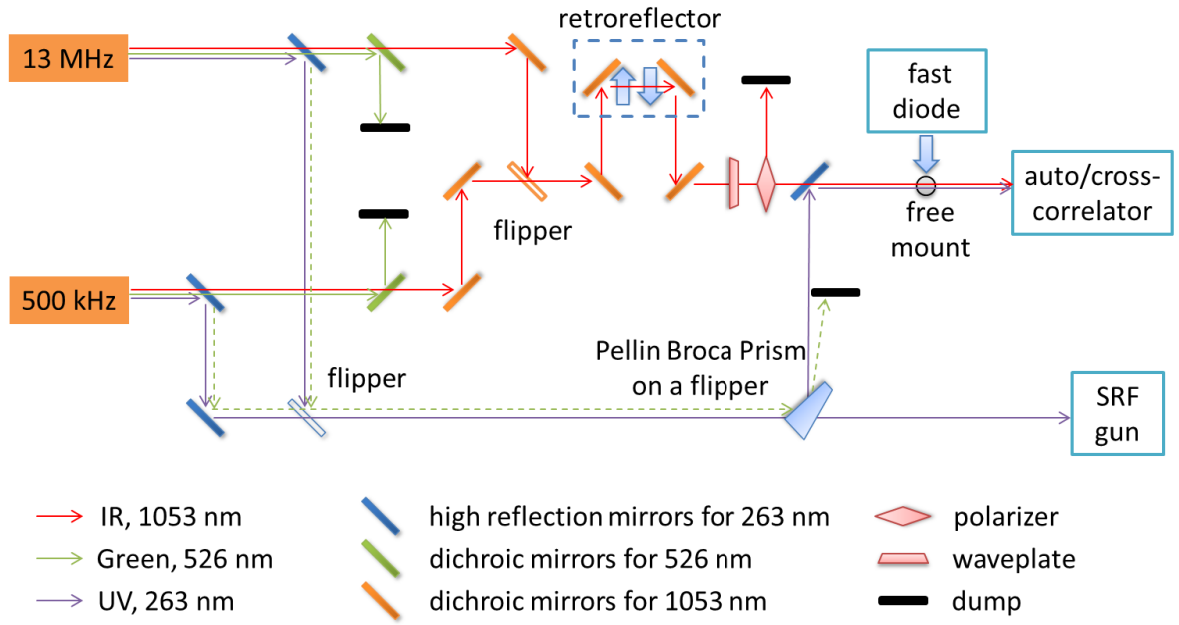

Fig. 3.2 The setup of the preparation beamline for auto/cross-correlator, for both 13 MHz and 500 kHz channels.

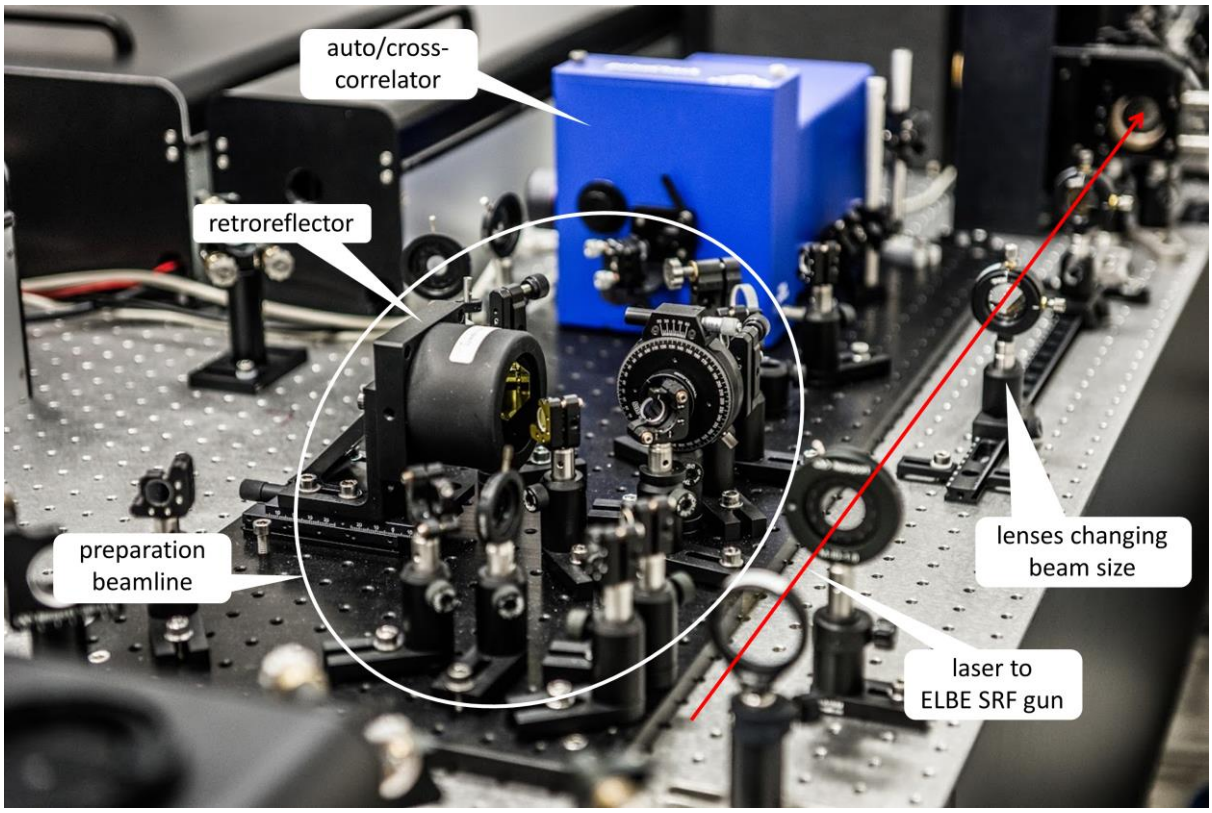

Fig. 3.3 The auto/cross-correlator from A.P.E Company and the preparation beamline installed in the laser system of ELBE SRF gun.

3.2. Measurement of energy and energy spread

Energy and energy spread of beams at ELBE are measured mainly by dipoles. An example in the diagnostics beamline of the SRF gun is introduced in this section.

As shown in Fig. 2.17, a diagnostics beamline is connected directly behind the ELBE SRF gun, of which the setup is shown in Fig. 3.4. A Faraday cup is installed at 0.77 m from the SC solenoid to measure the total current. After the Faraday cup, three quadrupoles focus the beam for further transport, followed by Screen-station 2 and 3 for beam observation and slit-scan emittance measurement, as presented in Section 3.3.

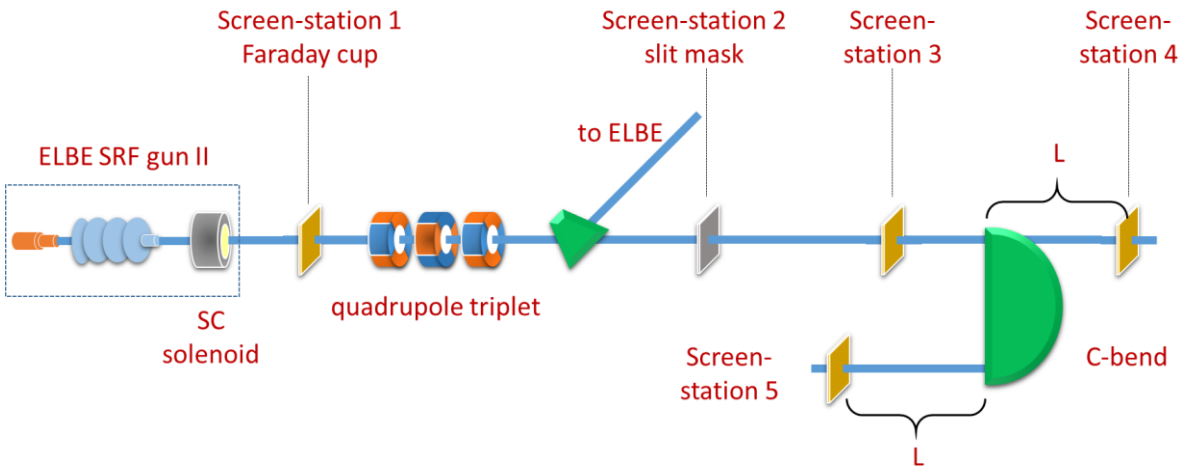

Fig. 3.4 The diagnostics beamline of ELBE SRF gun.

A 180° horizontal dipole (C-bend) is installed following Screen-station 3 for energy measurement, which images the input beam reversely. The distance from its entrance to Screen-station 4 is the same as the distance from its exit to Screen-station 5, as shown in Fig. 3.4. Therefore, projections of a monoenergetic beam on both screens should be the same.

Based on the above-mentioned settings in the diagnostics beamline, energy and energy spread of an electron beam from the SRF gun can be measured step by step:

Firstly, the beam should be transported through the center of both Screen-station 3 and 4, with the C-bend and all steering magnets turned off between the two stations. In this case, the beam is travelling in the center of the beam pipe, and hence injecting into the C-bend perpendicularly. Secondly, the beam should be focused horizontally at Screen-station 4 to reduce the influence from transverse phase space, as shown in Equation (3-4). Then the C-bend can be turned on and the beam is transported to Screen-station 5.

The energy of the beam is given by:

$$\overline{E}=ecB_{bend}R_{bend}=C_E\cdot I_{bend} \tag{3-3}$$

where e is the charge of an electron, c is the speed of light; B_{bend} and R_{bend} are the magnetic field and bending radius of the C-bend respectively; C_E is a calibration constant with a value of 0.129 MeV/A delivered by magnetic field measurements and I_{bend} is the current of the C-bend.

The energy spread is calculated from the horizontal size of the beam projection on Screen 5, which can be decomposed into two components: one from the transverse beam transport, leading to the same beam size as that on Screen 4; the other from the dispersion in the C-bend. Hence, the calculation of the energy spread is as follows:

$$\sigma_E=C_0\sigma_{x,\,disp}=C_0\sqrt{{\sigma_{x,\,05}}^2-{\sigma_{x,\,04}}^2} \tag{3-4}$$

where $\sigma_{x,\,04}$ and $\sigma_{x,\,05}$ are the horizontal beam size on Screen 4 and 5 respectively, and $\sigma_{x,\,disp}$ is the dispersed component of beam size on Screen 5. The factor C_0 is given by $C_0=2\,R_{bend}/\overline{E}$.

One error in this measurement is caused by the alignment of Screen-stations and beam-pipes in the diagnostics beamline. In practice it is hard for the beam to drift freely from the center of Screen 3 to the center of Screen 4 without beam loss, and thus a random error is generated if the incident beam of the C-bend is not perpendicular. This error is about 5%, summarized from the measurements by different operators. Another error comes from the calibration of C_E which is estimated to be 5% to 10%. Consequently, both the relative error for energy and energy spread are estimated to be 10%, represented by $\delta\overline{E}/\overline{E}$ and $\delta(\sigma_E)/\sigma_E$ respectively.

This method of energy and energy spread measurement is also applied to other combinations of dipole and screens in the ELBE beamline. In cases without a perfect screen as Screen 4 which provides the influence of the transverse beam transport, errors of energy spread measurements should be controlled by focusing the beam at the measurement screen after the dipole.

In addition, a Browne-Buechner spectrometer [77] is installed after the entrance of nELBE branch. It contains a circular-edge dipole which images point sources with the same energy. Particles with different energies are imaged onto a plane where a screen is installed, as shown in Fig. 3.5. A vertical slit is used to select a narrow beamlet and thus the effect of beam size

on the energy spread measurement is eliminated. Using the slit, the horizontal energy distribution in the bunch is neglected.

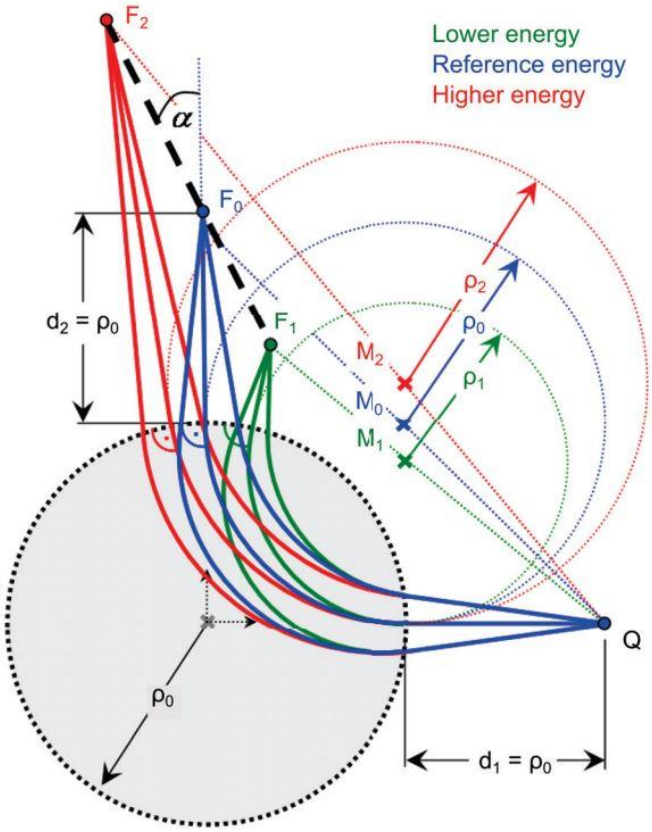

Fig. 3.5 The sketch of Browne-Buechner spectrometer [78].

3.3. Slit scan emittance measurement

3.3.1. Introduction

This section introduces a well-known emittance measurement method called "slit-scan". The idea is to measure the intensity distribution at a number of points in transverse phase space, and the normalized rms emittance can be calculated according to:

$$\varepsilon_u = \beta\gamma\varepsilon_{ug} = \beta\gamma\sqrt{u^2_{ave} \cdot u'^2_{ave} - uu'^2_{ave}} \tag{3-5}$$

and :

$$\begin{aligned} u^2_{ave} &= \frac{\sum[I_i(u_i - u_{ave})^2]}{\sum I_i} \\ u'^2_{ave} &= \frac{\sum[I_i(u'_i - u'_{ave})^2]}{\sum I_i} \\ uu'_{ave} &= \frac{\sum[I_i(u_i - u_{ave})(u'_i - u'_{ave})]}{\sum I_i} \\ u_{ave} &= \frac{\sum(I_i u_i)}{\sum I_i} \\ u'_{ave} &= \frac{\sum(I_i u'_i)}{\sum I_i} \end{aligned} \tag{3-6}$$

where u and u' are the coordinates of the position and angle in a transverse direction (e.g., x or y); I is the measured intensity; the subscript i is the index of measured points; β and γ are the relativity parameters and ε_{ug} is the geometric emittance.

To measure I_i, particles with particular position and angle must be sampled from the beam. Beamlets from different positions are selected by a slit scanning transversely through the beam. In the sampled beamlet from each position, particles travelling with different angles are separated after some distance and are projected onto a downstream screen. The image on the screen is recorded by a CCD camera. The accumulation of pixel values generates the angle distribution of the beamlet. The basic setup of the slit-scan emittance measurement is shown in Fig. 3. 6.

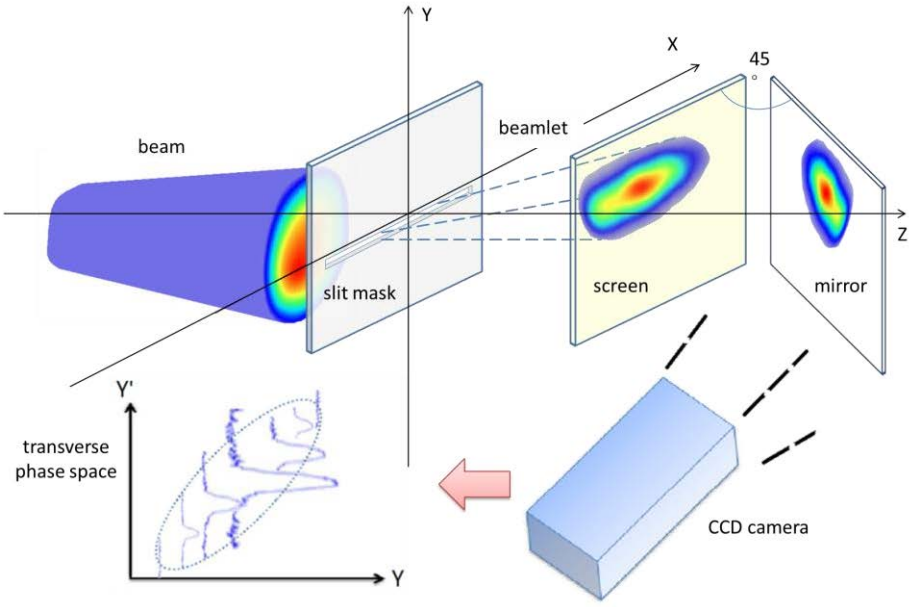

Fig. 3. 6 The basic setup of the slit-scan emittance measurement.

3.3.2. Setup, software and measurement procedures

In the diagnostics beamline introduced in Fig. 3.4, a 1 mm thick slit mask is installed at the position of Screen-station 2. It is vertically moveable with a horizontal slit, which has the dimension of 10 mm × 0.1 mm. Screen 3 is located 77 cm after the slit mask to record the sampled beamlets. The setup of Screen-station 2 and 3 is shown in Fig. 3.7. The calibration screen has a coordinate system for calculating the dimension of pixels.

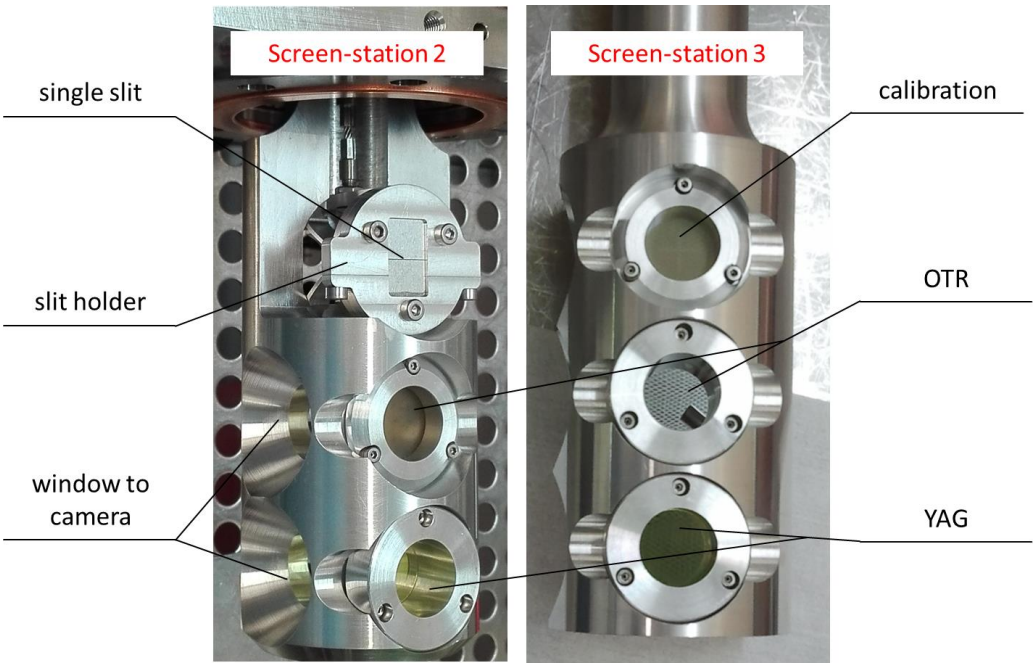

Fig. 3.7 The structure of Screen-station 2 and 3.

During the measurement, the beam should be first transported through the center of Screen 2 and 3, with no steering magnets turned on between them. In this case, the beam injects into the slit mask perpendicularly and the sampled beamlet travels freely between the two stations so that its angle can be measured correctly. In the next step, the entire beam should be focused at Screen 2 to be smaller than the length of the slit (10 mm) for complete sampling. Meanwhile, on Screen 3 the beam size should also be controlled to stay within the screen size, so that all beamlets can be recorded by the CCD camera.

To shorten the measurement time, the slit is usually scanned roughly in advance to decide the scanning range. In the meantime, the exposure time of the camera should be adjusted to avoid saturation for every beamlet. The scanning step is usually set to 0.1 mm, which is the width of the slit, and thus the entire beam is sampled.

After the above preparation steps which are conducted manually, the following measurement and calculation are conducted automatically by the software.

The control of step motors and the CCD camera are combined in one LabVIEW program to perform the automatic emittance measurement, as shown in Fig. 3.8. CCD cameras are focused in advance on screens, with their exposure time and the trigger remotely changeable in the program. Other important input parameters include the range and the step of scanning, the number of images to record at each position and the beam energy.

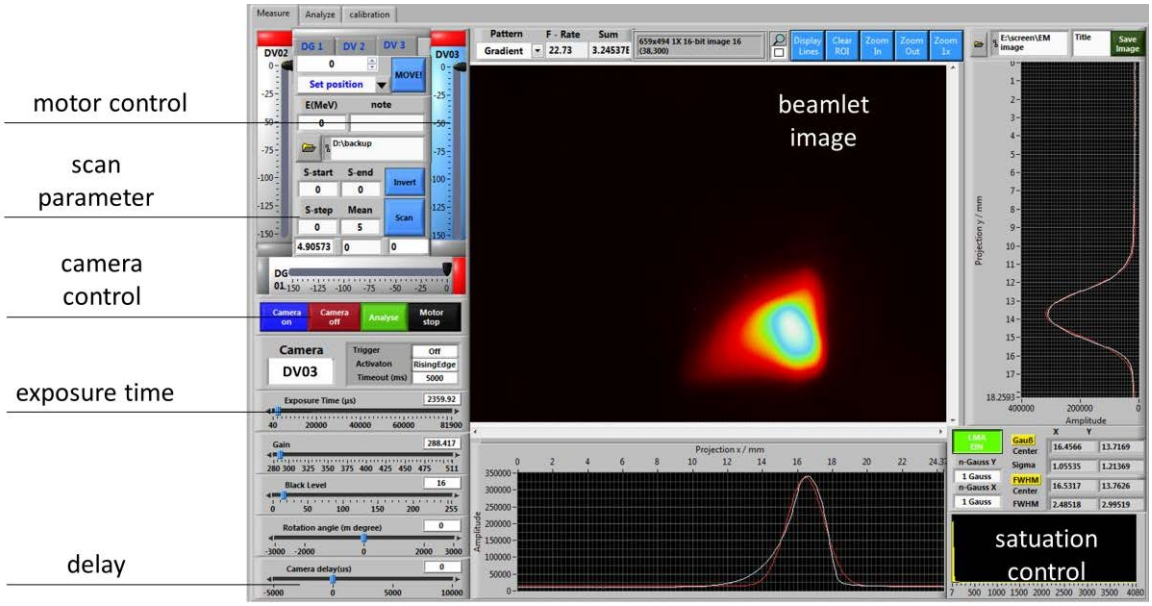

Fig. 3.8 Emittance measurement program for the ELBE SRF gun.

3.3.3. Image processing

The processing of images recorded by screens and cameras before using them for calculation composes an important part of this thesis. The method to be introduced in the following is also applied for all other screen based diagnostics at ELBE. Here, image processing includes choosing proper areas, subtracting the background, distinguishing beamlet signals and removing noise. As each measurement generates several hundreds of images, an automatic, universal and fast image processing algorithm is necessary.

The first step of image processing is to choose a proper area. The number of pixels directly affects the calculation time, therefore a proper area should contain as few pixels as possible but maintain all the information of beamlets. In the early stage, fittings were applied for this purpose, however, fittngs are not universal for all cases as the distribution of beamlets which depends on the beam quality is unpredictable, even roughly. For example, sometimes several peaks appear in the beamlet with different travelling angles, making pre-defined fitting for general cases unsuitable. The image processing method should effectively cover all situations especially for diagnosing bad beam qualities, and thus fittings were cancelled. Instead, all beamlet images are integrated to rebuild the entire beam, and by displaying it, a proper area can be chosen manually. This area is not the smallest for an individual beamlet, but it still significantly reduces the number of pixels to be processed. As shown in Fig. 3.9, the button of "sum" displays the rebuilt beam in the left window with intensity adjustable for users to locate the edge of the beam. This manual operation is acceptable because it occurs only once for one measurement.

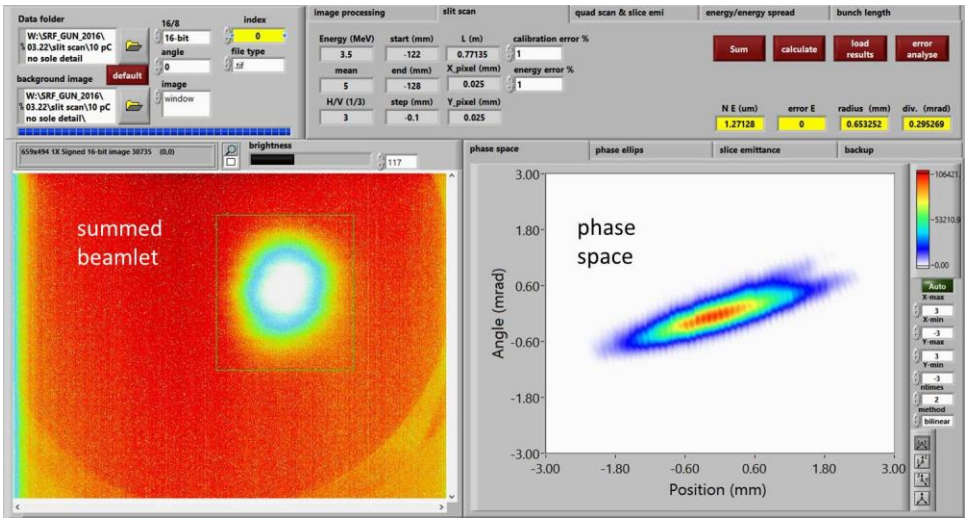

Fig. 3.9 Data processing program for the slit-scan emittance measurement.

The second step is to subtract the background. Pixel values of the image taken by the CCD camera are not exactly zero even when the beam is off. But rms calculations in Equation (3-3) and (3-4) are very sensitive to noise. At the edge of measured phase space where u or u' is large, even small noise in intensity will influence the rms value.

The usual way of removing the background is to subtract an image taken without beam. This method is kept as an option that a pre-saved background image can be selected for subtraction. However, when the beam intensity is strong enough, some reflections illuminate the entire screen, resulting in all pixel values larger than that of the background image. The background subtracting in this case is not adequate.

To represent the background, 10×10 pixels at each corner ($\times 4$) of the chosen area are selected. The average of these pixel values is subtracted from the image as background and then their standard deviation is used as a threshold, such that pixel values smaller than three times of the threshold are set to zero. As shown in Fig. 3.10, the calculated emittance for a single beamlet changed significantly after subtracting the background.

The third step is to distinguish beamlet signals from noise pixels. Again, pre-defined fitting is not applied as the beamlet distribution is unknown. Fig. 3.10 illustrates two cases with different beamlet distributions. One is an ideal case with a normal Gaussian distribution and the other is a special case at the edge of a bad-quality beam. Here the intensity of the beamlet signal is lower than that of most noise pixels and several separate signal peaks appear. A definition of beamlet signal not including the intensity is needed to distinguish signals from noise.

In Reference [79], noise with a pixel number lower than a threshold are deleted, cycling the pixel number. The larger the threshold the longer the processing time. In this thesis the definition of beamlet signals is “pixel clusters with more than 50 connected non-zero pixels”. The number 50 is selected by experience, as most noise occupy less than 10 pixels and most beamlet signals occupy more than 100 pixels. Consequently, clusters with less than 50 non-zero pixels are deleted. For such a high threshold of 50, an algorithm for distinguishing beamlet signals is developed avoiding cycling the pixel number for 50 times:

(1) Mark all pixels by 0 or 1. 1 represents any non-zero value.

(2) Scan all pixels until the next pixel marked with 1 is found. Save its index as the "center index" in an array of indexes for pixels in one cluster, named S.

(3) Check the mark of the surrounding pixels. If any pixel is marked with 1 while its index is not in Array S, insert its index into the end of Array S.

(4) Scan Array S from the beginning, set the first element to be the "center index" and repeat Step (3) till the end of Array S. Now all indexes saved in this array are from one cluster, which can be either beamlet signals or noise.

(5) Count the size of Array S. If it is less than 50, mark 0 to all pixels saved in Array S; If larger than 50, mark it with 2 which represents processed.

(6) Repeat Step (2) to (5) until all pixels are scanned. Finally, the value of all pixels marked with 0 should be set to zero and the rest of non-zero pixels are beamlet-signals.

The last step of image processing is to get rid of noise overlapping with beamlet signals. The method applied here is to cut the image to sub-areas of 5 × 5 pixels. In each sub-area, if any pixel value is larger than three times of the standard deviation plus the average of all 25 pixels, it will be replaced by the average value. This method has been tested to be suitable for all data, but it is time consuming. Another wavelet based approach reduces the processing time to a negligible level, however, it is not universally applicable.

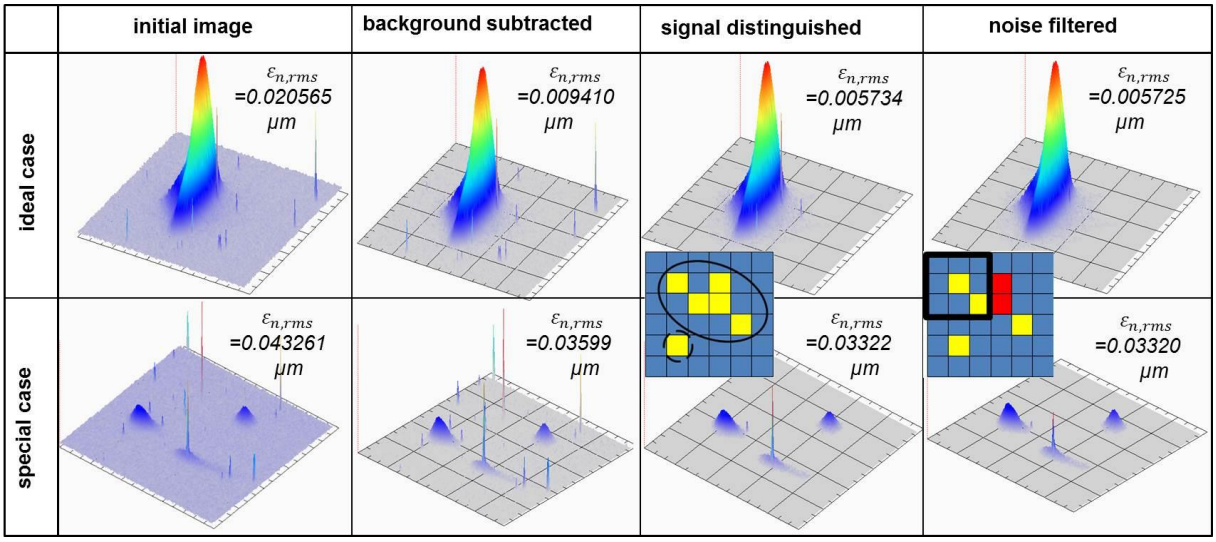

Fig. 3.10 Image processing algorithm for the slit-scan emittance measurement and all other screen-camera based beam diagnostics in this thesis.

3.3.4. Error analysis of slit-scan emittance measurement

The error of the slit-scan emittance measurement can be attributed to the error of dimensions $\delta\varepsilon_u(\mathrm{dim})/\varepsilon_u$, the error of slit collimation $\delta\varepsilon_u(\mathrm{slit})/\varepsilon_u$, the error of energy measurement $\delta\varepsilon_u(\overline{E})/\varepsilon_u$, the error of pixel-based calculation $\delta\varepsilon_u(\mathrm{pix})/\varepsilon_u$ and the error of instability $\delta\varepsilon_u(\mathrm{inst})/\varepsilon_u$. These five sources of errors are explained in this section.

- The error of dimensions

  The pixel size of beamlet images is obtained from a calibration glass screen with a millimeter scale at the same Screen-station. The angle of particles is calculated according to the distance between the slit and the measurement screen. Errors of pixel calibration and angle calculation are estimated to be less than 1%. By assigning such an error in the emittance calculation program, the value of emittance varies by about 1%. This value is used as the relative emittance error from geometric calibration, $\delta\varepsilon_u\,(\mathrm{dim})/\varepsilon_u = 1\ \%$.

- The error of slit collimation

  The width of the slit is 0.1 mm and the thickness of the slit mask is 1 mm. A part of the incident particles traveling with a non-zero angle will be lost. The portion of lost particles is given by $T_s \cdot \theta_i / W_s$, where T_s is the thickness of the slit plate, θ_i is the incident angle and W_s is the width of the slit, as shown in Fig. 3.11. The lost portion can be calculated, given the values of T_s, W_s and θ_i. However, the position of the slit relative to the screen is unknown due to inaccuracy of their mechanical installation. Therefore, the actual value of θ_i is unknown. Compared to u' in Equation (3-6) which indicates the angle of particles with respect to the movement of the beam center, θ_i is the angle with respect to the accelerator axis. By estimating a maximum lost portion of 5% for particles at the edge of the beam, the value of emittance varies by about 1.5%, depending on the specific bunch distribution. Therefore, the relative error of emittance from slit collimation is estimated to be $\delta\varepsilon_u\,(\mathrm{slit})/\varepsilon_u = 2\ \%$.

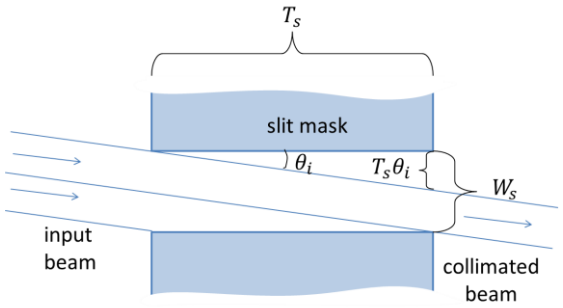

Fig. 3.11 An illustration of slit-collimation induced error of the slit-scan emittance measurement.

- The error of energy measurement

  The accuracy of energy measurement affects relativity parameters, β and γ, which influence the normalization of emittance. In the calculation program, it is allowed to

input error of the energy measurement which will be further used to calculate the relative error from the normalization:

$$\frac{\delta\varepsilon_u(\overline{E})}{\varepsilon_u} = \frac{1}{\beta^2} \cdot \frac{\delta\overline{E}}{\overline{E}} \tag{3-7}$$

- The error of pixel-based calculation

The geometric emittance is calculated from the pixel values of images recorded by a CCD camera. All pixel values have statistical errors. In this thesis, the standard deviation of pixel values for the background, σ_I, is used as an estimated error for all pixels. From Equation (3-5) and (3-6), the error from the pixel values is calculated automatically in the program according to:

$$\begin{aligned}\frac{\delta\varepsilon_u(pix)}{\varepsilon_u} = \frac{\pm\sigma_I}{\varepsilon_u \sum I_i}[&\left(\frac{u^2{}_{ave}}{2}\right)^2 \sum((u_i - u_{ave})^2 - u^2{}_{ave})^2 \\ &+ \left(\frac{u'^2{}_{ave}}{2}\right)^2 \sum\left((u'_i - u'_{ave})^2 - u'^2{}_{ave}\right)^2 \\ &+ (uu'_{ave})^2 \sum((u_i - u_{ave})(u'_i - u'_{ave}) - uu'_{ave})^2]^{1/2}\end{aligned} \tag{3-8}$$

- The error of beam instability

During the emittance measurement, the camera is usually exposed to at least 10 pulses of the beam at one position to record a single image, and about 30 to 50 positions are scanned in one measurement. If the beam is not stable, an error will be generated in the multi-pulse emittance measurement.

To gauge the influence of the beam instability, a simulation of the slit-scan measurement has been conducted with 40 bunches with random distributions in phase space. For each bunch distribution, a white noise is added to the transverse beam position as an offset, with the amplitude set to 20% of the transverse beam size. Such a white noise is parameterized according to an instability measurement on Screen 2 using a CCD camera. With this white noise, a virtual sampling is performed to exactly imitate the slit and thus the emittance is virtually measured. The ratio of the virtually measured emittance to the actual emittance increases with $\beta_u\gamma_u$ of the bunch, where β_u and γ_u are Twiss parameters, as shown in the right diagram in Fig. 3.12. Meanwhile, the left diagram in Fig. 3.12 shows no obvious trend between the statistic error of virtually measured emittance and $\beta_u\gamma_u$ of the bunch.

The value of $\beta_u\gamma_u$ measures how "fat" the phase ellipse is. As shown in Fig. 3.13, bunches with larger $\beta_u\gamma_u$ are "thinner", therefore the instability of the transverse offset enlarges the bunch distribution in TPS more significantly, leading to a larger systematic error of the emittance.

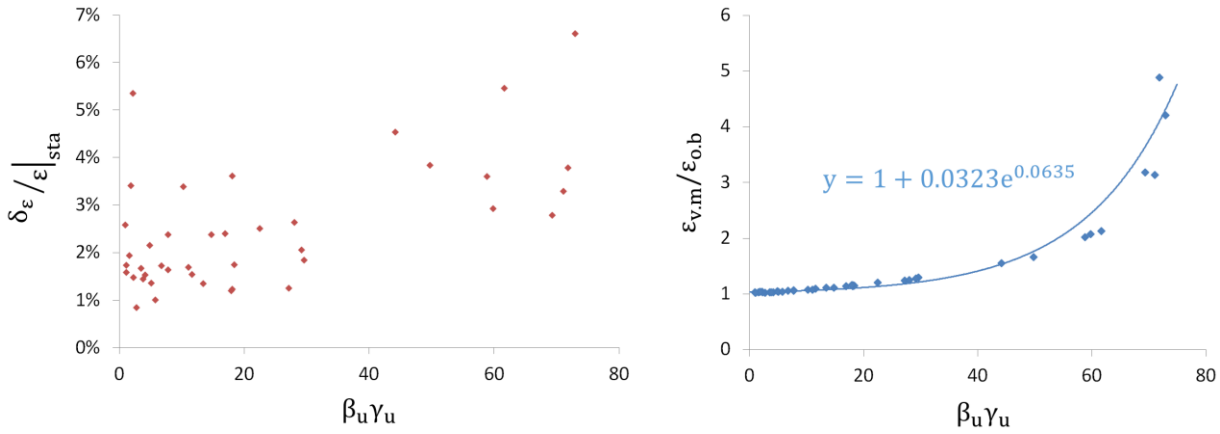

Fig. 3.12 Instability-induced statistical error (left) and systematical error (right) calculated from the virtual measurement.

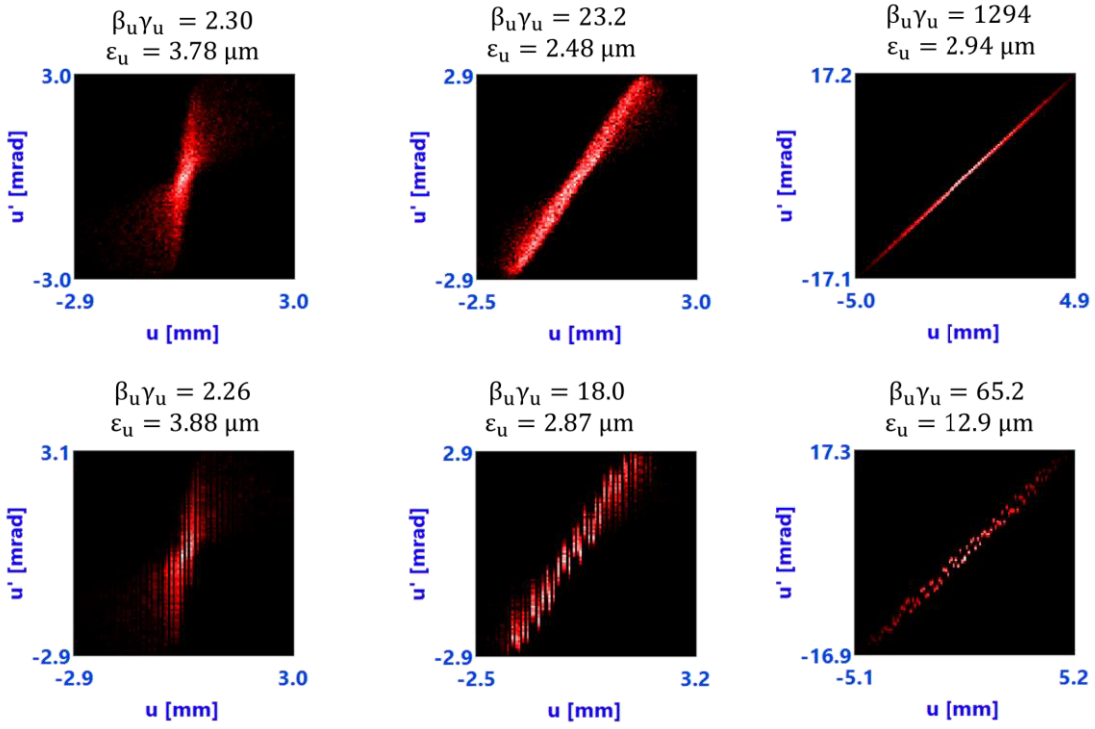

Fig. 3.13 Three examples presenting the dependence of instability-induced systematic error on $\beta_u\gamma_u$. The three distributions on top are the initial bunches and the three distributions at the bottom are the corresponding bunches that are virtually sampled.

As a solution, the systematic errors are corrected by the fitting result which is shown in Fig. 3.12:

$$\varepsilon_{ucor}=\frac{\varepsilon_u}{1+0.0323e^{0.0635\beta_u\gamma_u}} \tag{3-9}$$

The measured white noise on transverse beam position is assumed to come from vibrations of ELBE and it is potential to be reduced by soft connections of pumps. Meanwhile, to achieve the minimum value of $\beta_u\gamma_u$ by focusing the beam, i. e., to the beam waist, is also effective to reduce this systematic error.

According to the left diagram in Fig. 3.12, the statistical instability induced error is estimated by $\delta\varepsilon_u\,(\mathrm{inst})/\varepsilon_u=10$ %.

The total error of slit-scan emittance measurement is the rms of the above five errors:

$$\left.\frac{\delta\varepsilon}{\varepsilon}\right|_{ss}=[(\frac{\delta\varepsilon(\mathrm{dim})}{\varepsilon})^2+(\frac{\delta\varepsilon(\mathrm{slit})}{\varepsilon})^2+(\frac{\delta\varepsilon(\overline{\mathrm{E}})}{\varepsilon})^2+(\frac{\delta\varepsilon(\mathrm{pix})}{\varepsilon})^2+(\frac{\delta\varepsilon(\mathrm{inst})}{\varepsilon})^2]^{1/2} \tag{3-10}$$

3.4. Quadrupole scan emittance measurement

3.4.1. Introduction

Quadrupole scan is another widely applied method for emittance measurement in emittance-dominated beams. The principle is to utilize the beam transport matrix to derive the emittance. Its setup is basically the combination of a quadrupole and a downstream screen with a proper drift distance. When the quadrupole strength changes for measurement, the beam should be completely projected on the screen.

In a general case where a beam is transported from Position 0 to Position 1 and considering one transverse dimension only, the matrix in between is represented by M:

$$M=\begin{pmatrix} a & b \\ c & d \end{pmatrix} \tag{3-11}$$

such that:

$$\begin{pmatrix} u_0 \\ u'_0 \end{pmatrix} = \begin{pmatrix} a & c \\ b & d \end{pmatrix} \begin{pmatrix} u_1 \\ u'_1 \end{pmatrix} \tag{3-12}$$

where u_0 and u'_0 represent the position and the angle of a particle at Position 0 while u_1 and u'_1 represent the position and the angle of this particle at Position 1, respectively. The beta function between these two positions is:

$$\beta_1 \varepsilon_{ug} = a^2 \beta_0 \varepsilon_{ug} - 2ac\alpha_0 \varepsilon_{ug} + c^2 \gamma_0 \varepsilon_{ug} \tag{3-13}$$

Where β_1 is the Twiss parameter at Position 1, α_0, β_0 and γ_0 are Twiss parameters at Position 0, ε_{ug} is the geometric emittance of the beam which is assumed to be constant in the quadrupole-scan emittance measurement.

Rewrite Equation (3-13) in a compact way gives:

$$f = Ax + By + Cz \tag{3-14}$$

and

$$\begin{gathered} f=\beta_1\varepsilon_{ug}=\sigma_{u1}{}^2 \\ A=\beta_0\varepsilon_{ug}=\sigma_{u0}{}^2 \\ x=a^2 \\ B=\alpha_0\varepsilon_{ug} \\ y=-2ac \\ C=\gamma_0\varepsilon_{ug} \\ z=c^2 \end{gathered} \tag{3-15}$$

where σ_{u0} and σ_{u1} are the rms beam size at Position 0 and Position 1 respectively.

x, y and z can be calculated from the matrix M. By changing the matrix M, several combinations of (f, x, y, z) are available, and then the problem of deriving ε_{ug} is equivalent to fitting the best values of A, B and C with the known combinations of (f, x, y, z). Mathematically, the least squares method can be applied, which is to minimize the following objective function representing the sum squared differences of all groups between fitted and measured data:

$$\mathrm{Rest}=\sum\left[\frac{1}{\sigma_{fj}}(f_j-Ax_j-By_j-Cz_j)^2\right] \tag{3-16}$$

where the subscript j is the index of data group with different values of M, σ_{fj} is the error of the measured f_j and $1/\sigma_{fj}$ is the weighting factor. The more accurate f_j is measured (lager $1/\sigma_{fj}$), the more important the corresponding group is. The optimal values for A, B and C to minimize Rest should satisfy the first order conditions:

$$\begin{gathered} \frac{\partial \mathrm{Rest}}{\partial A}=0 \\ \frac{\partial \mathrm{Rest}}{\partial B}=0 \\ \frac{\partial \mathrm{Rest}}{\partial C}=0 \end{gathered} \tag{3-17}$$

Replacing Rest in Equation (3-17) by Equation (3-16), the solution for A,B and C is:

$$\begin{pmatrix} A \\ B \\ C \end{pmatrix}=\begin{pmatrix} \sum\frac{f_jx_j}{\sigma_{fj}} \\ \sum\frac{f_jy_j}{\sigma_{fi}} \\ \sum\frac{f_jz_j}{\sigma_{fj}} \end{pmatrix}\begin{pmatrix} \sum\frac{x_j^2}{\sigma_{fj}} & \sum\frac{x_jy_j}{\sigma_{fj}} & \sum\frac{x_jz_j}{\sigma_{fj}} \\ \sum\frac{y_jx_j}{\sigma_{fj}} & \sum\frac{y_j^2}{\sigma_{fj}} & \sum\frac{y_jz_j}{\sigma_{fj}} \\ \sum\frac{z_jx_j}{\sigma_{fj}} & \sum\frac{z_jy_j}{\sigma_{fj}} & \sum\frac{z_j^2}{\sigma_{fj}} \end{pmatrix}^{-1} \tag{3-18}$$

With the solved A, B and C, the emittance as well as Twiss parameters at Position 0 can be calculated by Equation (2-1) and (3-15),

$$\begin{aligned}\varepsilon_{ug}&=\sqrt{AC-B^2}\\ \beta_0&=\frac{A}{\sqrt{AC-B^2}}\\ \alpha_0&=\frac{B}{\sqrt{AC-B^2}}\\ \gamma_0&=\frac{C}{\sqrt{AC-B^2}}\end{aligned} \tag{3-19}$$

The above deduction is not limited to quadrupole scan. Any change of the transport matrix influencing the downstream beam size can be used to measure the transverse emittance.

As a special application of quadrupole scan with Position 0 being the entrance of a quadrupole and Position 1 being a downstream screen, the transport matrix M_{qs} is the product of the matrixes for the drift space and the quadrupole:

$$M_{qs}=\begin{pmatrix}1 & l_d\\ 0 & 1\end{pmatrix}\cdot\begin{pmatrix}\cosh(\sqrt{k_q}l_q) & \frac{1}{\sqrt{k_q}}\sinh(\sqrt{k_q}l_q)\\ -\sqrt{k_q}\sinh(\sqrt{k_q}l_q) & \cosh(\sqrt{k_q}l_q)\end{pmatrix} \tag{3-20}$$

where k_q is the quadrupole strength, l_q is the effective length of the quadrupole and l_d is the length of the drift space. By setting several values of k_q and measuring corresponding beam sizes, the emittance can be calculated by Equation (3-14) to (3-20).

3.4.2. Error analysis of quadrupole scan emittance measurement

The measurement of beam size at Position 1 is based on screens and cameras. Before calculation, the image processing procedures described in Section 3.3.3 are applied first.

σ_{fj} is not only an error but also directly influences the value of the emittance, as it appears in Equation (3-18). It is calculated based on the statistical error of pixel values, σ_I, as in the following equation:

$$\sigma_{fj}=\sqrt{\sum\left(\frac{\partial {\sigma_{u1}}^2}{\partial I_i}\cdot\sigma_I\right)^2}=\frac{\sigma_I}{\sum I_i}\sqrt{\sum\left({u1_i}^2-f_j\right)^2} \tag{3-21}$$

The error of emittance caused by σ_{fj} can be calculated by:

$$\frac{\delta\varepsilon(\sigma_{fj})}{\varepsilon}=\sqrt{\sum\left(\sigma_{fj}\cdot\partial\varepsilon_{ug}/\partial f_j\right)^2} \tag{3-22}$$

However, according to Equation (3-17) and (3-18) the analytical solution of ε_{ug} as a function of f_j is very complicated, therefore, a simplified approximation is applied instead:

$$\frac{\delta\varepsilon(\sigma_{fj})}{\varepsilon}=\frac{1}{2\varepsilon_{ug}}\left|\varepsilon_{ug}-\varepsilon_{ug,\,f_j+\sigma_{fj}}\right|+\frac{1}{2\varepsilon_{ug}}\left|\varepsilon_{ug}+\varepsilon_{ug,\,f_j-\sigma_{fj}}\right| \tag{3-23}$$

$\varepsilon_{ug,\,f_j+\sigma_{fj}}$ and $\varepsilon_{ug,\,f_j-\sigma_{fj}}$ are the emittance calculated by replacing f_j in Equation (3-16) with $f_j+\sigma_{fj}$ and $f_j-\sigma_{fj}$, respectively. The idea is to estimate the influence on the emittance when all f_j has unipolar errors.

Other errors, including the error from the transport matrix M and the error from space charge effects during transport, are negligible for low bunch charge densities compared to $\delta\varepsilon(\sigma_{fj})/\varepsilon$. Considering the normalization of emittance, the total error estimated for quadruple-scan emittance measurement is given by the rms value of $\delta\varepsilon(\sigma_{fj})/\varepsilon$ and the error from energy measurement $\delta\varepsilon(\overline{E})/\varepsilon$:

$$\left.\frac{\delta\varepsilon}{\varepsilon}\right|_{qs}=\left[\left(\frac{\delta\varepsilon(\sigma_{fj})}{\varepsilon}\right)^2+\left(\frac{\delta\varepsilon(\overline{E})}{\varepsilon}\right)^2\right]^{1/2} \tag{3-24}$$

3.4.3. Slice emittance measurement

As discussed in Section 2.5.1, to measure the emittance of temporal slices or slices with different energies is of interest in studying the slice mismatch problem. Quadrupole scan is applied to measure the slice emittance. The setup is shown in Fig. 3.14, where a dipole is used between the quadrupole and the screen to separate energy slices transversely. The slice emittance is measurable only in the transverse direction perpendicular to the bending direction of the dipole.

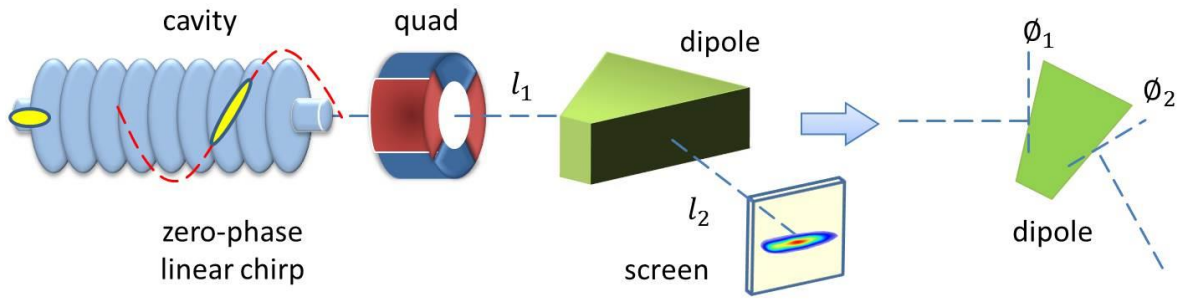

Fig. 3.14 The setup of the quadrupole based slice emittance measurement.

The quadrupole is used to vary the beam size on the screen for further fitting of the transverse emittance, which is the same as the quadrupole scan measurement. The transport matrix M_{se} here is different from M_{qs} because of the dipole. M_{se} is the product of matrices of two drift spaces, the quadrupole, the dipole and the edges of the dipole:

$$M_{se}=\begin{pmatrix}1 & l_2\\ 0 & 1\end{pmatrix}\cdot\begin{pmatrix}1 & 0\\ -\frac{\tan\theta_2}{R_d} & 1\end{pmatrix}\cdot\begin{pmatrix}\cos\frac{l_d}{R_d} & R_d\sin\frac{l_d}{R_d}\\ -\frac{1}{R_d}\cos\frac{l_d}{R_d} & \cos\frac{l_d}{R_d}\end{pmatrix}\cdot \\ \begin{pmatrix}1 & 0\\ -\frac{\tan\theta_1}{R_d} & 1\end{pmatrix}\cdot\begin{pmatrix}1 & l_1\\ 0 & 1\end{pmatrix}\cdot\begin{pmatrix}\cosh\left(\sqrt{k_q}l_q\right) & \frac{1}{\sqrt{k_q}}\sinh\left(\sqrt{k_q}l_q\right)\\ -\sqrt{k_q}\sinh\left(\sqrt{k_q}l_q\right) & \cosh\left(\sqrt{k_q}l_q\right)\end{pmatrix} \tag{3-25}$$

where θ_1 and θ_2 are the entrance and exit edge angles of the dipole; l_1 and l_2 are the lengths of drifts shown in Fig. 3.14; l_d is the length of the trajectory in the dipole and R_d is the radius of the trajectory.

With this method, the emittance of energy slices can be measured. By chirping the bunch at zero phase of a cavity in front of the quadrupole, temporal slices are separated by energy. In this case, the emittance measured for energy slices also represents the emittance of temporal slices.

The error of the temporal position of each slice comes from the size and the divergence of the incident beam of the dipole. Imagine a monoenergetic beam with the same transverse phase space passing through the dipole to the screen: the time duration calculated from the beam size on the screen (σ_{xmono}) is a good estimate of the temporal coordinate error. σ_{xmono} is not measurable, therefore in practice, it is replaced by the beam size on another screen on the straight beamline, with the closest trajectory length to the measurement screen. The error of the slice emittance can be estimated by Equation (3-24).

Using the Browne-Buechner spectrometer introduced in Section 3.2 is one of the choices for slice emittance measurement. The procedure of the error estimation was carefully analyzed in Reference [78].

4. Experimental results

4.1. Measurements of the laser pulse length

Because of the prompt response time of the metallic photocathodes, laser pulse length determines the initial length of the electron bunch. In 2015, during the commissioning of ELBE SRF Gun II with a copper cathode, an energy modulation was observed from a dispersed beam after a dipole in ELBE beamline, as shown in the left diagram of Fig. 4.1. The energy modulation implies a longitudinal density modulation of the bunch, which reflects the longitudinal laser pulse profile.

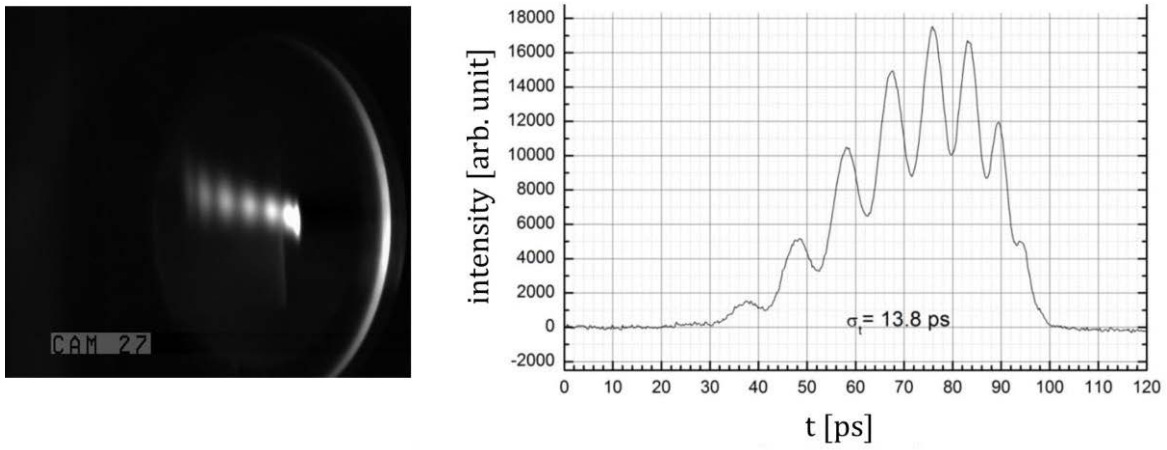

Fig. 4.1 Dispersed beam of ELBE SRF Gun II with a copper cathode, imaged on the screen behind a dipole magnet in the ELBE beamline (left). Measurement of the longitudinal profile of the UV laser pulse in the diagnostics beamline (right). A modulation of longitudinal density distribution can be observed.

An electron-beam-based diagnostics of the longitudinal laser pulse profile was conducted in the diagnostics beamline of the SRF gun. For quasi-zero bunch charges, the energy distribution in the electron bunch comes only from the difference of time when electrons are emitted from the cathode. Therefore, the energy distribution reflects the longitudinal distribution of the initial electron bunch at the photocathode, which is also the longitudinal laser pulse profile. With this method, the longitudinal profile of the laser pulse was measured and the result is shown in the right diagram of Fig. 4.1. The assumed longitudinal density modulation is observed meanwhile the measured rms pulse length of 13.8 ps is more than twice the design value of 6 ps.

This result motivates a direct measurement of the longitudinal laser pulse profile, using the method of auto/cross-correlation introduced in Section 3.1. The auto-correlated signal of the

IR laser beam and the cross-correlated signal between IR and UV laser beams were measured as shown in Fig. 4.2 and fitted with Gaussian functions. According to Equation (3-1) and (3-2), the rms pulse lengths of the IR and UV laser are 11.5 ps and 8.6 ps respectively.

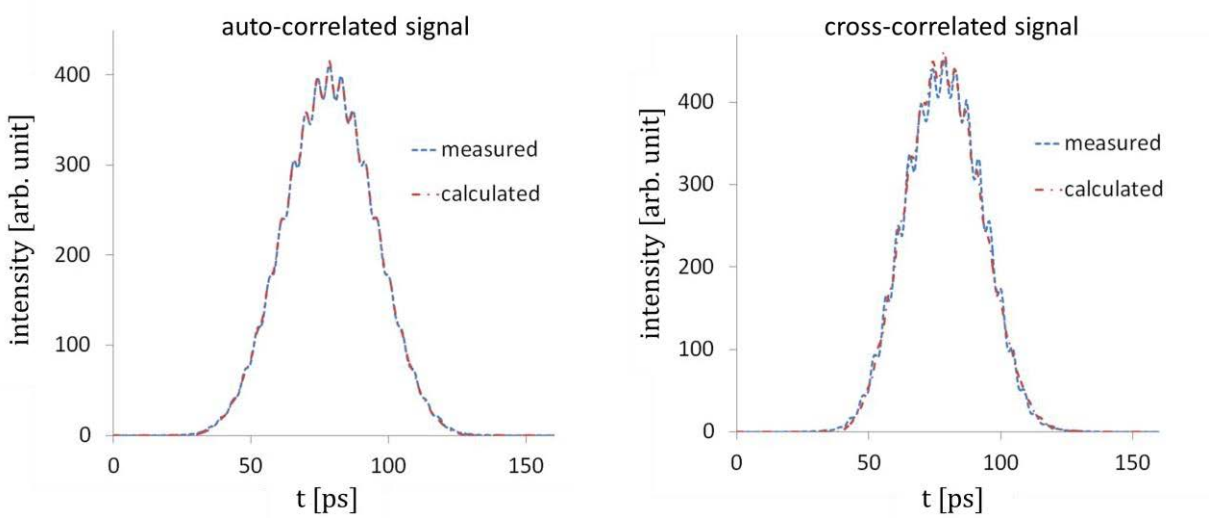

Fig. 4.2 Auto-correlated signal of the IR laser beam (left) and cross-correlated signal between IR and UV laser beams (right). The blue curves show the experimental data while the red curves are calculated from deconvolution signals, which will be explained in the following paragraphs in this section. From Gaussian fittings, the rms pulse lengths of the IR and UV laser are 11.5 ps and 8.6 ps respectively.

However, the Gaussian fitting does not provide any information about the modulation. Using the FFT based deconvolution described in Section 2.5.4, the profiles of both the IR beam and the UV beam were deconvolved and shown in Fig. 4.3. Calculated from the deconvolved profiles, the rms pulse length of IR laser is 11.2 ps and the pulse length of the UV laser is 8.3 ps, which are slightly smaller than those calculated from the Gaussian fitting. The modulation is now observed and the structure of the UV pulse agrees with the electron beam based measurement shown in Fig. 4.1. However, this direct measurement of the UV pulse length using cross-correlation is 50% lower than that of the electron-beam-based measurement.

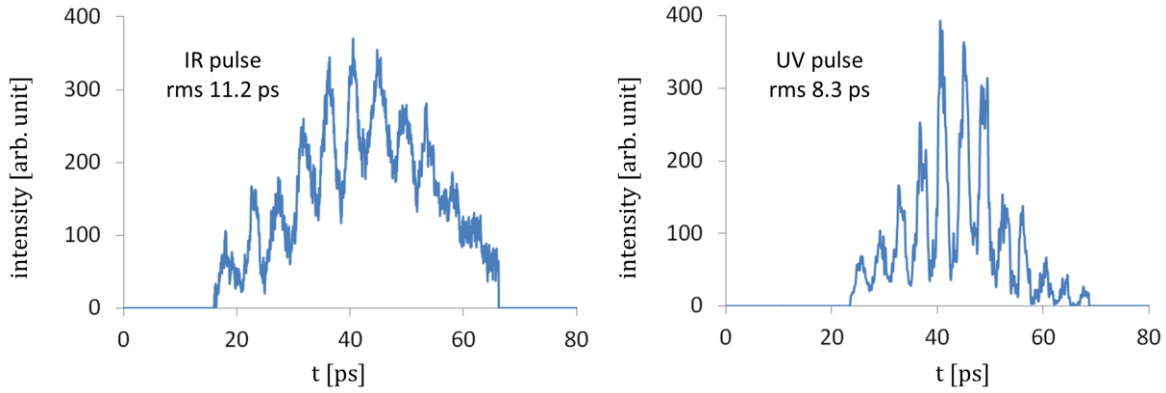

Fig. 4.3 Deconvolved IR pulse profile (left) and UV pulse profile (right).

Smoothing and interpolation have to be conducted to the measured correlation signals before deconvolution. The deconvolution is very sensitive to the accuracy of measurement results as well as to the parameters set for smoothing and interpolation. The deconvolved pulse distributions are further used to perform the convolution numerically and the result is compared with measurement, as an evaluation of the deconvolution. The results of the convolution based on the best solutions of deconvolution (shown in Fig. 4.3), are already presented in Fig. 4.2 with the red curves. It shows that the measured and calculated auto-correlated signals agree with each other very well. For the cross-correlation, however, there is relative larger difference between measurement and calculation. The reason is that the cross-correlated signal has a much weaker intensity therefore the SNR is smaller.

As both measurements indicate an undesired modulation in the longitudinal profile of the laser pulse, the laser system for ELBE SRF gun was improved and after that the longitudinal distribution of the laser pulse was recovered to a Gaussian distribution with the rms pulse length of 7 ps, which is also the value used throughout this thesis. Auto-correlated and cross-correlated signals measured for the improved laser system are shown in Fig. 4.4.

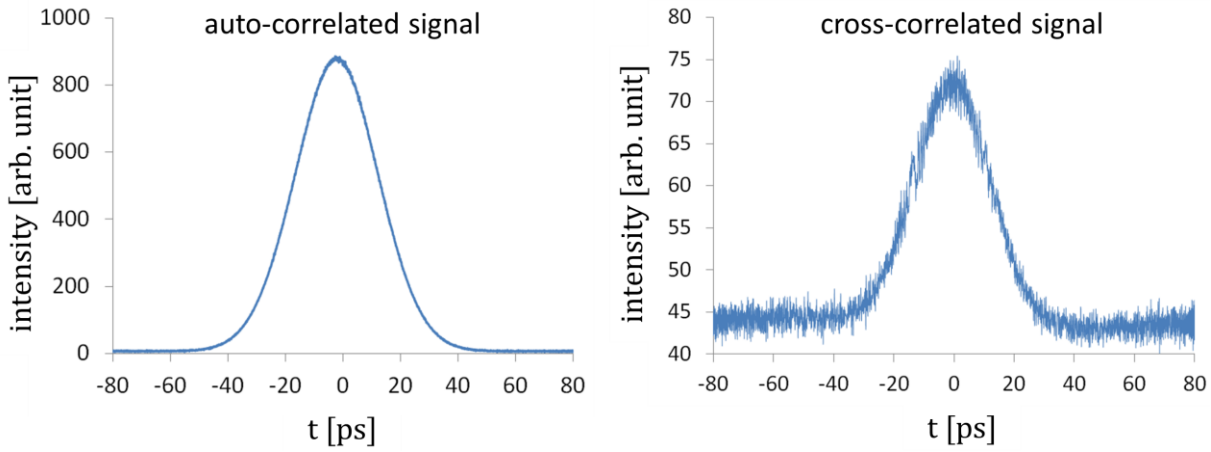

Fig. 4.4 Auto-correlated signal of the IR laser beam (left) and cross-correlated signal between IR and UV laser beams (right) after the improvement of the laser system. From Gaussian fittings, the rms pulse lengths of the IR and UV laser are 10.3 ps and 7.0 ps respectively.

This auto/cross-correlation based measurement for longitudinal laser pulse profile shows that the pulse length of the UV laser is about 70% of that of the IR laser. By design, the intensity of the UV beam is about 15% of that of the IR beam and the alignment of cross-correlation is more challenging. As a result, the SNR of cross-correlated signal is much smaller than that of the auto-correlated signal.

4.2. Commissioning of ELBE SRF Gun II with magnesium cathode

As described in Section 1.1.2, a contamination happened to the SRF cavity while changing the Cu cathode with a Cs_2Te cathode, reducing its performance. After that, as an alternative photocathode, a magnesium cathode was installed in the gun, aiming to generate electron bunches with a bunch charge of several hundreds of pC. This magnesium cathode has a laser-cleaned area of 4 mm in diameter and possessed a QE of 0.2%. For measurements in this section, the cathode position in operation was 1.4 mm and the laser was temporally Gaussian distributed with an rms pulse length of 7 ps.

4.2.1. Energy and energy spread measurement

Energy and energy spread were measured in the diagnostics beamline according to the method introduced in Section 3.2, at a gradient of 8 MV/m. The DC voltage was -5 keV, the bunch charge was 5 pC and the laser phase was scanned from 15° to 70°. For other laser phases the electron beam exceeds the measurement range of Screen 5. The laser spot was radially quasi-Gaussian distributed with the rms size of 0.23 mm. The SC solenoid was used to focus the beam at Screen 4. Measurement results are presented in Fig. 4.5, as well as results of simulations using the same parameters.

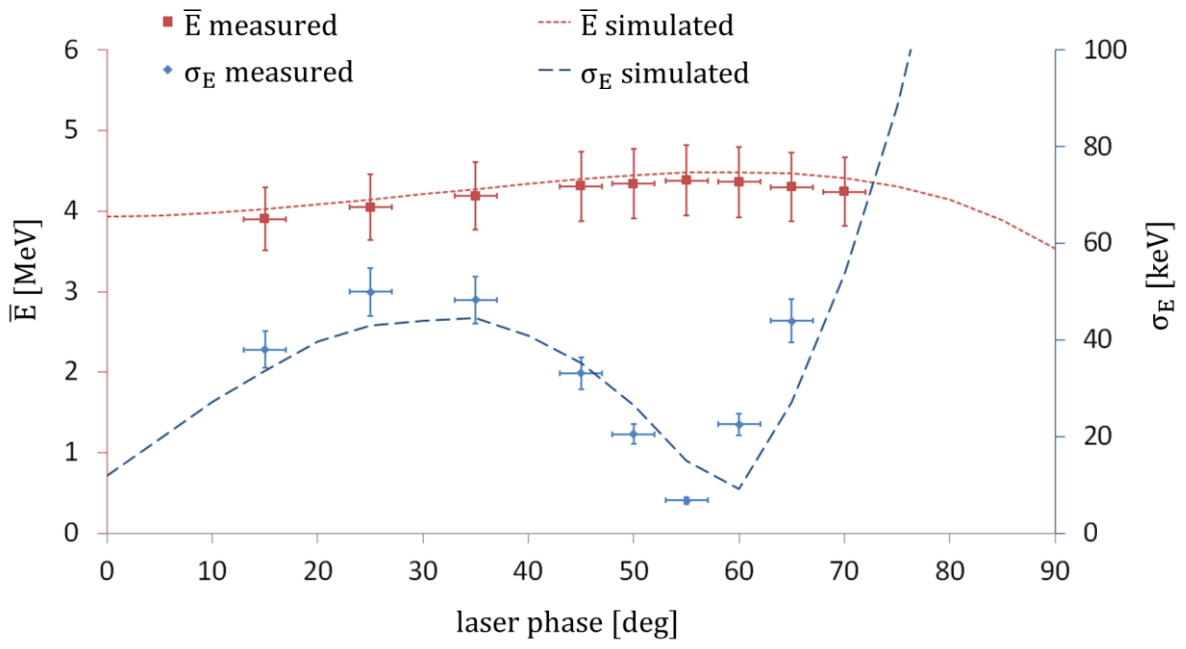

Fig. 4.5 Energy and energy spread measurement for ELBE SRF Gun II with a magnesium cathode. Relevant parameters of the SRF gun during measurement: gradient is 8MV/m, cathode position is 1.4 mm, laser pulse length is 7 ps and DC voltage is -5 keV.

In Fig. 4.5, the simulation shows a similar trend as the measurement. At the laser phase of about 55°, the energy reaches its maximum of 4.38 MeV while the energy spread has a minimum of 7 keV. For all measured laser phases, the energy varies by only less than 10%. However, the energy spread firstly increases to 40 keV, then decreases to its minimum, and finally increases strongly with the laser phase.

4.2.2. Dark current measurement

The dark current of an SRF gun refers to the current induced by the RF field, which can be emitted from the surface of both the cathode and the cavity because of field emission due to local field enhancement or a local decrease of the work function. As discussed in Section 1.3, the dark current should be kept as low as possible for pELBE, nELBE and CBS experiments.

In an experiment of changing the cathode position, a new field emitter appeared near the cathode and a significant increase of the dark current was observed. The energy spectrum of the dark current is shown in the left diagram of Fig. 4.6. It is observed that the dark current has a high-energy peak with the same energy as the desired electron beam, which cannot be eliminated by dipoles.

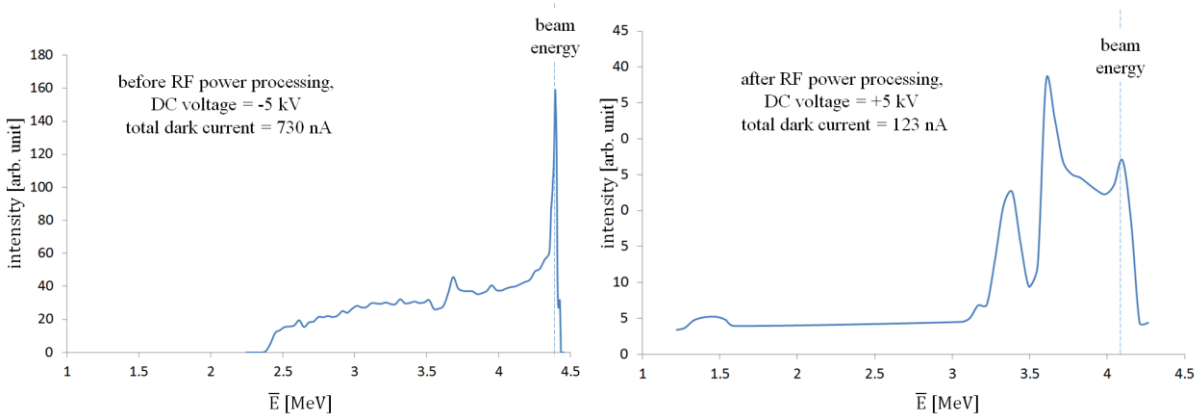

Fig. 4.6 The spectrum of dark current after the new field emitter was generated (left) and the spectrum of dark current after RF power processing. The DC voltage is negative in the left diagram and positive in the right diagram.

It was found that the increased dark current is sensitive to the polarity of the DC voltage. More dark current was produced with negative DC voltage. Therefore, positive DC voltage was applied and the dark current was reduced to a much lower level. Fig. 4.7 presents the measurement of dark current as a function of the gradient with different DC voltages, showing that in general the dark current increases with the gradient of the gun cavity and the positive DC voltage suppresses the dark current efficiently. Besides, RF power processing was

performed for the cavity but it could not reduce the total dark current. The spectrum of the dark current with +5 keV DC voltage after the RF power processing is shown in the right diagram of Fig. 4.6. Compared to the left diagram, which was measured with negative DC voltage, not only the total dark current is reduced to 17%, but the fraction of the high-energy peak is also remarkably reduced.

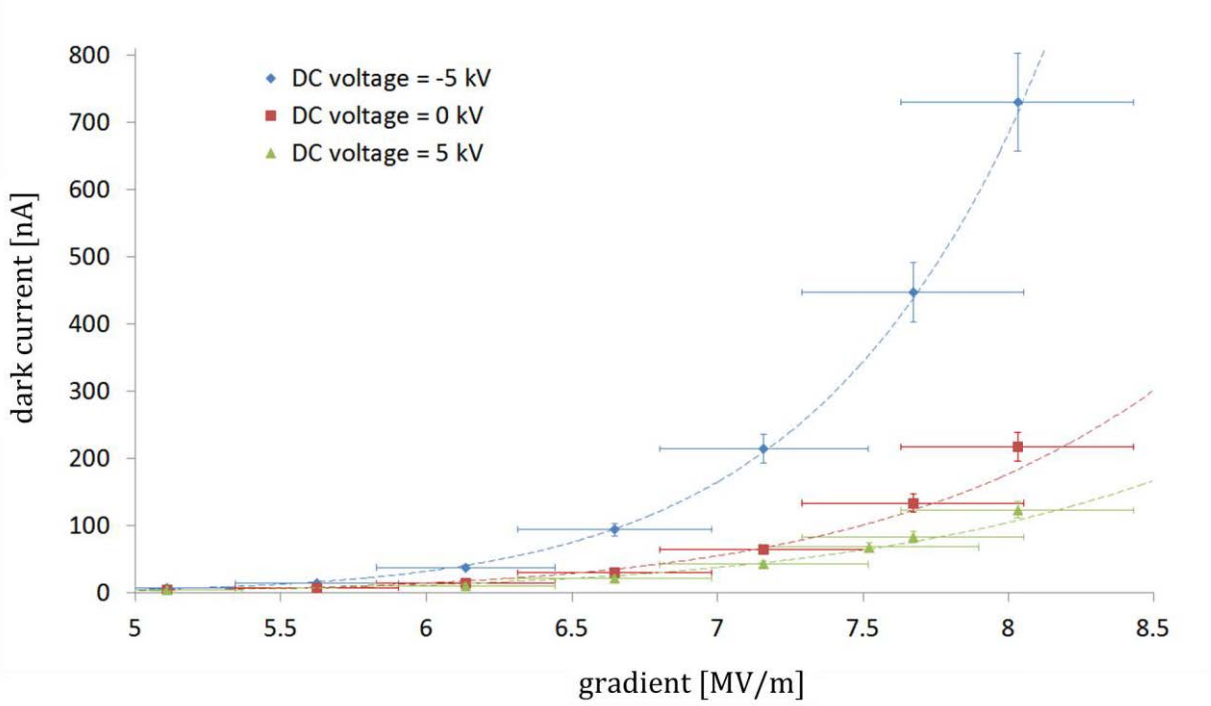

Fig. 4.7 The relation between dark current and gradient of ELBE SRF Gun II with different DC voltages. Dashed lines are quadratic polynomial fittings of measured data. All measurements are done with the cathode position of 1.4 mm.

4.2.3. Emittance versus DC voltage

A negative DC voltage is supposed to provide an extra acceleration for the initial electron bunch and therefore it had always been applied until the accident in which the new field emitter was formed during the cathode moving. However, according to Section 4.2.2, a positive DC voltage has to be applied to reduce the dark current of the gun. It is interesting to investigate how the DC voltage influences the beam quality, therefore, a measurement of the transverse emittance for different bunch charges was conducted with and without the positive DC voltage. Results are contrary to the initial expectation: the emittance is actually smaller with a positive DC voltage, as shown in Fig. 4.8. In this measurement the gradient was set to 8 MV/m and the laser phase was 50°. An aperture with a diameter of 0.5 mm was installed to cut the laser spot to a quasi-flattop distribution. The laser spot on the cathode has an rms size of 0.25 mm.

This measurement enlightened the simulation work in Section 2.7.1. It is shown in simulation that a positive DC voltage leads to longer bunches. The charge density is lower in longer bunches which can result in smaller emittance. This explanation is supported by Fig. 4.8, where the difference of emittance becomes larger between cases with and without the positive DC voltage with higher bunch charges.

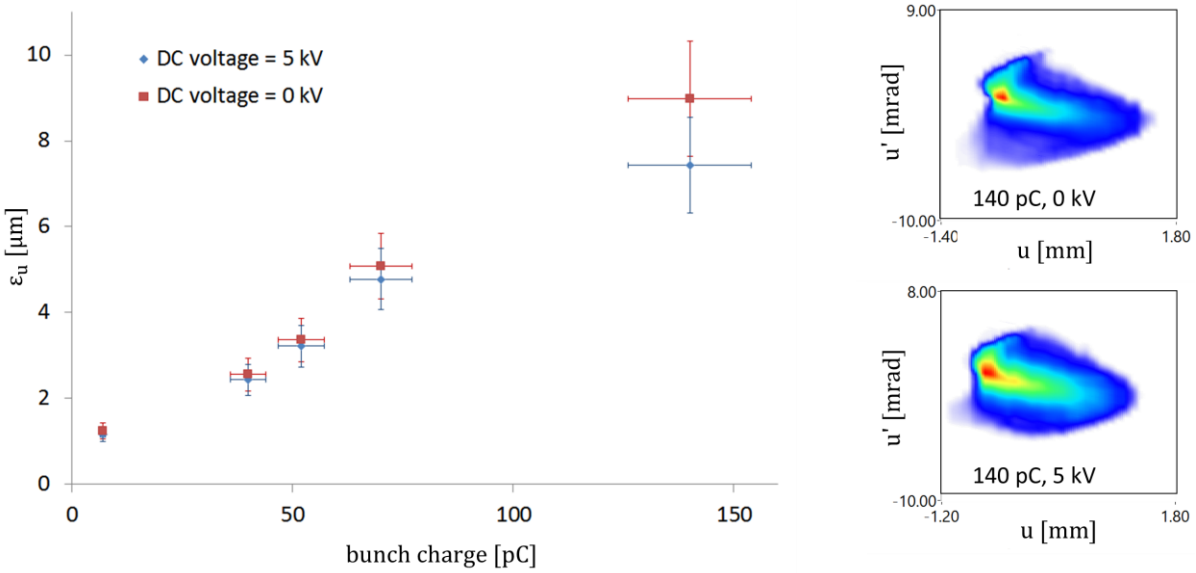

Fig. 4.8 Transverse emittance measured for different bunch charges with/without the DC Voltage. In general, a positive DC voltage leads to smaller emittance. Phase spaces for 140 pC bunches with/without the positive DC voltage are illustrated on the right. Relevant parameters of the SRF gun during measurement: gradient is 8 MV/m; laser phase is 50°; beam energy is 4.36 MeV; cathode position is 1.4 mm; laser pulse length is 7 ps; laser spot size is 0.25 mm.

4.2.4. Impact of laser spot size

The transverse distribution of the UV laser used for the ELBE SRF gun has to be optimized for each operation mode depending on the bunch charge. Theoretically, a large laser spot reduces the space charge effect but increases the thermal emittance. The balance of these two aspects depends on the bunch charge, which is supported by the simulation study in Section 2.7.2.

An aperture with a diameter of 0.5 mm was used to select a round, quasi-Gaussian distributed laser spot for the commissioning of ELBE SRF Gun II with the magnesium cathode. In general, the selected laser spot will be imaged on the cathode with a designed amplification factor of 2.5 (measured to be 2.4). To study the influence of laser spot size on the quality of the beam, another two apertures with diameters of 1 mm and 1.5 mm were applied as a replacement of the 0.5 mm aperture. In addition, a defocusing lens and a focusing

lens were installed sequentially in front of the aperture to enlarge the beam size and hence to change the distribution of the laser spot. These two lenses were applied for the 1 mm aperture and 1.5 mm aperture.

For the four experimental series with 0.5 mm aperture, 1mm aperture, 1 mm aperture with lenses and 1.5 mm aperture with lenses, the vertical emittance was measured with slit-scan method at Screen 2 in the diagnostics beamline for different bunch charges. The FWHM laser spot sizes for the four series were 0.68 mm, 1.33 mm, 1.42 mm and 1.68 mm respectively. For these measurements, the gradient of the gun was 7.16 MV/m, the laser phase was 50° and the DC voltage was +5 keV. The measurement results are shown in Fig. 4.9 and compared to simulation results presented with solid lines. Generally, the measurement results have the same trend, but are larger than the simulation results.

The simulation was performed for the beam transport from the cathode to Screen 2 with the simulation tool described in Section 2.6. The thermal emittance was calculated by ASTRA according to Reference [60], where it is mentioned that in general the experimental thermal emittance measured in an RF photocathode gun is about a factor of 2 times the theoretical thermal emittance. One of the reasons for this difference is supposed to be the surface roughness of metal cathodes which has not been taken into account in the theory. In Fig. 4.9 the total emittance from simulation partially consists of the underestimated thermal emittance.

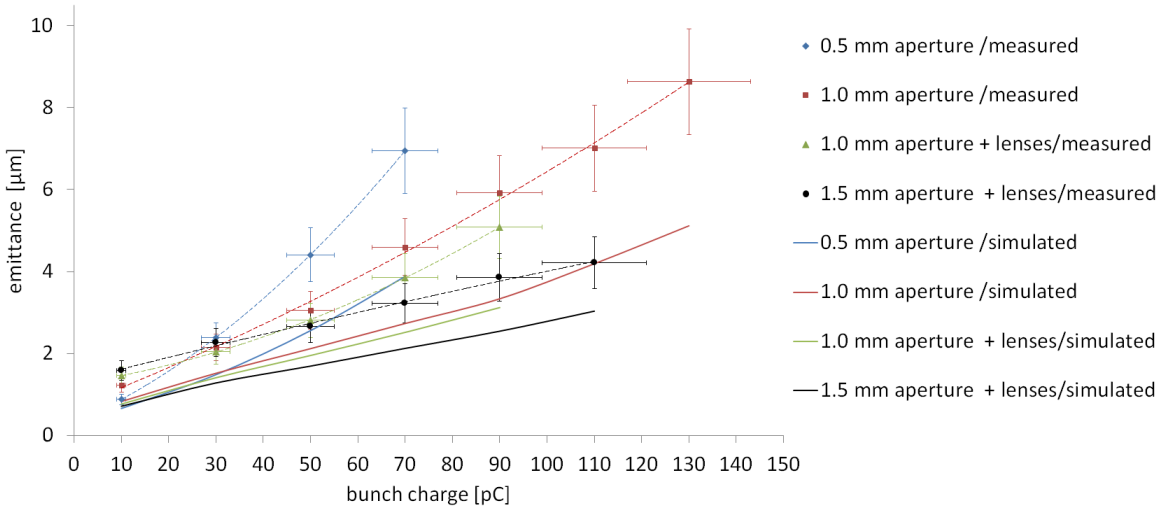

Fig. 4.9 Measured and simulated emittance vs. bunch charge for different laser distributions. Dashed lines are quadratic polynomial fittings of the measured data. Relevant parameters of the SRF gun during measurement: gradient is 7.16 MV/m; laser phase is 50°; beam energy is 3.9MeV; cathode position is 1.4 mm; DC voltage is 5 keV; laser pulse length is 7 ps.

As a general trend, for bunch charges below 25 pC, the thermal emittance dominates the total emittance, and hence, smaller laser spot sizes lead to lower emittance. For bunch charges

higher than 30 pC, space-charge-induced emittance contributes the most to the total emittance and thus larger laser spot sizes result in lower emittance. The distributions of laser spots for these four experimental series are shown in Fig. 4.10, together with the corresponding phase space distributions for beams with bunch charges of 10 pC and 70 pC.

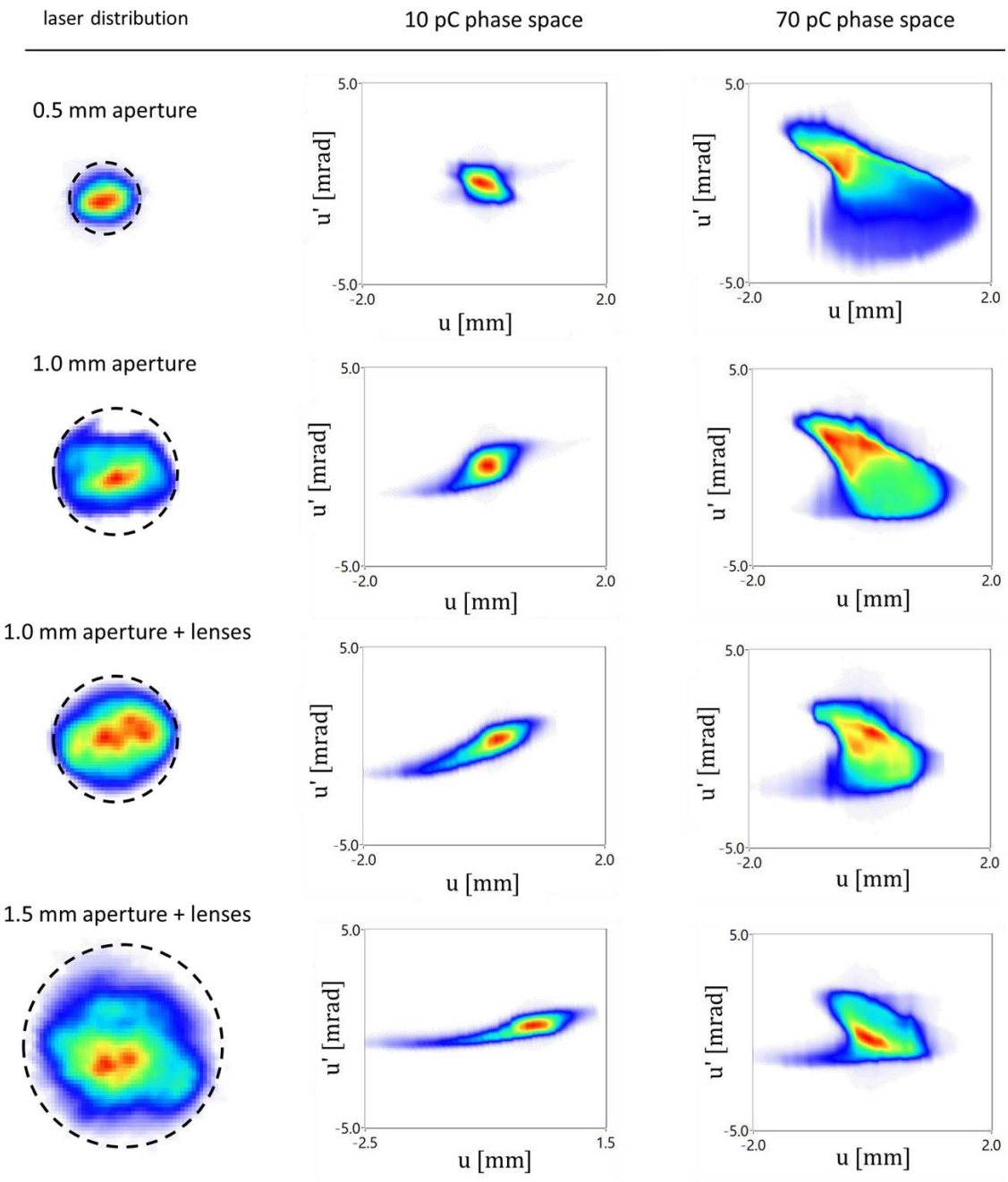

Fig. 4.10 Laser spot distributions and phase space distributions for beams with the bunch charge of 10 pC and 70 pC. From top to bottom, the four laser spots are selected by a 0.5 mm aperture, a 1.0 mm aperture, a 1.0 mm aperture & two lenses and a 1.5 mm aperture & two lenses. The FWHM laser spot sizes for the four groups are 0.68 mm, 1.33 mm, 1.42 mm and 1.68 mm respectively. The phase space is enlarged by the size of laser spot for the bunch charge of 10 pC. But for the bunch charge of 70 pC, the phase space shrinks with laser spot size. The relevant parameters of the SRF gun during measurement: gradient is 7.16 MV/m; laser phase is 50°; beam

energy is 3.9 MeV; cathode position is 1.4 mm; DC voltage is 5 keV; laser pulse length is 7 ps; the current of the SC solenoid is 3.65 A.

Although Fig. 4.9 shows that the emittance always increases with bunch charge, Fig. 4.10 gives an example in the experimental series of "1.5 mm aperture with lenses" where the beam size can be larger for lower bunch charges at Screen 2. To investigate the reason, measured beam sizes for all experimental groups are shown in Fig. 4.11. Most of the measured beam sizes are up to 30% larger than simulations. However, both measurements and simulations indicate similar trends for all experimental groups. The beam size profile given by Elegant reveals the reason, which is exemplified in Fig. 4.12. With the same solenoid strength, a beam with lower bunch charge has a smaller beam size and a smaller divergence at the SC solenoid, which is equivalent to a smaller objective distance if the solenoid is considered as a lens. Therefore, the beam waist is closer to the solenoid, which later leads to a diverging beam at Screen 2 with a larger size than that of the beam with a higher bunch charge.

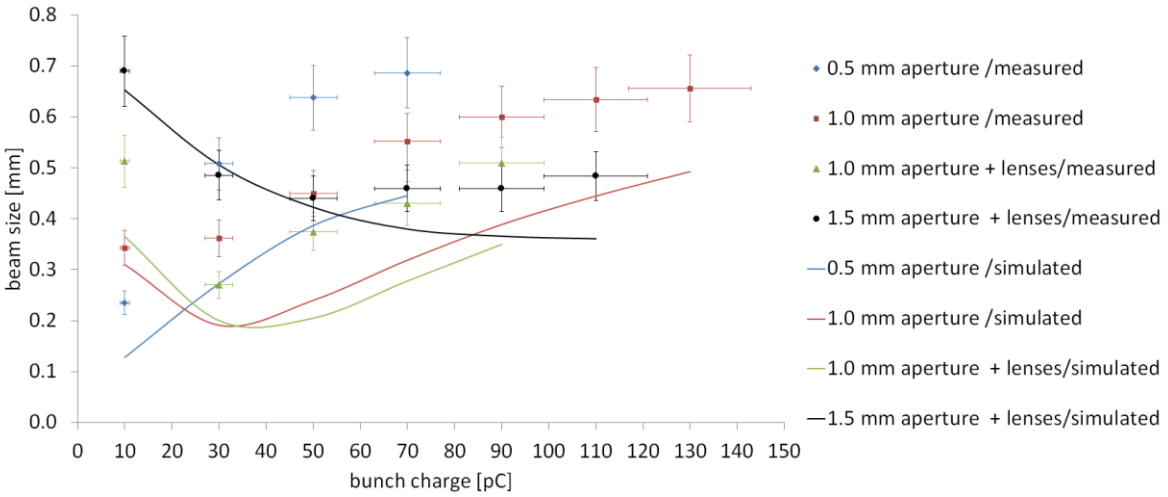

Fig. 4.11 Measured and simulated beam size vs. bunch charge for difference laser distributions. The bunch size at Screen 2 can be larger for lower bunch charges. The reason is explained in Fig. 4.12. Relevant parameters of the SRF gun during measurement: gradient is 7.16 MV/m; laser phase is 50°; beam energy is 3.9MeV; cathode position is 1.4 mm; DC voltage is 5 keV; laser pulse length is 7 ps.

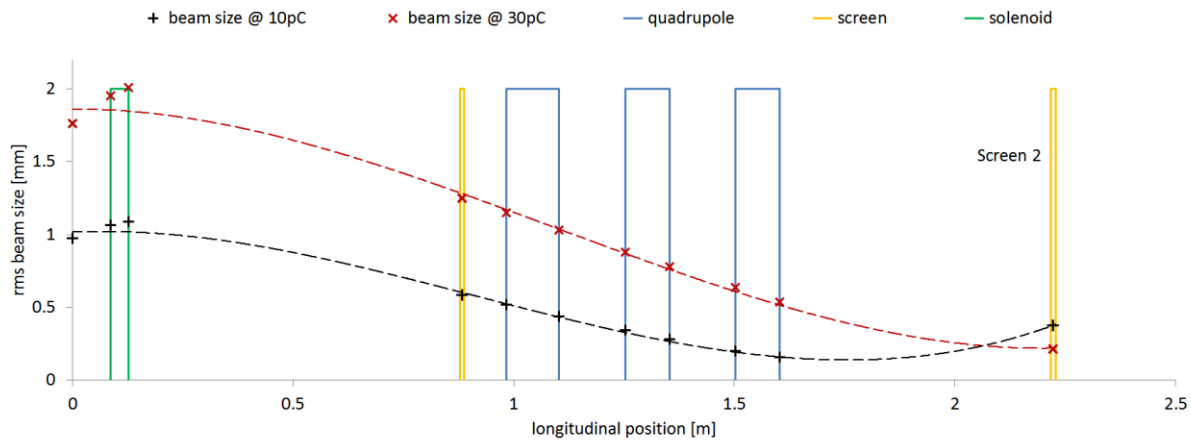

Fig. 4.12 The beam size profile given by Elegant from the exit of gun-cavity to Screen 2, for 10 pC and 30 pC bunches in the experimental group with 1.0 mm aperture and lenses. At Screen 2, the beam size for 10 pC is larger than that for 30 pC.

4.3. Longitudinal space charge experiments at PITZ

According to simulations in Section 2.5.3 and 2.8, the longitudinal space charge (LSC) effect plays an important role in the transport of beams with the energy from several MeV to several tens of MeV. To verify this effect, a relevant experiment has been conducted at institute PITZ.

The PITZ beamline and the experimental conditions are shown in Fig. 4.13. In this experiment, the applied bunch charge was 1 nC. Electron bunches were generated from an NCRF gun with an energy of 6.04 MeV, and then accelerated by a booster to the energy of 21.4 MeV. The RF phase of the gun was chosen for minimum energy spread, which is negligible compared to the energy spread after the booster.

Two quadrupoles right after the booster cavity were used to focus the beam, with its waist controlled in the middle of the two downstream dispersive sections, named of HEDA 1 and HEDA 2, respectively.

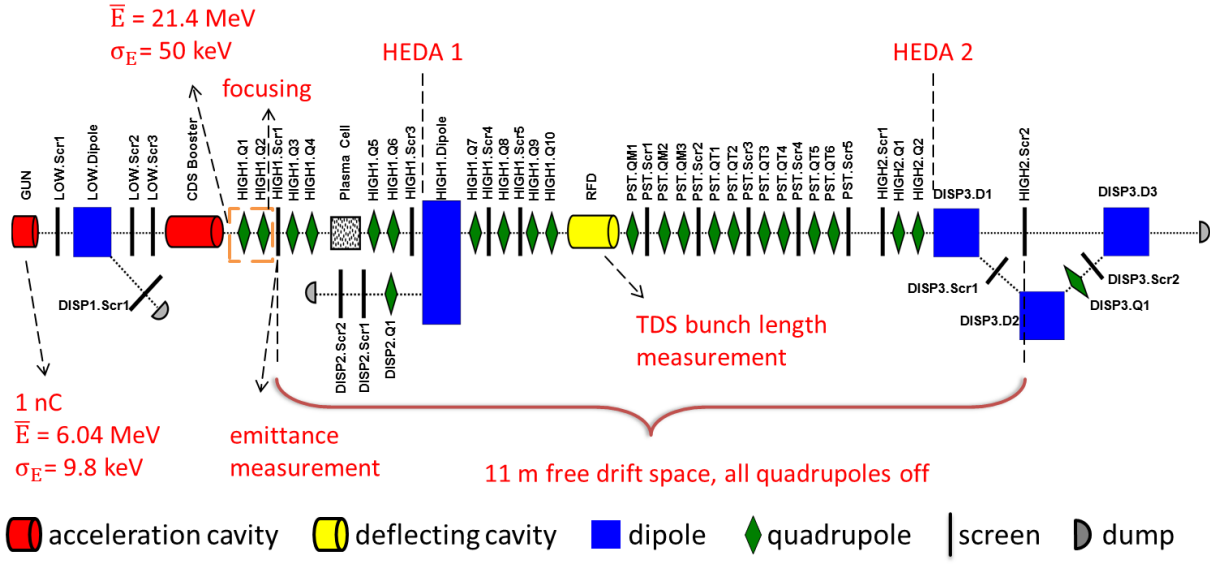

Fig. 4.13 The PITZ beamline and the experimental conditions.

The beamline section for studying the LSC effect starts from the screen HIGH1.Scr1, where a slit scan emittance measurement [80] was performed. Results are shown in Fig. 4.14 with the horizontal emittance of 4.65 µm and the vertical emittance of 2.21 µm. In the following beam transport for 11 m, all quadrupoles were turned off. The mentioned two dispersive sections, HEDA 1 and HEDA 2, were used to measure the energy and energy spread. Between them, a Transverse Deflecting Structure (TDS) based bunch length measurement [81] was performed and the rms bunch length was measured to be 6 ps, as

shown in Fig. 4.15. The beamline from HEDA 1 to HEDA 2 is a free drift distance neglecting the steerers with low magnetic fields. The beam size along the beamline is shown in Fig. 4.16.

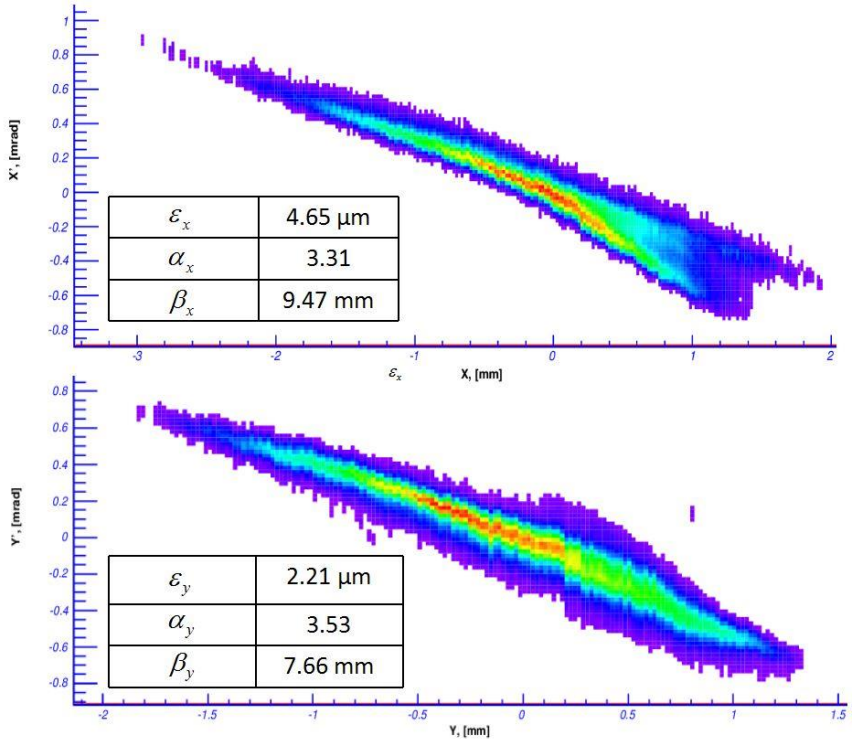

Fig. 4.14 Transverse emittance measurement at PITZ for a 1 nC, 21.4 MeV beam.

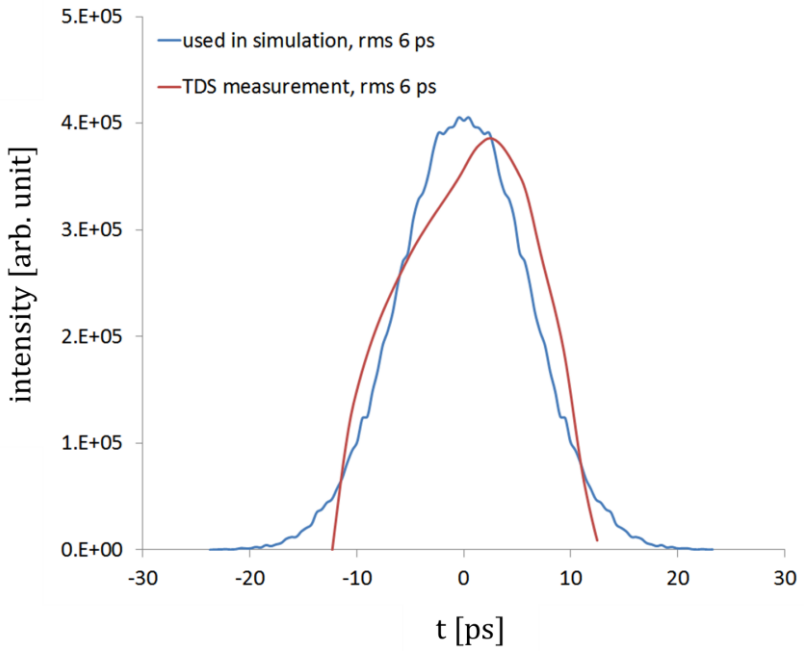

Fig. 4.15 TDS measurement of bunch length at PITZ and the Gaussian bunch distribution used in simulation with the same rms bunch length of 6 ps.

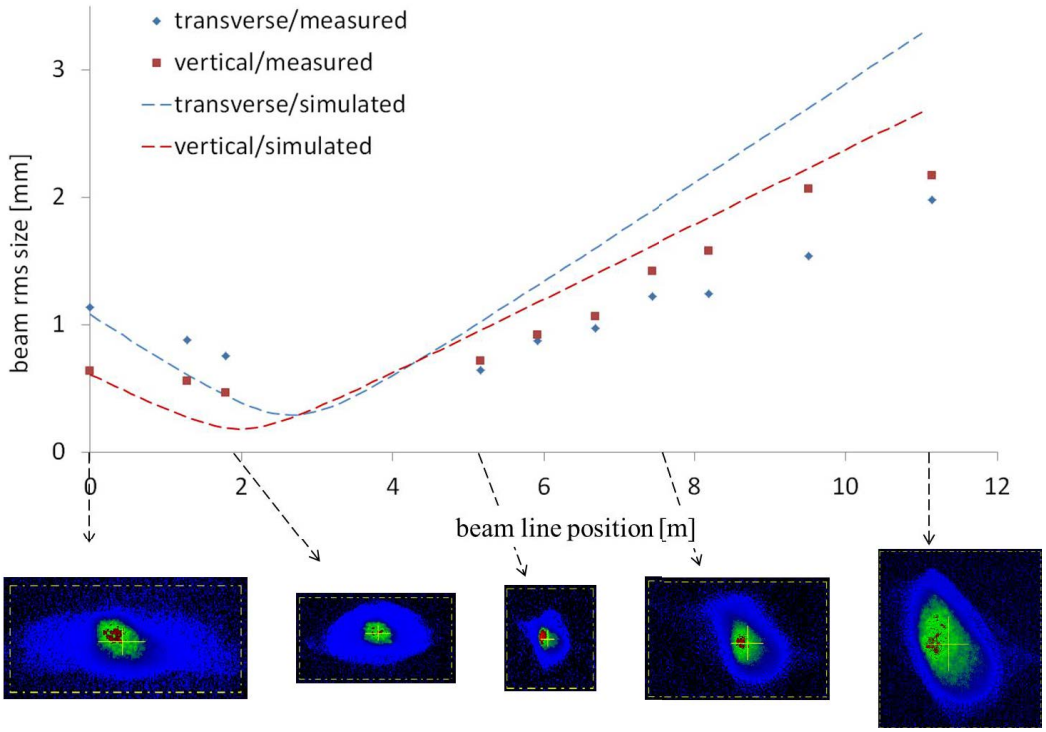

Fig. 4.16 Measurement and simulation of transverse beam size at PITZ.

The LSC effect is quantified by the change in energy spread. The energy and energy spread were measured at both ends of the free drift space while the phase of the booster cavity was scanned, as shown in Fig. 4.17. The energy measured at HEDA 2 is 1% lower than that measured at HEDA 1, which might be caused by the calibration error of dipoles. However, even if there is a systematic error, the relationship between energy and booster phase is not influenced. Both measurements show that the crest phase of the booster for the maximum energy gain is -84°. The booster phase for minimum energy spread is also -84° measured at HEDA 1 but it shifted to -79° in the measurement at HEDA 2. In addition, for all phases, a variation of energy spread is observed which is much larger than the assumed systematic error of 1% from the energy measurement.

Booster phases lower than the crest phase provide a positive chirp and higher phases provide a negative chirp. The variation of energy spread can be explained by the general influence of the LSC effect that the head of the bunch gains energy and the tale loses energy. In positively/negatively chirped beams the LSC effect enlarges/reduces the energy spread of the bunch.

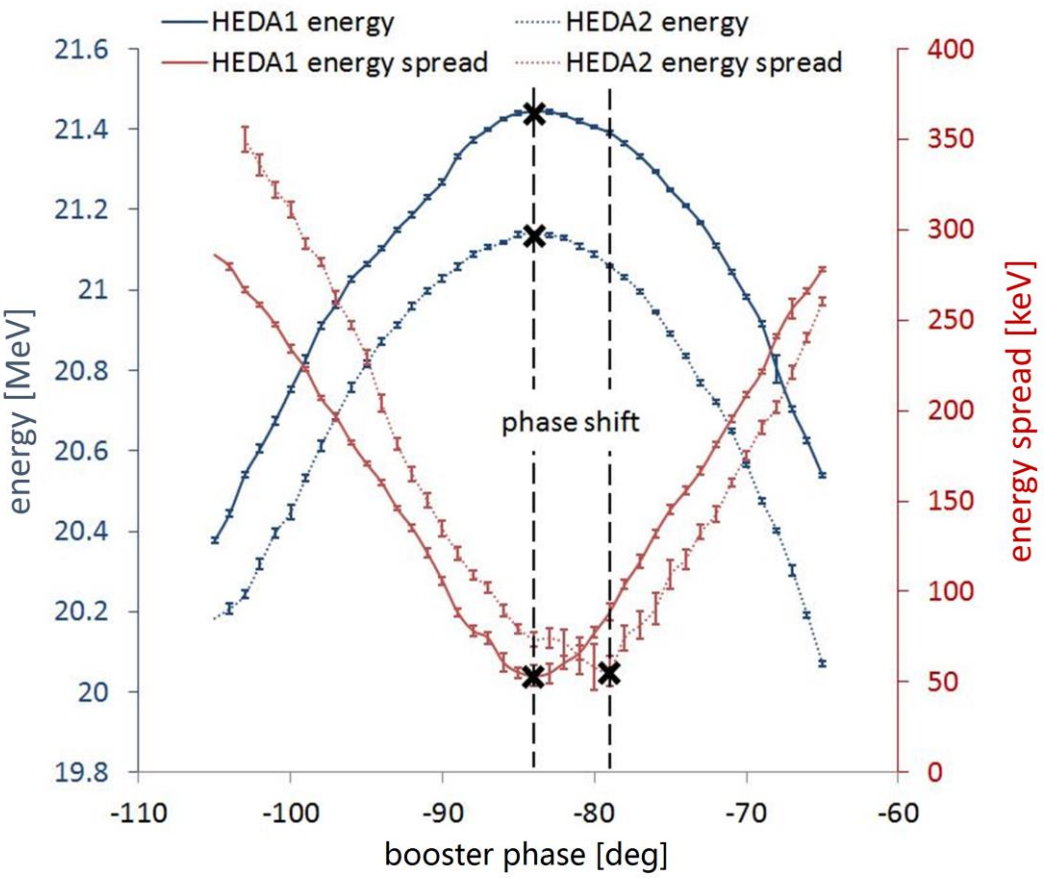

Fig. 4.17 Energy and energy spread measurements at dispersive sections of the PITZ beamline.

This experiment aimed to verify the strong LSC effect in Elegant simulations. A simulation was performed for a simple free drift space, where the energy change of particles only came from the LSC effect. The incoming beam was initialized as 3D Gaussian distributed using the above measured parameters of emittance, Twiss parameters and bunch length. The simulated transverse beam size is shown in Fig. 4.16.

In simulation, the rms bunch length is set to 6 ps, which is the same as TDS measurement results. The applied longitudinal bunch distribution is shown in Fig. 4.15. The energy and energy spread measured in HEDA 1 is set for the initial beam. After the drift distance, the simulated energy spread is compared with measurement at HEDA 2, as shown in Fig. 4.18. The variation of simulated energy spread is about 50% smaller than that of measurements, which is sensitive to the bunch length. By applying smaller bunch lengths, stronger LSC effect was observed in simulation. The results with 4 ps bunch length match the experiments the best.

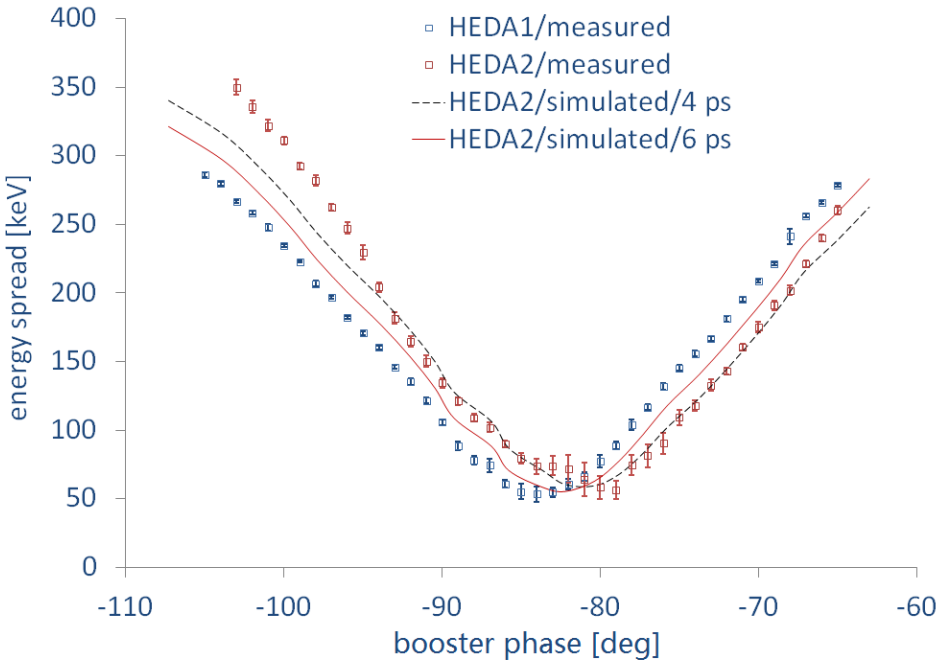

Fig. 4.18 Simulation results of the energy spread variations at different bunch lengths, compared with experiments. Error bars in this figure include only statistical errors. It is shown that the LSC effect is weaker in simulation than in actual measurements. The impact of the LSC effect in the simulations of Section 2.5.3 and 2.8 is not over-discussed.

As a summary of the experiments at PITZ, the impact of the LSC effect was studied by measuring the energy spread variation in a free drift space. The variation has also been simulated based on the measured parameters of the incident beam. The influence of the LSC effect on a 21 MeV/1 nC electron beam was confirmed by observing the shift of the minimum-energy-spread phase of the booster measured at both ends of a free drift distance. The influence from experiments is twice of that from simulations. The difference may come from the error of the energy spread measurement, the error of the TDS bunch length measurement or the error of initializing the electron bunch with the Gaussian distribution in simulations. Adequate attention on the LSC effect should be paid to future beam transport in the ELBE accelerator.

4.4. 200 pC beam transport in ELBE beamline

This section presents a beam transport experiment in which a high-bunch-charge beam was transported from ELBE SRF Gun II to the Browne-Buechner spectrometer. The beamline is shown in Fig. 2.17. This beam transport experiment was designed to verify that the high-bunch-charge beam generated by the SRF gun can be transported in the ELBE beamline without critical beam loss. In addition, experimental results were also used to evaluate the simulation tool introduced in Section 2.6.

During the high bunch charge operation, a diagnostic mode of operation was applied to protect the ELBE beamline, which only allowed the SRF gun to inject a beam with an average current below 10 μA. For that reason, a mechanical shutter was applied to modulate the laser beam into macro pulses of 40 ms out of every 100 ms, reducing the average current while keeping the same bunch charge of 200 pC. The gradient of the gun was 7.5 MV/m, the laser phase was adjusted to minimize the energy spread, the cathode position was 1.4 mm, the DC voltage was +5 keV, the laser pulse length was 7 ps, and the laser spot size was 0.64 mm horizontally and 0.69 mm vertically.

The location of each measurement is shown in Fig. 4.19: The bunch charge was measured by the Faraday cup in the diagnostics beamline (shown in Fig. 3.4) and an Integrating Current Transformer (ICT) after Linac 1. The energy and energy spread were measured by dipoles after both Linacs as well as by the energy spectrometer. The beam size was measured along the beamline on Yttrium Aluminium Garnet (YAG) screens or Optical Transition Radiation (OTR) screens using Charge-Coupled Device (CCD). The emittance of the SRF gun and the distribution in vertical phase space were measured with slit-scan method in the diagnostics beamline. In addition, quadrupole-scan emittance measurements were performed in the dogleg, after Linac 1, after Linac 2 and right before the energy spectrometer. Finally, slice emittance and bunch length were measured by quasi-linearly chirping the beam using Linac 2.

A simulation of this experiment is also presented in this section. Most parameters in the simulation are the same as experimental parameters except for the laser spot distribution and the gradient of cavities: The laser is transversely imitated using a 2D Gaussian distribution with the rms spot size of 0.65 mm. The cavity gradients of both linacs are adjusted according to the measured energy at the crest phases of all cavities. The simulation is meaningful to analyze the measurement results, and optimized parameters in the simulation can be used as initial setting of experiment. Parameters used in this simulation can be found in Appendix III.

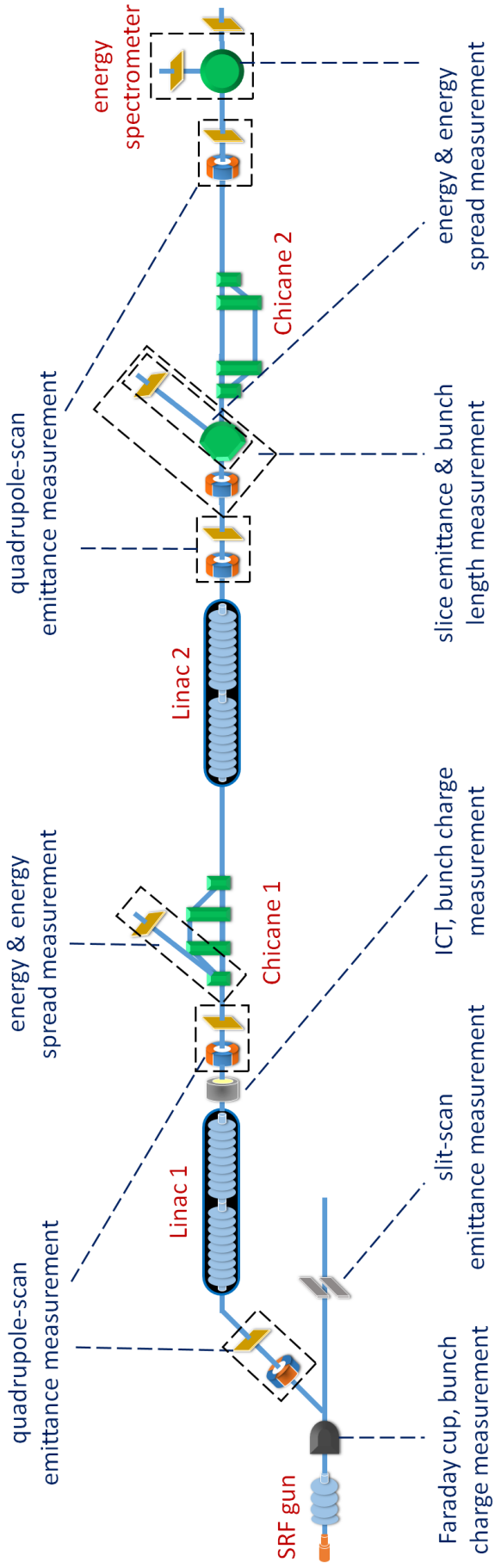

Fig. 4.19 Indications of measurements presented in this section. Beam loss monitors are installed along the entire beamline, which are not shown in this figure.

4.4.1. Bunch charge and beam loss measurement

For this experiment, the bunch charge measured at the Faraday cup was 185 pC with a 10% error. After the dogleg and Linac 1, which are the most critical sections for beam loss (according to simulations in Section 2.8), the bunch charge measured by an ICT was 200 pC with an error of 1%.

After Linac 1 and the ICT, the beamline is straight and the beam transport is less challenging. Optimizing the beam transport, the signals of all beam loss monitors were minimized to a negligible level with respect to the beam cutoff threshold. Based on the measurement of the Faraday cup, the ICT and the beam loss monitors, the bunch charge transported to the energy spectrometer was about 200pC.

4.4.2. Energy and energy spread measurement

Each of the Linacs at ELBE includes two cavities. These four cavities are named as Cavity 1, 2, 3 and 4 sequentially along the beamline. From Cavity 1 to Cavity 4, the gradient was set to 10 MV/m, 7 MV/m, 6 MV/m and 6 MV/m respectively. The length of each cavity is approximately 1 m. The energy and energy spread after Linac 1 were measured using the first dipole of Chicane 1, with different phases of Cavity 2 (shown in Fig. 4.20). Using a dipole after Linac 2, energy and energy spread were measured with Cavity 1 and 2 at their crest phases, while the phases of Cavity 3 and 4 were scanned simultaneously, as shown in Fig. 4.21.

In both measurements, the error of the measured energy was estimated to be 1% due to the alignment error of the beam, while the calibration errors of the dipoles were not included. A 10% error for the measured energy spread was estimated from the size calculation of the dispersed beam. The contribution of the horizontal beam size ($\sigma_{x,04}$ in Equation (3-4)) was not corrected but included in the error estimation.

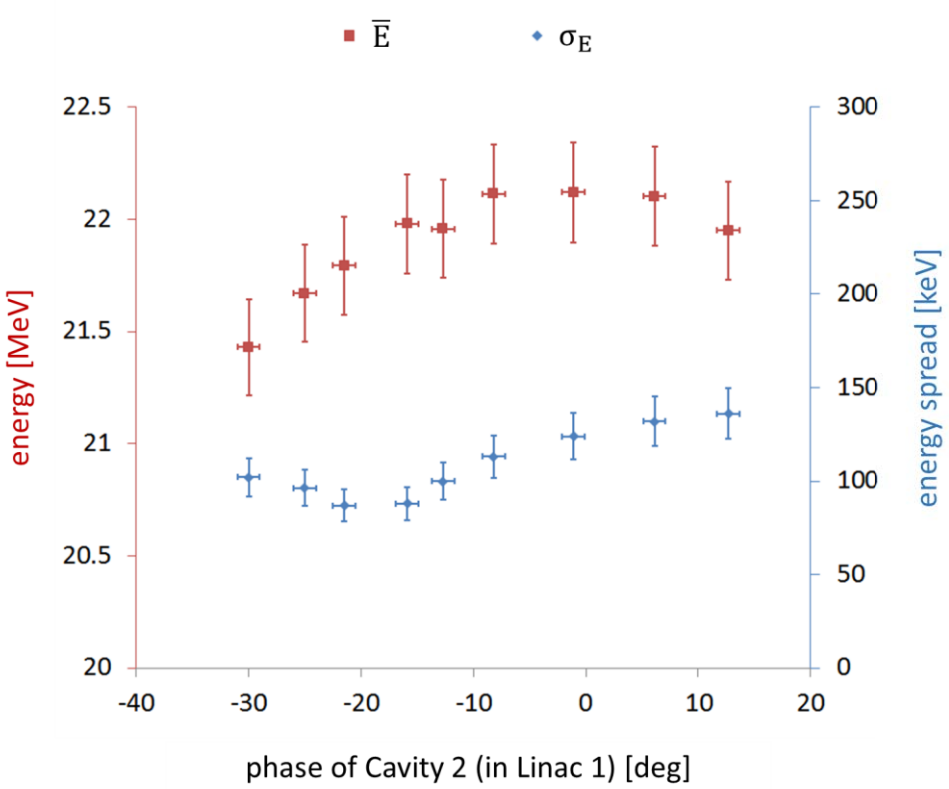

Fig. 4.20 Energy and Energy spread measurements after Linac 1.

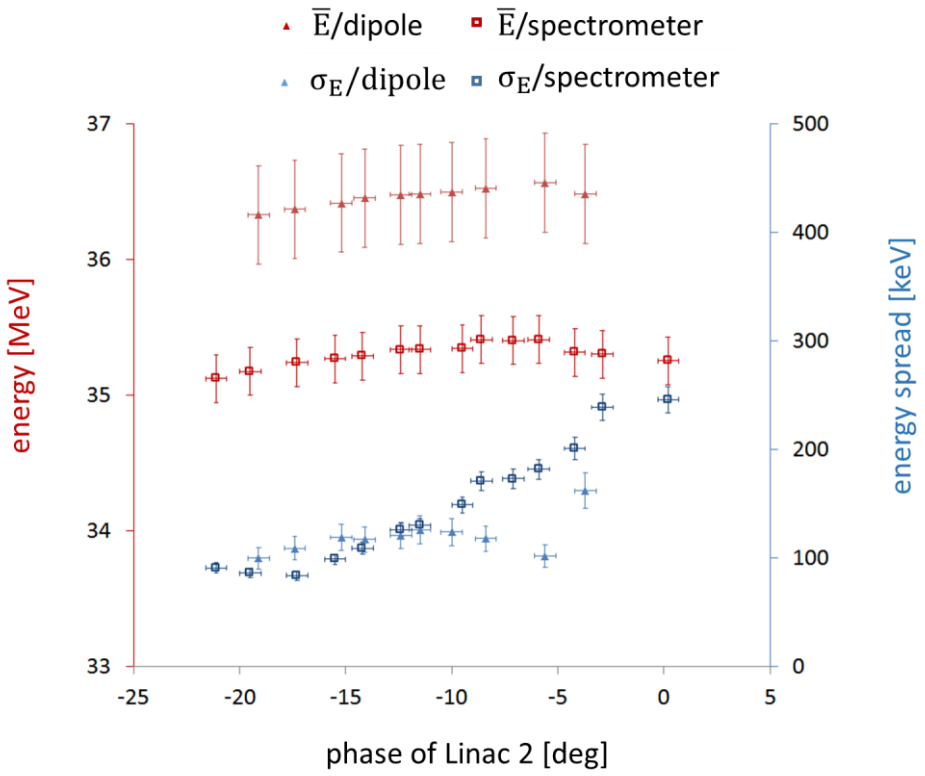

Fig. 4.21 Energy and energy spread measured at a dipole after Linac 2 and at at the Browne-Buechner spectrometer.

At the end of the beam transport, energy and energy spread were measured using the Browne-Buechner spectrometer introduced in Section 3.2. Results are also presented in Fig. 4.21. This spectrometer was designed specifically for energy and energy spread measurement. The CCD camera has less noise and the beam size contribution is corrected by selecting the beam with a narrow slit and imaging the selected beamlet on a screen. With all cavities set to their crest phases, the final beam energy was 35.4 MeV and the energy spread was 182 keV.

As shown in Fig. 4.21, in general the energy measured with the spectrometer is about 1 MeV lower than that measured with the dipole right after Linac 2. The trend of the energy spread measured by the spectrometer is more reasonable, that the energy spread is monotonic after the minimum point. The discrepancy of energy from the two measurements is due to the calibration error of the dipole, which is beyond the scope of this thesis.

4.4.3. Transverse beam size measurement

In order to get the beam position information and the transverse size, movable YAG or OTR screens are installed in screen-stations along the beamline. With a small macro-pulse duration of 5 ms in 10 Hz, screens can be inserted into the beam path without initiating a beam cutoff by the beam loss monitor system. The screens at ELBE are installed with a 45° angle. The beam generates visible light on screens, which is then reflected to a CCD camera. The image of the light includes the information of the beam size. With the fluctuation of the beam and the dynamic range of screens considered, the error of beam size measurement in this experiment was estimated to be 10%.

Measured beam sizes at different positions are presented in Fig. 4.22. The measurement results are compared with the simulation results. The difference between both sides accumulates with the transport distance. As a result, the simulated vertical beam size increases to a maximum of 16.7 mm, which is meaningless to be shown thus not covered by the scale of Fig. 4.20. It was found that from the screen denoted as “mismatch start”, the mismatch between simulated and measured beam distribution started to enlarge rapidly. As an improvement for the simulation, the last quadrupole before this screen (named LA1_MQ05 at ELBE) was corrected from -1.89 A to -2.05 A. In the new simulation, it is obvious that the beam envelope is very sensitive to parameter variation: by correcting the strength of only one quadrupole by 8.5%, the vertical beam size after this quadrupole stays below 3.5 mm. In this case, simulated and measured beam sizes have similar values. At locations denoted by lower-

case letters in Fig. 4.22, the measured transverse distributions of the beam are compared with corrected simulation results, as shown in Fig. 4.23.

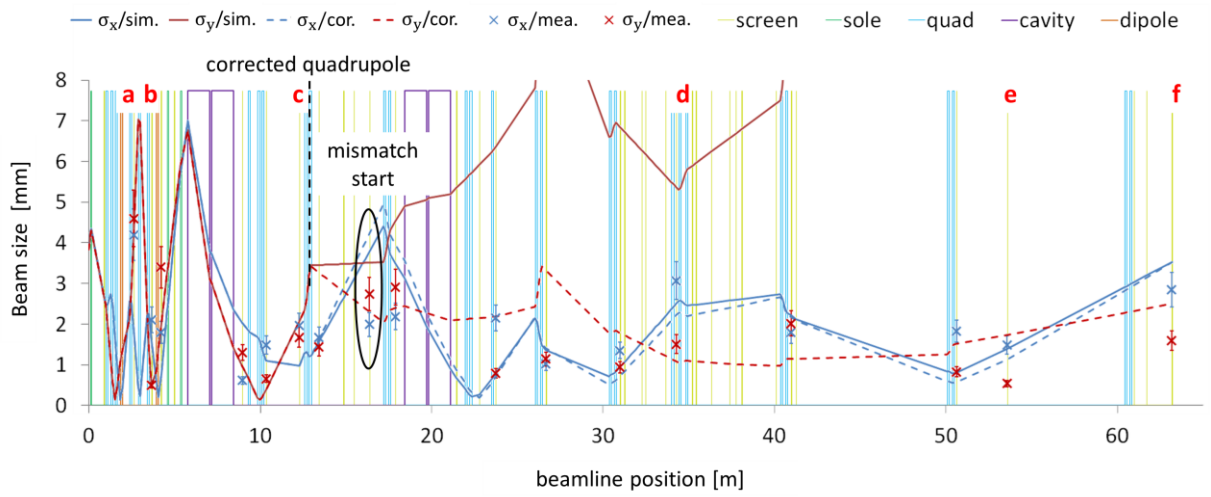

Fig. 4.22 Measured and simulated beam size profiles along the beamline for a 200 pC beam. The simulated vertical rms beam size evaluates to the maximum of 16.7 mm which exceeds the scale of this graph. Dashed lines represent a second simulation with the intensity of only one quadrupole corrected by 8.5%. The simulation is very sensitive such that the corrected vertical beam size stays below 3.5 mm after this dipole, which also agrees with measurements. At location marks from “a” to “f”, the measured transverse bunch distributions are compared with simulations in Fig. 4.23.

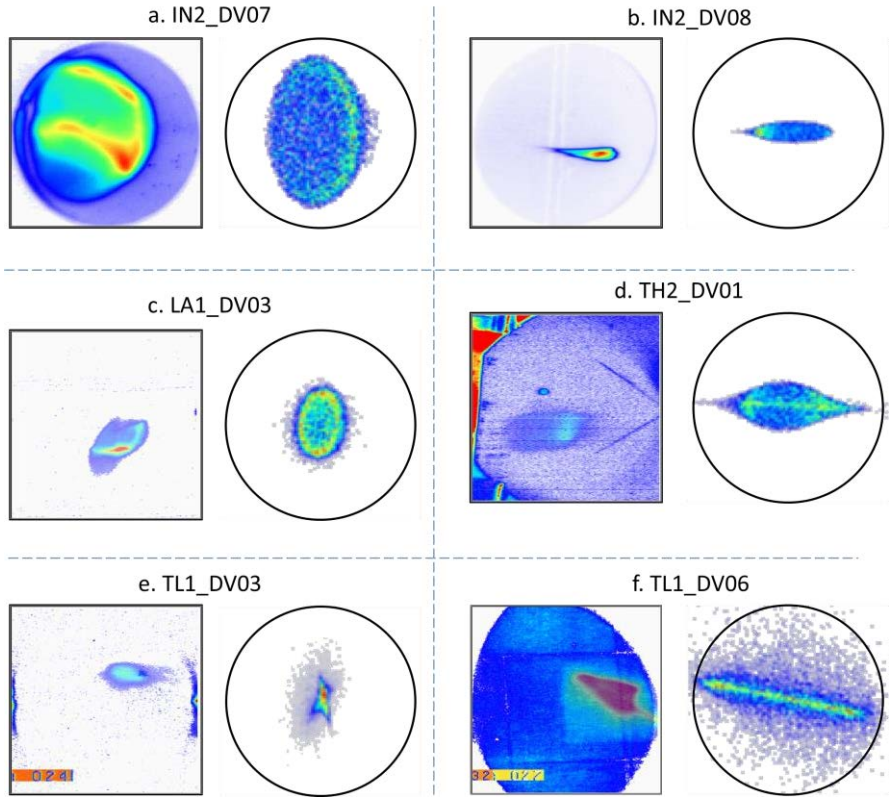

Fig. 4.23 Comparisons of measured (rectangular frame) and simulated (round frame) transverse bunch distributions. Circles surrounding the simulated bunches have the same diameter of screens of 21 mm. The edge

of screens can be seen from the measured bunch distributions. The position of each comparison is marked with the index from a to f, which can be located in Fig. 4.22.

In the beamline section before the quadrupole used for the correction, both the shape and the size of the bunch match well between simulation and experiment, as shown in Fig. 4.23a, b and c. After the corrected quadrupole, the discrepancy becomes larger. However, with the correction of this one quadrupole only, some of the measured features can also be observed in simulation, for instance, the large transverse beam hallow in Fig. 4.23d and the strongly focused beam in Fig. 4.23e. The bunch distribution at the first screen in the straight beamline after the spectrometer (named TL1_DV06) is shown in Fig. 4.23f, with the dipole of the spectrometer turned off.

4.4.4. Emittance measurement

At Screen 2 in the diagnostics beamline, the beam is assumed to be cylindrically symmetric and the transverse emittance was measured vertically with the slit-scan method. The solenoid was set to 3.65 A to focus the beam on Screen 2 and all quadrupoles were turned off. The measured emittance is 7.7±1.1 μm, which is more than twice the simulation result of 3.7 μm. The measured and simulated phase spaces at Screen 2 are shown in Fig. 4.24. It is shown that the measurement and simulation give similar scales of position and angle, but the real beam has a large hallow which influences the rms emittance significantly.

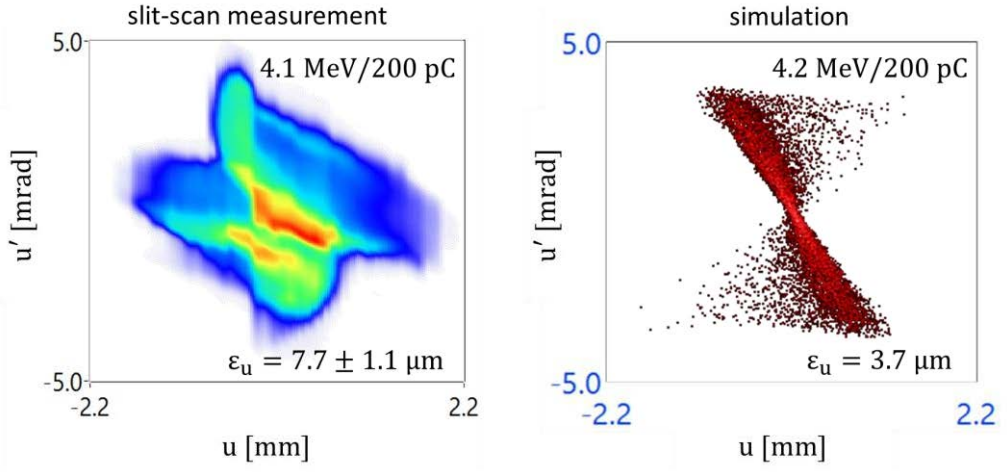

Fig. 4.24 Transverse phase space measured with slit-scan method (left) and simulated (right) for a 200 pC beam in the diagnostics beamline.

As marked in Fig. 4.19, quadrupole-scan emittance measurements were performed at different positions of the beamline. The measurement results are shown in Table 4.1. In the dogleg, the large transverse emittance of 33 μm is the result of dispersion, however, this large

value could not be observed in the simulation at the laser phase minimizing the energy spread. Both transverse and vertical emittance increase from the end of Linac 1 to the end point of the beam transport.

Table 4.1 Results of the emittance measurement with quadrupole-scan. l_d is the distance between the applied quadrupole and screen. The columns of "quadrupole" and "screen" show their internal names at ELBE. For the position of "after linac 2", slice emittance measurement was performed with a dipole between the quadrupole and the screen. The dipole is 0.55 m from the quadrupole and 0.88 m from the screen.

position	quadrupole	screen	$\bar{E}$ [MeV]	l_d [m]	ε_x [μm]	ε_y [μm]
in dogleg	IN2_MQ06	IN2_DV08	4.1	0.22	33	6.7
after Linac 1	LA1_MQ03	LA1_DV03	22	2.12	10.2	5.6
after Linac 2	LA2_MQ01	LA2_DV02	35.2	1.71	14	6.3
after Linac 2	LA2_MQ03	FL1_DV01	29	0.55+ 0.88	-	6.7
before spectrometer	TL1_MQ05	TL1_DV05	35.2	0.46	14	10

Fig. 4.25 presents the measurement results in Table 4.1 compared to the results from simulation. The difference between measured and simulated vertical emittance is smaller than that between measured and simulated transverse emittance. One possible reason is that the real beam was not well aligned in the dogleg and the horizontal kick between slices are larger than that in simulation.

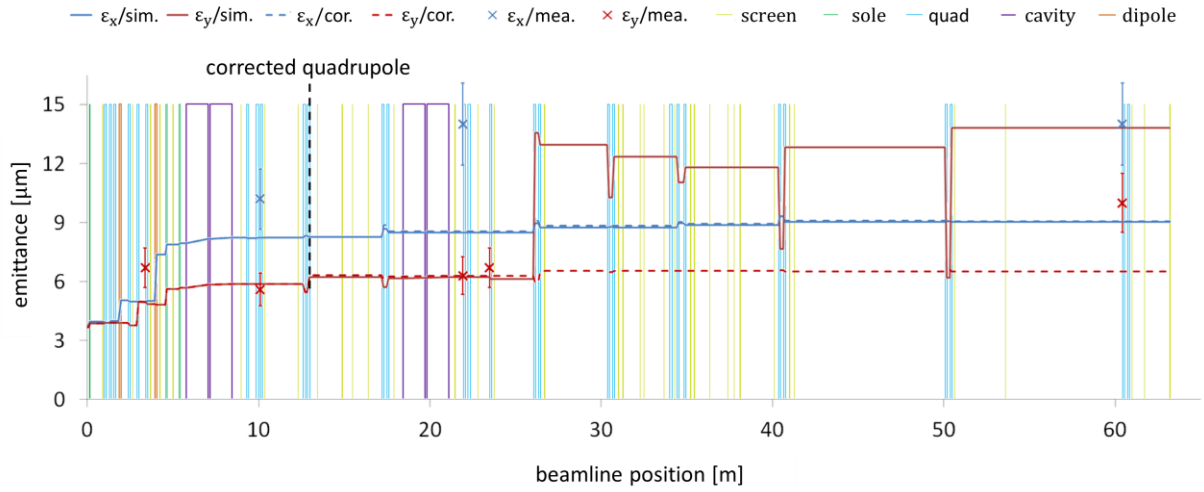

Fig. 4.25 Measured and simulated emittance profiles along the beamline for a 200 pC beam. Dashed lines represent a second simulation with the intensity of only one quadrupole corrected by 8.5%.

4.4.5. Slice emittance and bunch length measurement

In a bending beamline after Linac 2, as shown in Fig. 4.19, vertical slice emittance was measured. The vertical emittance of the entire bunch at this position was measured to be 6.7 μm, as presented in Table 4.1. According to the method introduced in Section 3.4.3, to measure the emittance of temporal slices the beam should be linearly chirped at zero phase. Cavity 4 was used to chirp the bunch. The applied phase of Cavity 4 was 90° from the crest phase and its gradient was set to 1.5 MeV, which provides a positive chirp.

According to analysis in Section 2.5.1, it is the energy slice that causes the slice mismatch problem. The slice emittance for energy slices is shown in Fig. 4.26, where the error of the relative energy of an individual slice with respect to the bunch center was estimated to be about 25 keV. Therefore, the bunch was sliced to pieces with a width of about 50 keV. More slices provide the same energy resolution but lower accuracy of emittance measurement by reducing particle numbers in an individual slice. Slice emittance was measured only for the central part of the bunch. For slices at the head and tail of the bunch, Equation (3-18) provides no solution as the intensity of these slices is too low. In Fig. 4.26, the energy distribution of the bunch is also shown, which is wider than the range of possible slice emittance measurement.

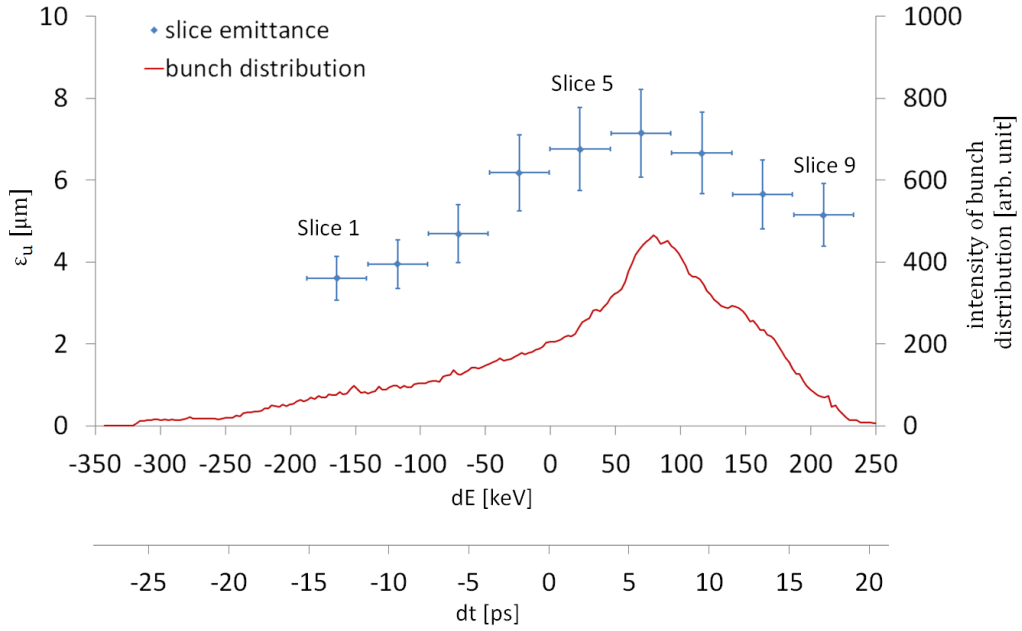

Fig. 4.26 Slice emittance measured after Linac 2. An individual slice has the width of 46 keV. If the chirp is assumed to be linear, the slice emittance of energy slices also represents that of temporal slices and the bunch distribution in energy is also the distribution in time, therefore the bunch length can be calculated.

The left diagram of Fig. 4. 27 shows the phase ellipse of three slices with the same numbering marked in Fig. 4.26. Slices have different orientation angles. The average slice emittance $\varepsilon_{ave.s.u}$ is 6.2 μm.

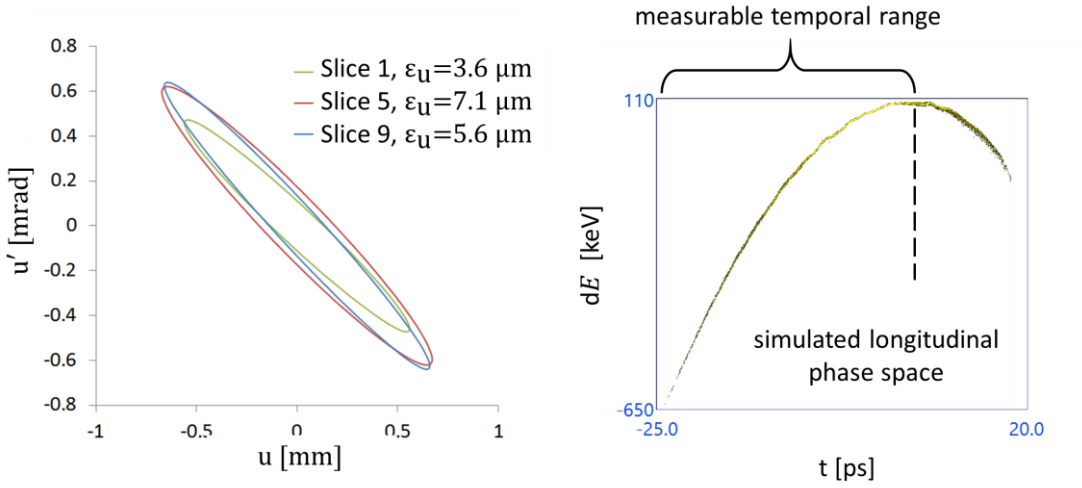

Fig. 4. 27 Measured phase ellipses of three slices. Slices do not have the same orientation (left). Simulated longitudinal phase space at the at the same position as slice emittance measurement (right).

The measured slice emittance of energy slices should also represent that of temporal slices as the beam was assumed to be linearly chirped by Cavity 4. However, in this experiment the electron bunches were very long (about rms 10 ps) which result in severe nonlinearity in longitudinal phase space, and thus the bunch after Cavity 4 cannot be approximated to be linear as shown by the simulated LPS after Cavity 4 in the right diagram of Fig. 4. 27. In this case, the energy slices cannot represent temporal slices. Nevertheless, the temporal scale is given in Fig. 4.26, neglecting the nonlinearity.

Neglecting the nonlinearity of the bunch after Cavity 4, the bunch distribution with respect to time in Fig. 4.26 can be used to calculate the rms bunch length before Cavity 4, which delivers 8.8 ps. In simulation, the bunch length at the same position is 9.0 ps, which only changes by less than 5% in the entire beam transport. Although the measured and simulated bunch lengths are very close, the measurement includes an ineligible systematic error due to the nonlinearity in LPS. The measurable temporal range shown in the right diagram of Fig. 4. 27 is only 70% of the entire bunch. According to the above analysis, the bunch length is about 10 ps as estimated.

5. Conclusion

Parallel to the technological development of the SRF gun at ELBE, this PhD work has been conducted aiming to optimize the gun for high-bunch-charge applications at the ELBE experimental stations: pELBE, nELBE, TELBE and CBS. The SRF gun parameters and the beam transport have to be optimized according to the specific requirements of each experimental station. In this work, rigorous simulations have been conducted for this optimization purpose based on a specially developed simulation tool. In the experimental part, beam diagnostic methods have been developed and applied to verify the beam transport in ELBE and compare it with the predicted simulation results. This close combination of simulation and experimental verification represent the central part of this thesis, which has demonstrated that the SRF gun could be improved to the application level. As the beneficiary, the ELBE center is pushed an important step closer to high-bunch-charge applications.

5.1. Summary of content

Detailed beam parameter requirements for these four experimental stations have been analyzed and proposed. The main challenge for pELBE and nELBE is to match TPS to the calculated acceptance on the beryllium window. A small bunch length is the most significant demand from THz and the transverse beam size is the key parameter for CBS, which should match that of the interaction laser.

In the simulation section, a powerful user-friendly simulation tool based on ASTRA and Elegant has been developed for the specific layout of ELBE, in a highly adaptable way for future modifications of the beamline. This simulation tool extends the understanding of the SRF gun and the beam transport through ELBE accelerator. Important physical effects included in the simulation are studied case-wise, including the electron emission from photocathodes, the slice mismatch problem, the CSR effect, the LSC effect and the Wakefield effect. SRF gun parameters were scanned in simulation and their effects on beam quality were analyzed in detail. Several optimized combinations of parameters were chosen for further beam transport, which was then optimized according to the requirements of high-bunch-charge applications.

Highlighted simulation results demonstrate that a beam with a bunch charge of 200 pC can satisfy all the requirements if transported properly. In the beam transport for pELBE and

nELBE, only the dogleg is a critical beamline section. The bunch compression for TELBE suffers from the nonlinearity in LPS. Methods of alleviating the nonlinearity were proposed and tested numerically, with which the rms bunch length was optimized to 0.12 ps (FWHM 0.24 ps). In the beam transport for CBS experiments, the LSC effect plays an important role in minimizing the energy spread. The minimized rms bunch size is 0.016 mm (FWHM 0.036 mm).

In the experimental sections, beam diagnostic methods are applied, including auto/cross-correlation based pulse length measurement for lasers, dipole-based energy and energy spread measurement, slit-scan emittance measurement, quadrupole-scan emittance measurement and slice emittance measurement. An important part of this PhD work consists of the development of an image processing algorithm, the software for slit-scan emittance measurement and the extra laser beamline for the auto/cross-correlator.

Most important experimental results are summarized as follows: The direct measurement of the temporal distribution of the laser pulse explained the cause of the longitudinal substructure on the electron bunch (in 2015) and motivated the correction of the problem in the UV laser. The SRF Gun was commissioned and the beam quality was improved by applying positive DC voltage and large laser spot size. The LSC effect was verified at PITZ showing that in practice the measured effect is even larger than that from simulations. A beam with a bunch charge of 200 pC was successfully transported up to an energy spectrometer in front of the CBS station. Most of the experimentally measured features can be also computed from simulations. The beamline parameters of the dogleg were optimized by simulation. The emittance of the SRF gun was measured to be 7.7μm at 200 pC.

Compared to the DC gun, the SRF Gun provides more than twice the maximum bunch charge and about half the transverse emittance at present. Besides, the temporal stability of the SRF gun is also better than that of the DC gun [82]. Both simulation and measurement results in this thesis serve as a starting point of utilizing the SRF gun as the injector of ELBE, for higher radiation flux and higher measurement accuracy.

5.2. Outlook

The simulation tool developed in this thesis features an easily adaptable design and convenient data plotting. It is more user-friendly than directly using ASTRA and Elegant. In the future, it can be extended to cover the entire ELBE. Careful measurement and calibrations of magnet fields will be useful to enhance the accuracy of simulation, which provides better guidance for experiments.

All the beam diagnostics presented in this thesis are based on screens and CCDs, which measure multiple bunches in one image and hence suffer from the instability of the beam. The work of locating and reducing vibrations of the beamline is underway and to be continued. The speed of image processing proposed in Section 3.3.3 can be increased by applying the wavelet algorithm properly. An optimization work on the laser transverse distribution has been conducted and will be continued [83].

The SRF gun at ELBE has not achieved its target parameters up to now. Limitations include the gradient of the cavity, the cathode position, the 3D size and distribution of the UV laser pulse and the preparation of Cs_2Te cathode. The gradient was designed to be 18MV/m but in practice the operation value is 8 MV/m, which is due to the accidents that the inner surface of the gun-cavity was scratched during manufacture and contaminated when changing cathodes. The cathode position is currently unchangeable to keep the dark current low. The pulse length of the laser can be optimized experimentally by applying a new crystal, which is not included in the frame of this thesis. The laser spot should match that of the effective area of the cathode, which can be enlarged to an overall diameter of 8 mm. With Cs_2Te cathodes, the maximum bunch charge can reach the nC level.

In the commissioning of ELBE SRF Gun II, two application experiments were conducted as proof of principle. As the first experiment, the beam from ELBE SRF Gun II was transported to nELBE. The neutron ToF measurement was carried out with results shown in Fig.5.1. The background of the measurement caused by the dark current contributed to 17.5% of the total signal. The second experiment was conducted at TELBE. The measured THz spectrum is shown in Fig.5.2. Evaluations of these results are beyond the scope of this thesis. For both applications, the bunch charge was 80 pC and the SRF gun was not optimized.

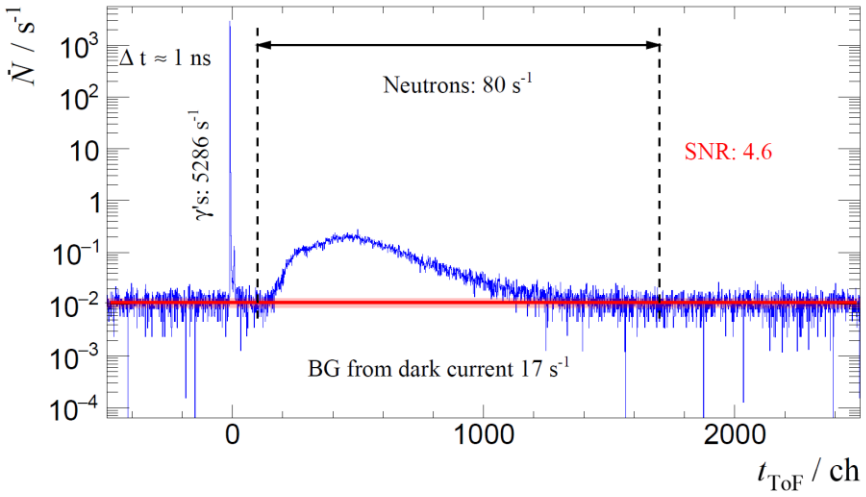

Fig.5.1 Spectrum of the ToF measurement using a beam from ELBE SRF Gun II with a bunch charge of 80 pC. Courtesy Toni Kögler from HZDR.

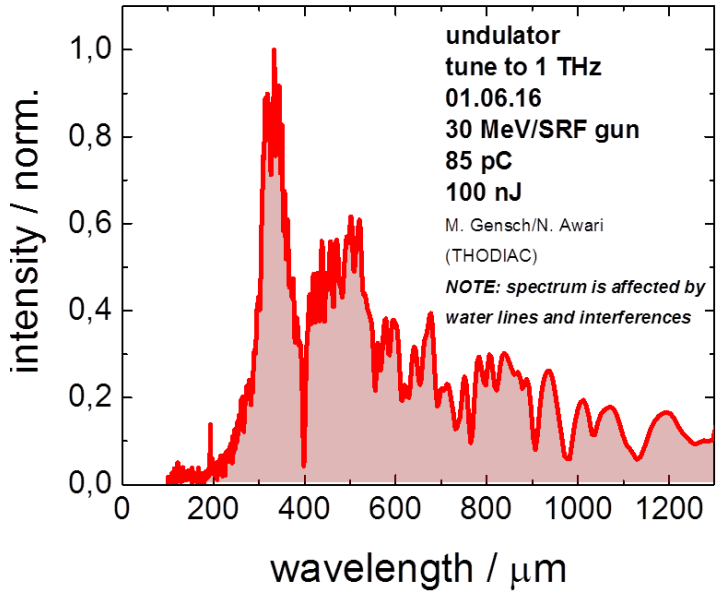

Fig.5.2 Spectrum of the THz radiation using a beam from ELBE SRF Gun II with a bunch charge of 85 pC. Courtesy Michael Gensch from HZDR.

These two applications with the bunch charge of 80 pC and the beam transport experiment with the bunch charge of 200 pC are just the first steps of utilizing ELBE SRF Gun II at the ELBE center. It is expected for nELBE, pELBE, TELBE and CBS experimental stations to benefit from the SRF Gun as a new electron source, providing CW beams with high bunch charge and low emittance.

Acknowledgement

Firstly, I would like to express sincere gratitude to my supervisor Dr. Jochen Teichert for his motivation, patience, immense knowledge and the continuous support of my PhD work. Besides the scientific guidance of this thesis, he also led the SRF gun group to conquer technical difficulties several times to smooth my research.

Besides my supervisor, I would like to thank the rest of my thesis committee: Prof. Dr. Thomas Cowan, Prof. Dr. Ulrich Schramm and Prof. Dr. Carsten Welsch, for their insightful comments and encouragement, as well as for their questions which incented me to widen my research from various perspectives.

My sincere thanks also goes to Dr. Karsten Möller, Dr. Rong Xiang and Dr. John Michael Klopf for their corrections and suggestions on this thesis. A special thanks goes to my officemate Hannes Vennekate for his close cooperation on my work and frequent help with daily language issues. I also appreciate the enlightening scientific help and technical supports from Dr. Peter Michel, Dr. André Arnold, Petr Murcek, Dr. Ulf Lehnert and the rest of the ELBE group,

I thank Prof. Dr. Carsten Welsch, Rob Ashworth, Magdalena Klimontowska for their organization of the LA^{3}NET project which broadly expanded my understanding of European scientific cooperation and provided valuable experience on social affairs. It is a fortune to know the fellows in this project. In particular, I am grateful to Jakob Krämer for useful discussions on the simulation work in this thesis.

Financially, this work is part of the LA3NET and has received funding from the European Union's Seventh Framework Programme for research, technological development and demonstration under grant agreement No. 289191, as well as EuCARD-2, contract number 312453, and by the German Federal Ministry of Education and Research grant 05K12CR1.

Last but not the least, I would like to thank my family and friends, especially my beloved wife Mingming Ma for her close proof reading of this thesis as well as her spiritual support, which is my most important motivation of finishing this PhD work.

Appendix

I. Table of abbreviations

BNL	Brookhaven National Laboratory
CBS	Compton Backscattering
CCD	Charge-Coupled Device
CDR	Coherent Diffraction Radiation
CMOS	Complementary Metal-Oxide-Semiconductor
CP	Cathode Position
CSR	Coherent Synchrotron Radiation
CTR	Coherent Transition Radiation
CW	Continuous-Wave
DC	Direct Current
DESY	Deutsches Elektronen SYnchrotron
DFM	Difference Frequency Mixing
DRACO	DResden lAser aCceleration sOurce
DoN	Degree of Nonlinearity
ELBE	superconducting Electron Linac for beams with high Brilliance and low Emittance
ERL	Energy Recovery Linac
FEL	Free Electron Laser
FFS	Final Focusing System
FFT	Fast Fourier Transform
FLASH	Free electron LASer in Hamburg
FWHM	Full Width Half Maximum
HEE	High-Energy Electrons
HZB	Helmholtz-Zentrum Berlin
HZDR	Helmholtz-Zentrum Dresden-Rossendorf
ICT	Integrating Current Transformer
IR	InfraRed
KEK	The High Energy Accelerator Research Organization of Japan
LCLS	Linac Coherent Light Source

LEEs	Low-Energy Electrons
LP	Laser Phase
LPS	Longitudinal Phase Space
LSC	Longitudinal Space Charge
MBI	Max-Born-Institute
NCRF	Normal Conducting Radio Frequency
nELBE	Neutron experimental station at ELBE
NPS	Naval Postgraduate School
OTR	Optical Transition Radiation
pELBE	Positron experimental station at ELBE
PITZ	Photo Injector Test Facility at DESY, Location Zeuthen
PKU	Peking University
QE	Quantum Efficiency
QWR	Quarter Wave Resonator
RI	Research Instruments
rms	root mean square
rpn	reverse Prolish notation
SACLA	x-ray free electron laser project in Japan
SHG	Second Harmonic Generation
SNR	Signal to Noise Ratio
SRF	Superconducting Radio Frequency
TDS	Transverse Deflecting Structure
TELBE	THz radiation station at ELBE
ToF	Time-of-Flight
TPS	Transverse Phase Space
UV	Ultra Violet
XFEL	X-ray Free Electron Laser
YAG	Yttrium Aluminium Garnet

II. Simulation parameters for Section 2.8

parameter	unit	pELBE	nELBE	THz	CBS
Bunch Charge	[pC]	200	200	200	200
Bunch Length	[ps]	7	7	7	7
Cathode Position	[mm]	2.8	2.8	1.7	1.8
Cavity 1 Gradient	[MV/m]	12	10	12	5.3
Cavity 1 Phase	[deg]	90	90	90	85
Cavity 2 Gradient	[MV/m]	9	7	9	5.3
Cavity 2 Phase	[deg]	80	80	88	85
Cavity 3 Gradient	[MV/m]	7	8	7	5.5
Cavity 3 Phase	[deg]	81	80	51	49
Cavity 4 Gradient	[MV/m]	7	8	7	5.5
Cavity 4 Phase	[deg]	81	80	51	49
Chicane1	[deg]	0	0	0	0
Chicane2	[deg]	11	30	26	19
DC Voltage	[kV]	5	5	5	5
Gun Gradient	[MV/m]	7.5	7.5	7.5	7.5
IN2_ML_01	[T]	0.174	0.174	0.155	0.155
IN2_MQ_01	[$1/m^2$]	-17.13	-17.13	-13.67	-13.67
IN2_MQ_02	[$1/m^2$]	29.493	29.493	28.746	28.746
IN2_MQ_03	[$1/m^2$]	-19.546	-19.546	-13.161	-13.161
IN2_MQ_04	[$1/m^2$]	42.729	42.729	42.722	42.722
IN2_MQ_05	[$1/m^2$]	-30.49	-30.49	-30.763	-30.763
IN2_MQ_06	[$1/m^2$]	42.729	42.729	42.722	42.722
LA1_MQ_01	[$1/m^2$]	3.877	3.877	3.877	6.597
LA1_MQ_02	[$1/m^2$]	-6	-6	-6	-8.662
LA1_MQ_03	[$1/m^2$]	-0.186	-0.186	-0.186	0.192
LA1_MQ_04	[$1/m^2$]	0.621	0.621	0.621	-6.065
LA1_MQ_05	[$1/m^2$]	0.089	0.089	0.089	9.499
LA1_MQ_06	[$1/m^2$]	0	0	0	14.366
LA1_MQ_07	[$1/m^2$]	0	0	0	-11.629
LA2_MQ_01	[$1/m^2$]	5.945	0.257	3.134	3.134

LA2_MQ_02	[1/m^2]	-3.429	0.225	0.298	0.298
LA2_MQ_03	[1/m^2]	-4.291	-3.724	-1.623	-4.623
Laser Phase	[deg]	15	20	20	20
NL1_MQ_01	[1/m^2]	-	-12.854	-	-
NL1_MQ_02	[1/m^2]	-	12.306	-	-
NL1_MQ_03	[1/m^2]	-	12	-	-
NL1_MQ_04	[1/m^2]	-	-7.316	-	-
NL1_MQ_05	[1/m^2]	-	14.902	-	-
NL1_MQ_06	[1/m^2]	-	30.981	-	-
NL1_MQ_07	[1/m^2]	-	-24.024	-	-
PP_MQ_01	[1/m^2]	5.254	-	-	-
PP_MQ_02	[1/m^2]	-0.596	-	-	-
PP_MQ_03	[1/m^2]	-4.562	-	-	-
PP_MQ_04	[1/m^2]	-2.842	-	-	-
PP_MQ_05	[1/m^2]	-0.216	-	-	-
TH1_MQ_01	[1/m^2]	3.112	2.762	-3.899	3.538
TH1_MQ_02	[1/m^2]	-0.103	-0.084	0.4	-0.853
TH1_MQ_03	[1/m^2]	-3.159	-3.159	7.85	2.812
TH1_MQ_04	[1/m^2]	1.405	1.405	-1.863	-5.165
TH2_MQ_01	[1/m^2]	11.828	0	17.787	9.263
TH2_MQ_02	[1/m^2]	-15.074	0	-23.115	-9.623
TH2_MQ_03	[1/m^2]	6.105	0	11.446	2.104
TH2_MQ_4	[1/m^2]	-	-	11.521	-
TL1_MQ_01	[1/m^2]	-	-8.706	-	7.186
TL1_MQ_02	[1/m^2]	-	8	-	-6.594
TL1_MQ_03	[1/m^2]	-	-2.796	-	-8.869
TL1_MQ_04	[1/m^2]	-	1.577	-	9.3
TL1_MQ_05	[1/m^2]	-	-	-	-8.391
TL1_MQ_06	[1/m^2]	-	-	-	8.954
TL1_MQ_07	[1/m^2]	-	-	-	4.139
TL1_MQ_08	[1/m^2]	-	-	-	-4.94

III. Simulation parameters for Section 4.4

parameter	unit	value
Bunch Charge	[pC]	200
Bunch Length	[ps]	7
Cathode Position	[mm]	1.4
Cavity 1 Gradient	[MV/m]	11
Cavity 1 Phase	[deg]	90
Cavity 2 Gradient	[MV/m]	7.5
Cavity 2 Phase	[deg]	83
Cavity 3 Gradient	[MV/m]	6.5
Cavity 3 Phase	[deg]	87
Cavity 4 Gradient	[MV/m]	6.5
Cavity 4 Phase	[deg]	87
DC Voltage	[kV]	5
Gun Gradient	[MV/m]	7.5
IN2_ML_01	[T]	0.176
IN2_MQ_01	[$1/m^2$]	-16.672
IN2_MQ_02	[$1/m^2$]	28.301
IN2_MQ_03	[$1/m^2$]	-5.919
IN2_MQ_04	[$1/m^2$]	40.63
IN2_MQ_05	[$1/m^2$]	-32.866
IN2_MQ_06	[$1/m^2$]	40.644
LA1_MQ_01	[$1/m^2$]	-2.041
LA1_MQ_02	[$1/m^2$]	7.798
LA1_MQ_03	[$1/m^2$]	-3.375
LA1_MQ_04	[$1/m^2$]	14.02
LA1_MQ_05	[$1/m^2$]	-13.96
LA1_MQ_06	[$1/m^2$]	7.418
LA1_MQ_07	[$1/m^2$]	-4.573
LA2_MQ_01	[$1/m^2$]	0
LA2_MQ_02	[$1/m^2$]	0
LA2_MQ_03	[$1/m^2$]	0.345

Laser Phase	[deg]	45
TH1_MQ_01	[1/m^2]	14.274
TH1_MQ_02	[1/m^2]	-12.111
TH1_MQ_03	[1/m^2]	4.325
TH1_MQ_04	[1/m^2]	-3.028
TH2_MQ_01	[1/m^2]	0
TH2_MQ_02	[1/m^2]	3.344
TH2_MQ_03	[1/m^2]	-1.683
TL1_MQ_01	[1/m^2]	6.116
TL1_MQ_02	[1/m^2]	-5.511
TL1_MQ_03	[1/m^2]	-6.687
TL1_MQ_04	[1/m^2]	-5.476
TL1_MQ_05	[1/m^2]	0
TL1_MQ_06	[1/m^2]	0

Bibliography

[1] M. Ferrario, “Overview of FEL injectors”, http://accelconf.web.cern.ch/AccelConf/e06/Pre-Press/THYPA01.pdf.

[2] I. Ben-Zvi, Supercond. Sci. Technol., 29 (2016) 103002.

[3] P. Emma, R. Akre, J. Arthur et al., Nat. Photonics 4, 343 641 (2010).

[4] G. H. Hoffstaetter et al., “The cornell ERL prototype project”, Proceedings of the 2003 Particle Accelerator Conference, pp. 192-194.

[5] A. Bartnik et al., Physical Review Special Topics Accelerators and Beams, 18, 083401 (2015).

[6] C. Gulliford et al., APL 106, 094101 (2015).

[7] B. Dunham et al., APL 102, 034105 (2013).

[8] F. Stephan and M, Krasilnikov, “High brightness photo injectors for brilliant light sources”, Synchrotron Light Sources and Free-Electron Lasers, DOI 10.1007/978-3-319-04507-8_15-1.

[9] F. Sannibale et al., Phys Rev STAB 15 103501 (2012).

[10] J. Sekutowicz et al., "SRF gun development overview", Proceedings of SRF 2015, pp. 994-1000.

[11] H. Chaloupka et al., Nucl. Instrum. Methods Phys. Res., Sect. A 285, 327 (1989).

[12] A. Arnold and J. Teichert, Physical Review Special Topics Accelerators and Beams, 024801 (2011).

[13] J. Hao et al., Nucl. Instrum. Methods Phys. Res., Sect. A 557, 138 (2006).

[14] S. Quan et al., Nucl. Instrum. Methods Phys. Res., Sect. A 798 (2015) 117–120.

[15] A. Burrill, “First horizontal test results of the HZB SRF photoinjector for bERLinPro”, Proceedings of IPAC2015, pp. 2768-2770.

[16] W. Xu et al. “First beam commissioning at BNL ERL SRF gun”, Proceedings of IPAC2015, pp. 1941-1943.

[17] S.P. Niles et al., “NPS prototype superconducting 500 MHz quarter-wave gun update”, Proceedings of FEL2010, pp. 457-460.

[18] S. Belomestnykh et al., “Commissioning of the 112 MHz SRF gun and 500 MHz bunching cavities for the CeC PoP Linac”, Proceedings of IPAC2015, pp. 3597-3599.

[19] R. Legg et al., “Status of the Wisconsin SRF gun”, Proceedings of IPAC2012, pp. 661-663.

[20] D.Kostin et al., “SRF Gun-cavity R&D at DESY”, htTPS://pubdb.xfel.eu/record/288570/files/THPB056.pdf.

[21] T. Konomi et al., “Design, fabrication and performance of SRF-gun-cavity”, Proceedings of SRF2015, pp. 1243-1246.

[22] R. Inagaki et al., “Development of multi-alkali photocathode deposited on LiTi2O4 substrate for SRF-gun”, Proceedings of IPAC2014, pp. 673-675.

[23] C. D. Beard et al., “Conceptual design of a high average current SRF gun”, Proceedings of EPAC08, pp. 220-222.

[24] D. Janssen et al., Nucl. Instrum. Methods Phys. Res., Sect. A 507, 314 (2003).

[25] A. Arnold et al., Nucl. Inst. Meth. A 577(2007) 440.

[26] J. Teichert et al., Nucl. Inst. Meth. A 743(2014)114–120.

[27] R. Xiang et al., “A step closer to the CW high brilliant beam with SRF gun II”, Proceedings of IPAC2015, pp. 1456-1458.

[28] H. Vennekate et al., “Transverse emittance compensation for the rossendorf SRF GUN II”, Proceedings of IPAC2014, pp. 1582-1584.

[29] P. Murcek et al., “The SRF photoinjector at ELBE – design and status 2013”, Proceedings of SRF2013, pp. 148-150.

[30] A. Arnold et al., “Fabrication, tuning, treatment and testing of two 3.5 cell photo-injektor cavities for the ELBE Linac”, Proceedings of SRF2011, pp. 405-407.

[31] I. Will et al., “Photocathode lasers for cesium telluride photocathodes”, 1st LA³NET Topical Workshop, February 20th - 22nd 2013, CERN, Switzerland.

[32] X. J. Wang et al., Nucl. Inst. Meth. A, 1995, 356 (2) 159-166.

[33] T. Srinivasan-Rao et al., Review of scientific instruments 1998; 69 (6): 2292-2296.

[34] H. B. Michaelson, Journal of Applied Physics 1950; 21(6): 536-540.

[35] P. Michel et al., “Status of the radiation source ELBE upgrade”, Proceedings of IPAC2014, pp. 2233-2234.

[36] A. Büchner et al., “First operation of the ELBE superconducting electron linear accelerator”, Proceedings of FEL2001, pp. 19-20.

[37] A. Wagner et al., Journal of Physics: Conference Series 618 (2015) 012042.

[38] K. A. Olive et al. (Particle Data Group), Chin. Phys. C, 38, 090001 (2014).

[39] J. Klug, E. Altstadt et al., Nucl. Inst. Meth. A 577 (2007) 641.

[40] D.W. Muir and M. Herman, “Long term needs for nuclear data development”, INDC(NDS)-428, IAEA Nuclear Data Section Vienna, Austria, 2000.

[41] R. Beyer E et al., Nucl. Inst. Meth. A 575 (2007) 449.

[42] M. Sands, “A beta mismatch parameter”, SLAC internal report SLAC-AP-85 (1991).

[43] M. Gensch et al., “Thz facility at ELBE: a versatile test facility for electron bunch diagnostics on quasi-CW electron beams”, Proceedings of IPAC2014, pp. 933-934.

[44] M. Gensch,“Brilliant infrared lightsources for micro-ellipsometric studies of organic thin films”, in Ellipsometry of Functional Organic Surfaces and Films, Springer Series in Optical Sciences 52, DOI 10.1007/978-3-642-40128-2.

[45] F. Kuschewski et al., "Optical nanoscopy of transient states of Matter", Scientific Reports (2015), 12582.

[46] P. Levi Sandri, Dario Moricciani, Nucl. Inst. Meth. A 455 (2000) 1-6.

[47] K. Chouffani et al., Phys. Rev. ST Accel. Beams 9, 050701 (2006).

[48] S. Chen et al., Phys. Rev. Lett. 110, 155003 (2013).

[49] A. Jochmann, “Development and characterization of a tunable ultrafast x-ray source via inverse-compton-scattering”, PhD thesis. TU Dresden, HZDR, 2014.

[50] K. Zeil et al., New J. Phys. 12, 045015 (2010).

[51] A. Jochmann et al., Phys. Rev. Lett. 111, 114803 (2013).

[52] S. M. Vinko et al., Nature 482.7383 (Feb. 2012), pp. 59–62.

[53] C. Rischel et al., Nature 390.6659 (Dec. 1997), pp. 490–492.

[54] H. N. Chapman et al., Nature 470.7332 (Feb. 2011), pp. 73–7.

[55] K. Flöttmann, ASTRA: A space charge tracking algorithm, Manual, Version 3 (2011), update April 2014.

[56] H, J. Billen, Poisson Superfish, version 7.17, LA-UR-96-1834 (2006).

[57] M. Borland, Advanced Photon Source LS-287, September 2000.

[58] CST STUDIO SUITE™, CST AG, Germany, www.cst.com.

[59] K. Flöttmann, “Note on the thermal emittance of electrons emitted by cesium telluride photocathodes”, TESLA FEL-Report 1997-01, http://flash.desy.de/sites2009/site_vuvfel/content/e403/e1642/e839/e829/infoboxContent830/tesla-fel1997-01.pdf.

[60] D. Dowell and J. Schmerge, PRST-AB 12,074201, 2009.

[61] V. Volkov and D. Jansen, “RF focusing – an instrument for beam quality improvement in superconducting RF guns”, Proceedings of EPAC2000, pp. 2055–2057.

[62] H. Vennekate, “Emittance compensation for SRF photo injectors”, Ph.D. thesis of Dresden University of Technology, 2016 – to be published.

[63] André Arnold, Simulation und Messung der Hochfrequenzeigenschaften einer supraleitenden Photo-Elektronenquelle, Dissertation, Fakultät für Informatik und Elektrotechnik der Universität Rostock, 2012.

[64] A. Mostacci et al., PRST-AB, 15, 082802 (2012).

[65] C. Limborg-Deprey et al., Nuclear Instruments and Methods in Physics Research Section A: Accelerators, Spectrometers, Detectors and Associated Equipment, 557 (2006) 106–116.

[66] M. Borland, Physical Review Special Topics - Accelerators and Beams, Volume 4, 070701 (2001).

[67] S. Di Mitri and M. Cornacchia, Nucl. Instrum. Methods Phys. Res., Sect. A 735, 60 (2014).

[68] S. Di Mitri, “CSR-induced emittance growth and related design strategies”, USPAS, 2015.

[69] Z. Huang et al., Physical Review Special Topics - Accelerators and Beams, Volume 7, 074401 (2004) 074401-1.

[70] R. M. Jones, “Hom Mitigation”, CAS RF Lecture Series 15-6-2010, http://cas.web.cern.ch/cas/Denmark-2010/Lectures/Jones-1.pdf.

[71] G. V. Stupakov, “Wake and Impedance”, SLAC-PUB-8683, October 2000.

[72] K.Miyata and M.Nishi, Particle Accelerators, 1990, Vol. 34, pp. 131-154.

[73] M. Borland, User’s manual for Elegant, http://www.aps.anl.gov/Accelerator_Systems_Division/Accelerator_Operations_Physics/manuals/elegant_latest/elegant.html.

[74] Eden T. Tulu et al., “3D multipacting study for the rossendorf SRF gun”, Proceedings of SRF2013, pp. 991-994.

[75] H. Edwards et al., "3.9 GHz cavity module for linear bunch compression at FLASH", Proceedings of LINAC2010, pp. 42-45.

[76] A.P.E company, online manual, http://www.ape-berlin.de/sites/default/files/pulseCheck_SM.pdf.

[77] C. Browne and W. Buechner, The Review of Scientific Instruments, 27 (1956).

[78] J. Rudolph, “Instruments and techniques for analysing the time-resolved transverse phase space distribution of high-brightness electron beams”, Ph. D. thesis, der Universität Rostock, 2012.

[79] L. Staykov, “Characterization of the transverse phase space at the photo-injector test facility in DESY, Zeuthen site”, Ph.D. thesis, University of Hamburg, 2008.

[80] G. Vashchenko et al., “Emittance measurements of the electron beam at PITZ for the commissioning phase of the European XFEL”, Proceedings of FEL2015, pp. 285-288.

[81] H. Huck et al., “First results of commissioning of the PITZ transverse deflecting structure”, Proceedings of FEL2015, pp. 110-114.

[82] M. Kuntzsch et al., “Bunch Compression Dependent Jitter Analysis with Large Spectral Range”, Proceedings of IBIC2015, pp. 43-45.

[83] F. Roscher, "Erprobung und Evaluierung eines räumlichen Lichtmodulators (SLM) zur Verbesserung der Strahlqualität eines Photokathodenlasers", Diplomarbeit, Hochschule für Wirtschaft und Technik Dresden.

Erklärung

Hiermit versichere ich, dass ich die vorliegende Arbeit ohne unzulässige Hilfe Dritter und ohne Benutzung anderer als der angegebenen Hilfsmittel angefertigt habe; die aus fremden Quellen direkt oder indirekt übernommenen Gedanken sind als solche kenntlich gemacht. Die Arbeit wurde bisher weder im Inland noch im Ausland in gleicher oder ähnlicher Form einer anderen Prüfungsbehörde vorgelegt.

Diese Arbeit wurde am Institute für Kern und Teilchenphysik der Technischen Universität Dresden unter wissenschaftlicher Betreuung von Prof. Dr. Ulrich Schramm angefertigt.

Es haben keine früheren erfolglosen Promotionsverfahren stattgefunden.

Ich erkenne die Promotionsordnung der Fakultät Mathematik und Naturwissenschaften an der Technischen Universität Dresden vom 23.02.2011 in der Fassung vom 18.06.2014 an.

Dresden, den 07.11.2016